Sterol-phospholipid interactions in model lipid membranes

Jonathan Paul Litz

A dissertation
submitted in partial fulfillment of the
requirements for the degree of

Doctor of Philosophy

University of Washington

2015

Reading Committee:

Sarah L. Keller, Chair

Lutz G. Maibaum

Joshua C. Vaughan

Program Authorized to Offer Degree:
Chemistry

University of Washington

Abstract

Sterol-phospholipid interactions in model lipid membranes

Jonathan Paul Litz

Chair of the Supervisory Committee:
Professor Sarah L. Keller
Departments of Chemistry and Physics

Cell membranes feature complex intermolecular interactions between phospholipids and sterols. In this dissertation, I discuss how the accessibility (a measure of chemical activity) of cholesterol in a lipid bilayer varies as a function of bilayer composition. By using the two complementary cyclodextrins (methyl-beta and hydroxypropyl-alpha), I assay the accessibility of both cholesterol and phospholipids for removal from lipid bilayers. Next, I present ternary phase diagrams of mixtures of an unsaturated lipid, a saturated lipid, and one of three different sterols (β-sitosterol, stigmasterol, and ergosterol). Finally, I present research to which I contributed on the thickness mismatch of coexisting liquid phases in model lipid membranes.

TABLE OF CONTENTS

ACKNOWLEDGMENTS

Over the last five years, I have had the great fortune to work with and be surrounded by an absolutely incredible group of mentors, colleagues, and friends. First and foremost, I would like to thank Sarah Keller, whose guidance and support in graduate school have been unmatched. Sarah is a brilliant scientist, fun to work with, and an excellent mentor. I am also indebted to Thomas Portet, who took me under his wing and brought me up to speed in biophysics research when I first transferred into the Keller group. Likewise, it was a blast to discuss my research with Matt Blosser. Matt was always there to help me fill in my physics-based knowledge gaps, as well as to discuss academia, politics, sports, or whatever else he or I had been pondering. My thanks also go to my wonderful labmates Ranee James, Joan Bleecker, Scott Rayermann, Caitlin Cornell, Christina Faller, Glennis Rayermann, Moshe Gordon, Roy Black, Ryan Brewster, and Bo Lee, as well as to the amphiphiliphiles and the UW Chemistry staff.

There is no way for me to express in words my gratitude for the love and support afforded to me by my friends and family throughout graduate school (and life). Mom and Dad, you are incredible; you instilled in me a desire to question and to learn, and you have been endlessly supportive and loving since day one. Friends, I am blessed to have you; when times were tough you were there to help, and when times were good you were there to celebrate. Helen, you deserve thanks as a colleague, a friend, and a family member; I look forward to continuing to grow, love, and learn with you.

Chapter 1
INTRODUCTION

1.1 Overview

This dissertation is divided into two parts: Chapters 1-6 describe my current research on the physical chemistry and biophysics of lipid bilayers; Chapters 7-9 describe my first two-and-a-half years of graduate research in which I developed computational models to describe the interactions between localized surface plasmon resonance supporting nanoparticle aggregates and molecular probes. Four chapters in this dissertation (Chapters 2 and 7-9) are reproductions of papers I authored or co-authored that have been published in peer-reviewed journals.[1–4] One chapter (Chapter 6) contains work that is currently under review for publication.[5] Not included in this dissertation are publications resulting from my undergraduate research.[6–9]

1.2 Selecting a model system

Cellular membranes are chemical zoos comprised of thousands of different types of lipids and proteins. These species interact in complex and unpredictable ways. A recent study found over 500 different lipid species in human blood plasma.[10] Given that this study was performed on 100 similarly aged Americans and that diet and genetics play a significant role in an individual's lipid profile, it is likely that the full human lipidome is far more diverse.[10,11] How then, does one go about systematically studying the physical properties of cell membranes? One approach is to reduce the system down to its minimal functional components. At its simplest, the cell membrane can be thought of as a lipid bilayer, devoid of proteins. In aqueous solution, lipids self-assemble into an array of supramolecular structures designed to minimize contact between water and their hydrophobic tails. The two most common classes of lipid in animal and yeast cells are sterols and phosphatidylcholine (PC)-lipids.[12–14]

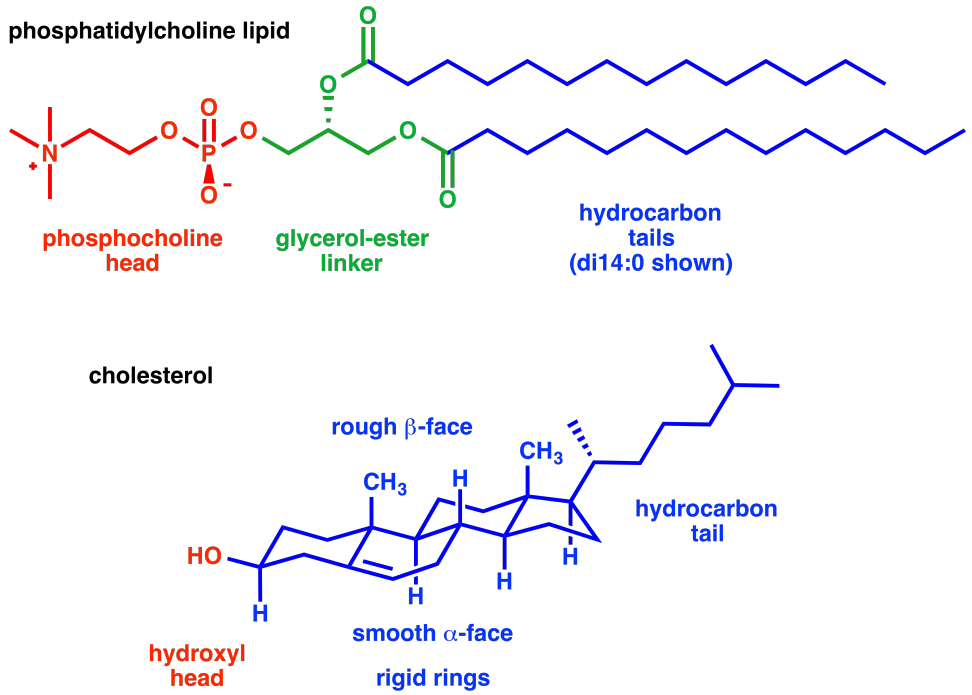

Figure 1.1: The chemical structures of phosphatidylcholine lipids (top) and cholesterol (bottom). PC-lipids have a large, zwitterionic headgroup, a glycerol-ester linker group, and two fatty-acid-derived hydrocarbon tails. Cholesterol has a small, hydroxyl headgroup, a rigid-ring body, and a short hydrocarbon tail. Hydrophilic regions are depicted in red and hydrophobic regions are depicted in blue. The glycerol-ester linker is of intermediate polarity and is depicted in green.

1.2.1 Phosphatidylcholine lipids

PC-lipids are a class of phospholipids defined by three structural features: a hydrophilic phosphocholine headgroup, a chiral glycerol-ester or glycerol-ether linker group, and two hydrophobic, fatty-acid-derived hydrocarbon tails (Fig. 1.1). The most common PC-lipids in animal and yeast cells have asymmetric tails of 16 or 18 carbons, at least one of which contains a *cis* double bond.[12–15] PC-lipids are commonly referred to by the number of carbons and degree of unsaturation of their tails. For example, di-18:1-PC denotes a PC-lipid with two identical tails, each 18 carbons long with a single double bond. All lipids discussed in this work possess right-handed glycerol-ester linker groups and contain only *cis* double bonds; 18:1 refers to an 18 carbon acyl chain with a *cis* double bond located between the ninth and tenth carbons.

1.2.2 Cholesterol

Cholesterol is a predominantly hydrophobic lipid with a small hydroxyl headgroup, a rigid 4-member-ring body, and a short hydrocarbon tail (Fig. 1.1, bottom). The ring structure has a "smooth" α-face comprised only of C-H bonds and a "rough," sterically crowded β-face containing two methyl groups. Due to its rigid structure and small headgroup, cholesterol does not form single-component bilayers. It does incorporate into PC-lipid bilayers, where its rigid structure increases bilayer order but depresses T_{melt}. Cholesterol is soluble up to 65-70 mol% in saturated and monounsaturated PC-lipid bilayers.[16,17]

1.2.3 Giant unilamellar vesicles

The assembly of mixtures of PC-lipids and cholesterol into giant unilamellar vesicles (GUVs) has been discussed in depth previously.[18] These spherical supramolecular structures (vesicles) consist of a single lipid bilayer (unilamellar) that is 10-100 μm in diameter (giant). GUVs make for excellent model systems because they are large enough to be observed by fluorescence microscopy, and their composition can be finely tuned.[17,19]

Lipid bilayers are referred to as being more ordered or less ordered based on measurements of the average linearity of the lipid tails as measured by ^{2}H NMR[20] or wide angle x-ray scattering.[21] In general, order correlates directly with increased lipid tail saturation: order increases from bilayers comprised of di-18:1-PC to 18:1-18:0-PC to di-18:0-PC. Bilayer order is also positively correlated with bilayer main phase transition (melting) temperature, T_{melt}, and the affinity of the bilayer's component lipids for cholesterol.

1.2.4 Cyclodextrins

Randomly methylated β-cyclodextrin (mβCD) is a cyclic oligosaccharide composed of seven glucose subunits that have an average of 1.6-2.0 methyls per glucose (see Fig. 1.2). mβCD has a hydrophilic exterior and a hydrophobic core. The exterior makes mβCD water soluble, while the interior enables it to encapsulate small hydrophobic molecules like cholesterol. At low concentrations (less than 5-20 mM), mβCD selectively removes cholesterol from lipid bilayers, leaving PC-lipids behind.[22,23]

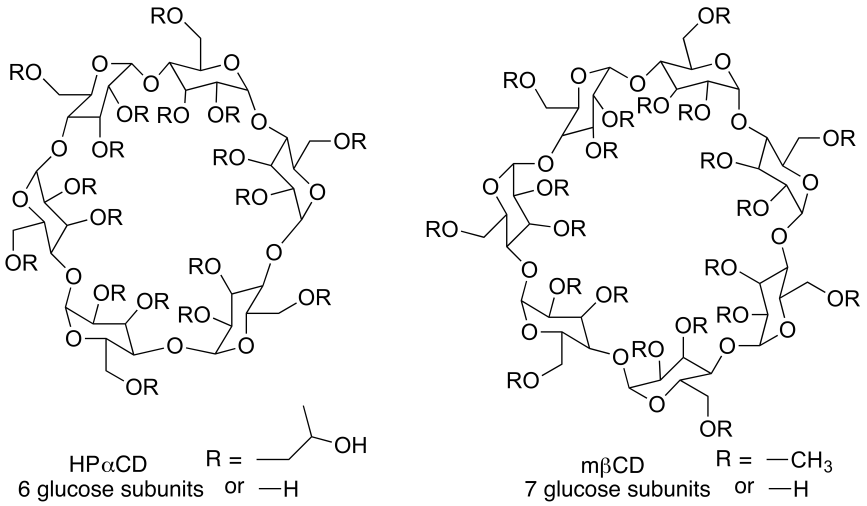

Figure 1.2: The chemical structures of HPαCD and mβCD. HPαCD selectively removes PC-lipids from membranes, leaving cholesterol behind. mβCD selectively removes cholesterol from membranes, leaving PC-lipids behind.[23]

Randomly 2-hydroxypropylated α-cyclodextrin (HPαCD) is a cyclic oligosaccharide composed of six glucose subunits that have an average of 1.6-2.0 2-hydroxyproplys per glucose (see Fig. 1.2). Like mβCD, HPαCD has a hydrophilic exterior and a hydrophobic core. However, the smaller hydrophillic core of HPαCD is not large enough to incorporate cholesterol. Instead it accommodates individual acyl chains of PC-lipids.[23] At concentrations of 25-75 mM, HPαCD selectively removes PC-lipids from lipid bilayers, leaving cholesterol behind.[23]

1.3 Membrane physical parameters

It is often useful to have rough estimations of lipid bilayer physical properties. A few particularly useful numbers follow.

The half-time of cholesterol flip-flop (movement from leaflet-to-leaflet) in liquid-phase bilayers is on the order of milliseconds (all measurements thus far have been limited by experimental time-resolution).[24–27] The half-time for desorption of cholesterol from a fluid bilayer into the aqueous phase is on the order of hours.[25]

The diffusion rate of lipids in a fluid bilayer is on the order of 1 $\mu m^2/s$.[28]

The average area per molecule in a PC-lipid bilayer is typically between 40 and 90 $Å^2$.[29,30] The thickness of a PC-lipid bilayer is typically between 20 and 50 Å.[29,30] The hydrocarbon

portion of the lipid bilayer is well-approximated as incompressible.[31]

1.4 Descriptions of cholesterol activity

There have been descriptions of the activity,[32] accessibility,[33] fugacity,[34] escape tendency,[35] depletion rate,[4] and efflux rate[36] of membrane cholesterol in the literature. Many of these terms have been used interchangeably in the literature. Here I provide some clarity on the common usage of each term.

1.4.1 Terms from thermodynamics

Two of the terms from the above list that have thermodynamic definitions are *activity* and *fugacity*.

Activity

To define chemical activity, we begin by defining chemical potential of species in a mixture. The chemical potential of a species i in an ideal mixture, μ_i^{I}, is

$$\mu_i^{\mathrm{I}} = \mu_i^* + RT \ln \chi_i, \tag{1.1}$$

where μ_i^* is the chemical potential of pure liquid i, χ_i is the mole fraction of i, and I denotes ideal. Deviation from ideal mixing can be expressed in terms of the activity (or effective mole fraction) of a chemical species, a_i, as

$$\mu_i = \mu_i^{\mathrm{ref}} + RT \ln a_i, \tag{1.2}$$

where μ_i is the chemical potential of i in the real mixture, and μ_i^{ref} is the chemical potential of i in a reference state (often chosen as the chemical potential of i as χ_i goes to 1 under the experimental conditions of interest).

Because pure cholesterol does not form stable bilayers, this choice of reference state is not applicable for defining the activity of cholesterol in a bilayer, a_C. Instead, I choose to define a_C against the chemical potential of cholesterol at its solubility limit in the bilayer, μ_C^{sol},

$$\mu_C = \mu_C^{\mathrm{sol}} + RT \ln a_C. \tag{1.3}$$

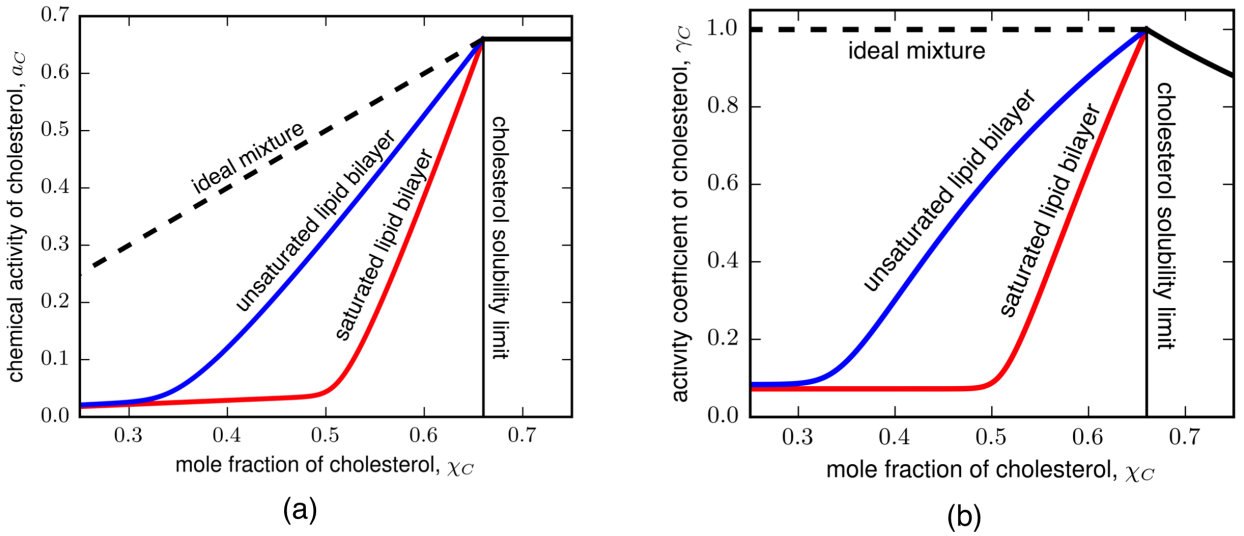

Figure 1.3: Schematics of possible relationships between the chemical activity (a) and activity coefficient (b) of cholesterol in a phospholipid bilayer comprised of an unsaturated lipid bilayer (blue) or saturated lipid bilayer (red). For comparison, the chemical activity and activity coefficient for cholesterol if the bilayer were to behave as an ideal mixture is shown (dotted black line). The values plotted here are in qualitative agreement with results from Ref. 4.

Often, it is useful to consider the composition-dependent relationship between a_C and χ_C. To do so, it is natural to use the activity coefficient, γ_C, defined as,

$$\gamma_C(\chi_C) = \frac{a_C(\chi_C)}{\chi_C}. \tag{1.4}$$

Because we chose μ_C^{sol} as the chemical potential against which a_C is defined, at the solubility limit of cholesterol in the bilayer, χ_{sol},

$$\gamma_C(\chi_{\text{sol}}) = 1, \text{ and} \tag{1.5}$$

$$a_C(\chi_{\text{sol}}) = \chi_{\text{sol}}. \tag{1.6}$$

Here, a_C can be conceptualized as the effective mole fraction of cholesterol in the bilayer and γ_C can be thought of as the proportionality constant that reports the fraction of active cholesterol in the bilayer. In Fig. 1.3, I plot examples of a_C and γ_C that are in qualitative agreement with results from Ref. 4.

It is important to remember that the activity of cholesterol in a 2D-bilayer is not entirely analogous to the activity of a species in a 3D-liquid. The apparent activity of cholesterol

associated with movement normal to the plane of the bilayer does not have to be equal to the activity of cholesterol associated with movement in the plane of the bilayer. For example, imagine a bilayer comprised of lipids with large, water-shielding headgroups. The activity of cholesterol would be high in the plane of the membrane, but the apparent activity of cholesterol associated with removal of cholesterol from the bilayer into the surrounding aqueous solution would be low.

Fugacity

The definitions of *fugacity* and chemical *activity* have a long history of conflation.[37] Typically, *fugacity* is used to describe gases and is most simply described as the effective pressure of a real gas. However, in one of the first papers to report on the accessibility of membrane cholesterol, McConnell stated, "Chemical activity is the same quantity as the classical term *fugacity*, meaning tendency to flee."[38] This term has been adopted in reference to some experiments measuring cholesterol accessibility.[34,35,39–45] Although it is not particularly misleading to use the terms *fugacity* and *accessibility* interchangeably, readers who encounter "the fugacity of cholesterol" are likely to form a mental image of measuring the ease with which cholesterol tends to escape from the membrane only in the direction normal to the plane of the membrane. However, as stated above, the activity of cholesterol in the direction normal to the plane of the membrane is not necessarily equivalent to the activity of cholesterol in the plane of the membrane.

1.4.2 Terms from experiments

Accessibility

The accessibility (or surface accessibility) of cholesterol is a loosely defined term used to describe the apparent chemical activity of cholesterol in the direction normal to the plane of the bilayer. Cholesterol accessibility has been quantified in terms of the degree of binding of cytolysins to membranes,[33,46] the rate of cholesterol oxidation by cholesterol oxidase,[47] and the rate of cholesterol depletion by cyclodextrins.[4] Absolute measurements of cholesterol accessibility determined by different techniques can be compared only qualitatively. Also,

care must be taken to make sure that accessibility measurements are not sensitive to changes in the probe used. For example, it has been shown that slight modification of the active site of the cytolysin perfringolysin O significantly changes measured values of cholesterol accessibility.[48]

Depletion rate / Efflux rate / Escape rate

The terms *depletion rate*, *efflux rate*, or *escape rate* of cholesterol are all used interchangeably to describe the rate at which a cholesterol-accepting molecule like cyclodextrin or high-density lipoprotein pulls cholesterol from a membrane. Typically *efflux* is used in reference to cells (as opposed to model membranes). These rates are all measures of the accessibility of cholesterol. Their absolute values depend both on the interaction between cholesterol and the acceptor and the concentration of the acceptor. An example of the results gained from this type of measurement is shown in Fig. 1.4.

Escape tendency

Escape tendency is often used as a synonym for chemical activity. However, this usage leads to the same problems as using the term *fugacity* because the activity of cholesterol within the membrane does not have to equal its tendency to escape from the membrane.

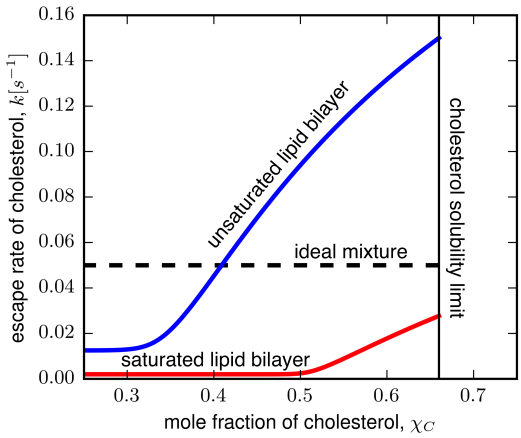

Figure 1.4: Qualitative escape rate 'constant' of cholesterol from a phospholipid bilayer comprised of an unsaturated lipid (blue) or saturated lipid (red) plotted against the mole fraction of cholesterol, χ_C. For comparison, the escape rate constant of cholesterol if the bilayer were to behave as an ideal mixture is shown (dotted black line). The values plotted here are in qualitative agreement with results from Ref. 4.

Chapter 2

DEPLETION WITH CYCLODEXTRIN REVEALS TWO POPULATIONS OF CHOLESTEROL IN MODEL LIPID MEMBRANES

My contribution to this work: I was intimately involved in all aspects of this project.

2.1 Abstract

Recent results provide evidence that cholesterol is highly accessible for removal from both cell and model membranes above a threshold concentration that varies with membrane composition. Here we measured the rate at which methyl-β-cyclodextrin depletes cholesterol from a supported lipid bilayer as a function of cholesterol mole fraction. We formed supported bilayers from two-component mixtures of cholesterol and a phosphatidylcholine (PC)-lipid, and we directly visualized the rate of decrease in area of the bilayers with fluorescence microscopy. Our technique yields the accessibility of cholesterol over a wide range of concentrations (30-66 mol%) for many individual bilayers, enabling fast acquisition of replicate data. We found that the bilayers contain two populations of cholesterol, one with low surface accessibility and one with high accessibility. A larger fraction of the total membrane cholesterol appears in the more accessible population when the acyl chains of the PC-lipid tails are more unsaturated. Our findings are most consistent with the predictions of the condensed-complex and cholesterol bilayer domain models of cholesterol-phospholipid interactions in lipid membranes.

2.2 Introduction

Mammalian cells regulate the concentration of cholesterol in their plasma membrane (∼40 mol%) and endoplasmic reticulum (∼5 mol%). When the concentration of cholesterol in the cell plasma membrane falls below a physiological set point, activation of a signaling pathway results in proteins in the endoplasmic reticulum upregulating cellular cholesterol production.[44,45,49] The cell may maintain this set point by monitoring the chemical activity (effective concentration) of cholesterol in the plasma membrane, which can be significantly different than the total plasma membrane cholesterol concentration.[40,44,50,51] In humans, diets high in saturated fats correlate with hypercholesterolemia, whereas diets high in monounsaturated fats are comparatively hypocholesterolemic.[52] The link between saturated fats and hypercholesterolemia may lie in the disparity between the activity and total concentration of cholesterol in the plasma membrane. Cholesterol interacts more favorably with saturated phospholipids than unsaturated phospholipids in membranes.[53] These favorable interactions

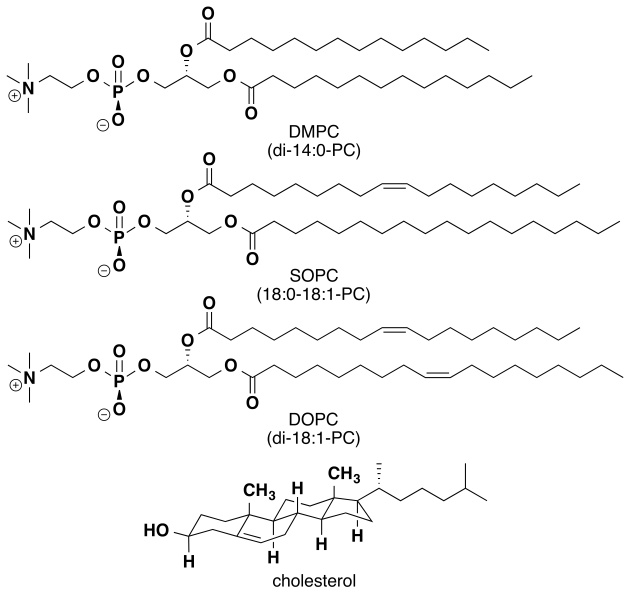

Figure 2.1: The molecular structures of DMPC (di-14:0-PC), SOPC (18:0-18:1-PC), DOPC (di-18:0-PC), and cholesterol. DMPC has two saturated tails. SOPC has one saturated and one monounsaturated tail. DOPC has two monounsaturated tails.

may reduce the activity of cholesterol with respect to total concentration, such that cells with higher concentrations of saturated lipids trigger cholesterol production even when the plasma membrane contains elevated levels of cholesterol.

Direct measurement of the activity of cholesterol in a membrane is difficult. Determining the surface accessibility of cholesterol is more experimentally tractable, and this quantity is hypothesized to be proportional to the activity of cholesterol within the membrane.[32] Here, we investigated whether all cholesterol molecules in a two-component phosphatidylcholine (PC)-lipid bilayer at high concentrations of cholesterol (30-66 mol%) are equally accessible for removal by methyl-β-cyclodextrin (mβCD). Specifically, we used fluorescence microscopy to image the decrease in area of PC-lipid membranes as mβCD selectively pulled cholesterol from them. We used the rate of decrease in membrane area to determine the rate of cholesterol depletion as a function of both the mole fraction of cholesterol (χ_C) and the degree of unsaturation of the PC-lipid tails. Molecular structures of the three phospholipids studied (DMPC, SOPC, and DOPC in order of increasing acyl chain unsaturation) and cholesterol are shown in Fig. 2.1.

Previously, cholesterol-dependent cytolysins and cholesterol oxidase have been used to assay the accessibility of cholesterol in two-component PC-lipid membranes.[33,46–48,54–58] The binding of two cytolysins, perfringolysin O and anthrolysin O, to cholesterol in the membrane increases sharply above a single χ_C characteristic to the PC-lipid in the bilayer.[33,46,48,54–56] Generally, this χ_C decreases with increasing lipid tail unsaturation. However, slight structural modification of the protein[59] or changes in pH[54] can cause this characteristic χ_C to shift independently of membrane lipid composition. These sensitivities make it difficult to isolate changes in the accessibility of cholesterol from changes in the binding behavior of the cytolysin. The use of monomeric cytolysin subunits may alleviate this problem.[48] Cholesterol oxidase converts cholesterol into cholest-4-en-3-one, altering the composition of the bilayer. This structural change should have minimal impact on the initial rate of oxidation measured, but the eventual widespread replacement of cholesterol, even by structurally-similar sterols, can drastically change membrane properties.[17,60] There have been disagreements in the literature stemming from the interpretation of results from cholesterol oxidase assays. In particular, some studies claim there is only one χ_C above which cholesterol accessibility increases sharply,[47] whereas others claim to observe several spikes in cholesterol oxidase activity at specific values of χ_C.[57,58] Results from previous cytolysin and cholesterol oxidase studies on two-component lipid bilayers are summarized in Table 2.1. Our mβCD area depletion assay avoids significant chemical modification of membrane components while giving an unambiguous readout of the accessibility of cholesterol as a function of χ_C.

There are three significant experimental challenges to overcome in measuring mβCD-induced area depletion of bilayers to determine the accessibility of membrane cholesterol over a wide range of χ_C. First, membrane fluctuations must be suppressed so the decrease in area can be measured accurately. Second, membrane tension must be approximately constant throughout the depletion process so that changes in tension do not influence the measured accessibility; changes in membrane tension makes measurements involving vesicles problematic.[61,62] Third, knowledge of the area per molecule of the membrane as a function of cholesterol concentration is needed. This quantity is straightforward to measure for monolayers[63] but much more challenging to determine for bilayers.[64] We addressed the first two challenges by developing a method of rupturing biotinylated giant unilamellar vesicles

Table 2.1: Previously published measurements of cholesterol accessibility for two-component PC-lipid bilayers.

PC-lipid[a]	Characteristic χ_C[b]	Assay	Ref.
di-16:0	0.63, 0.58	cholesterol oxidase (COD)	58
	0.50	COD	47
di-14:0	0.50	COD	47
18:0-18:1	0.50	COD	47
16:0-18:1	0.58, 0.52, 0.40, 0.25	COD	58
	0.50	COD	47
	0.334, 0.250	COD	57
di-18:1	0.62, 0.57, 0.51, 0.40, 0.25	COD	58
	0.33	COD	47
di-18:0	0.47[c]	perfringolysin O (PFO)	55
di-16:0	0.49[c]	PFO	55
di-14:0	0.51[c]	PFO	55
18:0-18:1	0.42[c]	PFO	55
16:0-18:1	0.47[c]	PFO	33
	0.45[c]	PFO	33
	0.45	PFO	46
	0.44[c]	PFO	55
	0.44[c]	PFO	56
	0.28[c]	PFO, pH = 7.4	54
	0.24[c]	PFO, pH = 5.1	54
di-18:1	0.45	PFO-D4[d]	48
	0.45	anthrolysin O (ALO)-D4[d]	48
	0.41	PFO	48
	0.37[c]	PFO	55
	0.35	PFO	46
	0.34[c]	PFO	33
	0.26	ALO	48
	0.26[c]	PFO, pH = 7.4	54
	0.20[c]	PFO, pH = 7.0	54
di-(4Me-16:0)	0.31	PFO	48
	0.27	PFO-D4[d]	48
	0.27	ALO-D4[d]	48
	0.25	PFO	46

[a]Lipids are listed by the number of carbons and degree of unsaturation of their tails (e.g. DMPC is di-14:0-PC). [b]Characteristic χ_C refers to the one or several mole fraction(s) of cholesterol at or above which the accessibility of cholesterol increases sharply. Only characteristic $\chi_C \geq 0.20$ are listed. [c]This value was interpreted from a graph as the half-maximum of cytolysin binding. [d]This version of the protein is monomeric and does not cause pores to form in the membrane.

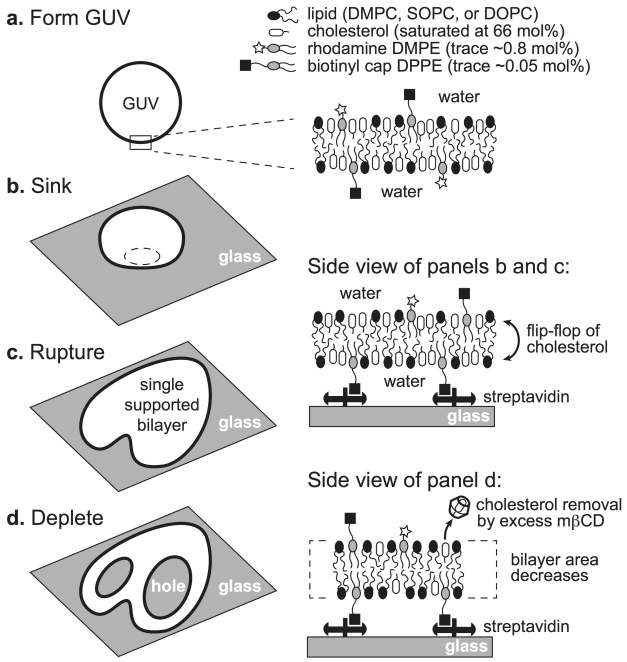

Figure 2.2: Overview of the experimental procedure. (a) A giant unilamellar vesicle (GUV) saturated with cholesterol at 66 mol% is produced via electroformation. (b) The GUV sinks to the bottom of the experimental chamber where it (c) ruptures onto a streptavidin-functionalized glass coverslip, forming a heart-shaped supported lipid bilayer (SLB). Cholesterol flip-flop is rapid between the upper and lower leaflets of the fluid bilayer.[24–27] (d) mβCD is added to the chamber, where it selectively removes cholesterol from the SLB. Large holes form in the SLB as cholesterol is depleted, and the bilayer area decreases.

(GUVs) onto a glass substrate coated with streptavidin that yields supported lipid bilayers (SLBs). Upon depletion of cholesterol with mβCD, a few large holes form in the bilayer, suggesting that strong bilayer-surface pinning interactions are minimized. We tackled the third challenge by aggregating published bilayer thickness and area per unit cell data and converting those values to molecular areas. An overview of our experimental procedure is shown in Figure 2.2 (full details appear in the Methods section).

It is important that we conduct our experiments on bilayers rather than monolayers —as has been achieved previously[32]— because large differences in miscibility behavior between monolayer and bilayer systems imply that cholesterol-phospholipid interactions differ in the two systems.[65] Also, our goal is to resolve disagreements about which models of cholesterol-lipid interactions best describe the accessibility of cholesterol in bilayer systems. The clearest

predictions from these models apply to bilayers comprised of a single lipid and cholesterol, which led us to use binary membranes in our experiments. Membranes composed of certain ternary mixtures of lipids and cholesterol are known to phase separate at common experimental temperatures.[19] Reports of two rates of cholesterol efflux from cells and from bilayers composed of ternary lipid mixtures[36,61,66,67] are challenging to interpret if the membrane demixes into coexisting liquid phases.

Here we show that the accessibility of cholesterol for removal by mβCD increases sharply above a single characteristic χ_C specific to the PC-lipid in the membrane. Our membranes are free of macroscopic phase separation. Our results show that cholesterol exists in multiple populations with distinct accessibilities in two-component PC-lipid membranes that appear otherwise homogeneous. Our method enables us to distinguish between different models of cholesterol-phospholipid interactions in lipid bilayers.

2.3 Results and Analysis

We added mβCD to an aqueous solution above a field of SLBs and recorded a time-series of micrographs to determine the rate at which cholesterol is depleted from the lipid bilayers. Full experimental details are compiled in the Methods section. A representative time-series of images for bilayers of DMPC and cholesterol appears in Fig. 2.3. We collected similar time-series for bilayers of SOPC and cholesterol and for bilayers of DOPC and cholesterol. As cholesterol is depleted from each bilayer, a few holes form and grow. We plot the fraction of each bilayer area remaining as a function of time after mβCD is added, $A_R(t)$. In Fig. 2.4 the mean of the experimental data ± two standard errors is shown in black, and the standard deviation of the data is shown in gray. Our goal is to use $A_R(t)$ to quantitatively determine how the rate of cholesterol depletion depends on χ_C.

Our approach to analyzing $A_R(t)$ is as follows: We define,

$$A_R(t) \equiv \frac{\text{area of bilayer at } t}{\text{area of bilayer at } t=0} = \frac{n_L + n_C(t)}{n_L + n_C(0)} \times \frac{a_{\text{avg}}(\chi_C[t])}{a_{\text{avg}}(\chi_C[0])}, \tag{2.1}$$

$$= \left(1 - \chi_C(0) + \frac{n_C(t)}{n_L + n_C(0)}\right) \times \frac{a_{\text{avg}}(\chi_C[t])}{a_{\text{avg}}(\chi_C[0])}, \tag{2.2}$$

where n_L is the number of PC-lipid molecules initially in the bilayer, χ_C is the mole fraction of cholesterol in the bilayer, n_C is the monotonically decreasing number of cholesterol molecules

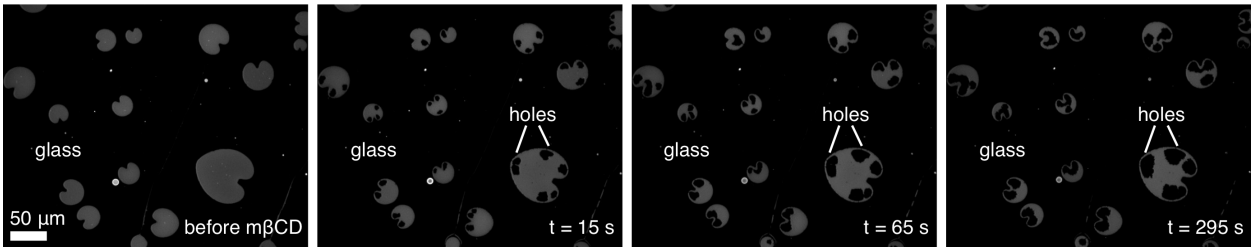

Figure 2.3: Micrographs of the cholesterol depletion process. Heart-shaped regions (gray) are individual supported lipid bilayers formed from the rupture of giant unilamellar vesicles onto a glass coverslip (black). mβCD is added at $t = 0$ s. mβCD removes cholesterol from the supported lipid bilayers. Large holes form in the bilayers as their areas decrease, further revealing the glass coverslip beneath them. DMPC/cholesterol bilayers are shown here, [mβCD] = 2.5 mM.

in the bilayer, and a_{avg} is the composition dependent average area per molecule in the bilayer.

Because we deplete with a gross excess of mβCD, the concentration of mβCD remains approximately constant throughout the experiment. Therefore, the rate of depletion for a given SLB varies with n_C only. If all cholesterol in the bilayer were equally accessible by mβCD and this accessibility were independent of χ_C, then the rate law governing the depletion process would be pseudo-first order in n_C with

$$-\frac{dn_C(t)}{dt} = k_1 n_C(t), \tag{2.3}$$

$$n_C(t) = n_C(0)e^{-k_1 t}, \tag{2.4}$$

where k_1 is the depletion rate constant. Then by Eq. 2.2,

$$A_R(t) = \left(1 - \chi_C(0) + \frac{n_C(0)}{n_L + n_C(0)}e^{-k_1 t}\right) \times \frac{a_{\text{avg}}(\chi_C[t])}{a_{\text{avg}}(\chi_C[0])}, \tag{2.5}$$

$$= \left(1 - \chi_C(0) + \chi_C(0)e^{-k_1 t}\right) \times \frac{a_{\text{avg}}(\chi_C[t])}{a_{\text{avg}}(\chi_C[0])}, \tag{2.6}$$

where k_1 is the single fitting parameter used to generate the one-population fit shown in Fig. 2.4 (blue line). This model underfits our data, implying that a model in which all cholesterol in the membrane is in a single population is inadequate to describe our system.

If instead there were two independent populations of cholesterol, one with high accessibility and one with low accessibility, then the depletion would be the sum of two pseudo-

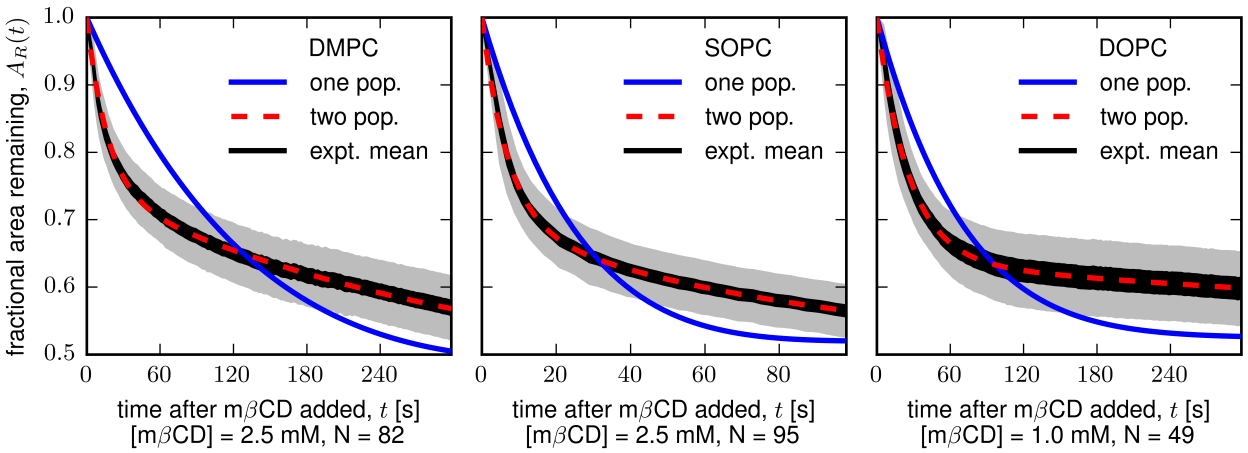

Figure 2.4: The fraction of bilayer area remaining as a function of time, $A_R(t)$, after addition of mβCD. $A_R(t)$ decreases as mβCD depletes cholesterol from the bilayer. The black region depicts our experimental mean ± two standard errors, and the gray region depicts the standard deviation of our data. The model with two cholesterol populations describes the data well (red dotted line), whereas the model with only one cholesterol population underfits the data (blue line). N is the number of replicate bilayers studied.

first-order processes with

$$-\frac{dn_C(t)}{dt} = k_s n_s(t) + k_f n_f(t), \tag{2.7}$$

$$n_C(t) = n_s(0)e^{-k_s t} + n_f(0)e^{-k_f t}, \tag{2.8}$$

where n_f and n_s are the numbers of cholesterol molecules in the two populations with corresponding rate constants k_f and k_s. We choose $k_f > k_s$ so that k_f (k_s) represents the fast (slow) cholesterol population. By Eq. 2.2,

$$A_R(t) = \left(1 - \chi_C(0) + \frac{n_s(0)}{n_L + n_C(0)}e^{-k_s t} + \frac{n_f(0)}{n_L + n_C(0)}e^{-k_f t}\right) \times \frac{a_{\text{avg}}(\chi_C[t])}{a_{\text{avg}}(\chi_C[0])}. \tag{2.9}$$

We then use the fact that $n_f(0) = n_C(0) - n_s(0)$, and define χ_s^0 as the initial mole fraction of the slow population of cholesterol, $\chi_s^0 \equiv n_s(0)/\left(n_L + n_C(0)\right)$, to obtain

$$A_R(t) = \left(1 - \chi_C(0) + \chi_s^0 e^{-k_s t} + \left(\chi_C(0) - \chi_s^0\right) e^{-k_f t}\right) \times \frac{a_{\text{avg}}(\chi_C[t])}{a_{\text{avg}}(\chi_C[0])}, \tag{2.10}$$

where χ_s^0, k_s, and k_f are the three fitting parameters used to generate the two population fit shown in Fig. 2.4 (red dotted line). This model describes our data well, and a summary of the fitting parameters is given in Table 2.2. This model is the simplest description of a

Table 2.2: Experimental parameters and fitting results for the two population model of cholesterol (Fig. 2.4 dotted red lines, Eq. 2.10).

Lipid	N^a	[mβCD]^b	$\chi_s^{0\,c}$	$k_s \times 10^3$ $(s^{-1})^d$	$k_f \times 10^3$ $(s^{-1})^e$
DMPC	82	2.5 mM	0.391 ± 0.002	2.38 ± 0.03	57.4 ± 1.2
SOPC	95	2.5 mM	0.312 ± 0.004	8.2 ± 0.2	138.2 ± 3.9
DOPC	49	1.0 mM	0.226 ± 0.004	0.98 ± 0.10	36.7 ± 0.8

[a]The number of replicate bilayers measured. [b]The concentration of mβCD used (see the Methods section). [c]Fitting parameter corresponding to the initial mole fraction of the slow population of cholesterol. [d]Fitting parameter corresponding to the rate constant for the depletion of the slow population of cholesterol. [e]Fitting parameter corresponding to the rate constant for the depletion of the fast population of cholesterol. The method of generating uncertainties in the fitting parameters is described in the Curve Fitting section.

membrane with more than one population of cholesterol. It is possible that there are more than two populations of cholesterol or that the two populations readily interconvert, but adding further complexity to the model is unwarranted by our data (see Fig. S3 in the Supporting Information for a three population model).

2.4 Discussion

We found evidence for two populations of cholesterol in bilayers containing cholesterol and either DMPC, SOPC, or DOPC. The fraction of cholesterol that is more highly accessible increases with the degree of unsaturation of the PC-lipid's acyl chains. These results in conjunction with the previous literature results in Table 2.1 enable us to assess current models of cholesterol-phospholipid interactions.

2.4.1 Models of cholesterol-phospholipid interactions

There are four commonly referenced descriptions of cholesterol-phospholipid interactions in membranes that yield distinct predictions about how the accessibility of cholesterol should vary with composition: These are the umbrella, superlattice, condensed-complex, and choles-

Table 2.3: Summary of models of cholesterol-phospholipid interactions in lipid membranes.

Model	# of characteristic χ_C[a] ($0.66 < \chi_C < 0.30$)	Dependent on PC-lipid head or tail?[b]
Umbrella (at solubility limit)	0	Head
Condensed-complex	1	Tail
Cholesterol bilayer domain	1	Both
Umbrella (regular distributions)	≥ 3	Head
Superlattice	≥ 3	Head

[a]The number of characteristic χ_C at which the accessibility of cholesterol is predicted to change sharply. [b]Statement of whether the predictions of the model vary with the structure of the phospholipid head, tail, or both.

terol bilayer domain models.

At the solubility limit of cholesterol in the bilayer, the umbrella model predicts non-specific cholesterol-phospholipid interactions that are independent of the PC-lipid tail.[68] The large hydrophilic PC-headgroups form a protective canopy under which cholesterol diffuses freely. Each PC-umbrella shields up to two molecules of cholesterol from water. This model successfully predicts that the solubility limit of cholesterol in PC-lipid bilayers is largely independent of PC-lipid tail structure,[16] with notable exceptions being polyunsaturated[69,70] and methylated[71] PC-lipids. However, by the shielding mechanism alone, all cholesterol in the bilayer should be equally accessible for removal by mβCD. Our results provide evidence that there are at least two populations of cholesterol with distinct accessibilities, and treating all cholesterol as equally accessible underfits our data (Fig. 2.4, blue line).

Both the umbrella and superlattice models predict that bilayers contain lattice-like, regular distributions of cholesterol and phospholipids at several characteristic values of χ_C. By the umbrella model, lattice formation is driven by unfavorable multibody cholesterol-phospholipid interactions; the energy of these interactions increases non-linearly as the number of cholesterol molecules per phospholipid increases.[68] By the superlattice model, long-range cholesterol-cholesterol repulsions drive lattice formation.[72] An essential similarity between these models is that both claim that the characteristic χ_C at which regular distributions form are independent of the degree of unsaturation of the PC-lipid tail.[58,68] The results

reported in references 57 and 58 are consistent with some of the predictions of these models. However, our results clearly show that the accessibility of cholesterol depends on the PC-lipid tail, with starkly different values of χ_s^0, k_s, and k_f for the three PC-lipids studied (Table 2.2). These models also predict a change in cholesterol accessibility at several values of χ_C. Our results show that a two-population model of cholesterol with a single characteristic χ_C is sufficient to describe our systems.

The third model, the condensed-complex model, predicts that cholesterol and phospholipids react reversibly to form thermodynamically stable complexes with a well-defined stoichiometry characteristic to the phospholipid tail.[39] These complexes behave as a third chemical species in the two-component bilayer. Cholesterol accessibility increases once χ_C exceeds the complex stoichiometry. At this point, the population of cholesterol that is more accessible exists in excess of the amount of cholesterol needed to fully partner with each PC-lipid. Our results, as well as the results reported in references 33,46–48,54–56, are consistent with this model: We found our data are well-described with two populations of cholesterol and that the characteristic χ_C at which cholesterol accessibility begins to increase varies with the degree of unsaturation of the PC-lipid tail.

The fourth model, the cholesterol bilayer domain model, states that cholesterol in excess of a threshold mole fraction, χ_{CBD}, forms submicroscopic domains of bilayer-thick, tail-to-tail cholesterol monohydrate that are soluble in the membrane.[73–76] Signatures of these domains in two-component PC-lipid bilayers have been interpreted from X-ray diffraction, neutron scattering, and electron paramagnetic resonance (Table 2.4).[77–82] Our results are also consistent with this model. The characteristic χ_C at which cholesterol accessibility begins to increase would correspond to the formation of cholesterol bilayer domains made of cholesterol in excess of χ_{CBD}; cholesterol in these domains would be less shielded from the aqueous phase than those in PC-lipid rich regions.

These four models need not be mutually exclusive. The cholesterol bilayer domain model makes predictions only about cholesterol concentrations above χ_{CBD}; it does not preclude the predictions of the condensed-complex model or the regular distributions predicted by the superlattice or umbrella models below χ_{CBD}. Attempts have been made to resolve the condensed-complex and superlattice models by treating the condensed-complexes as subunits

Table 2.4: Experimental reports of cholesterol bilayer domains in two-component PC-lipid bilayers.

PC-lipid[a]	χ_{CBD}[b]	Technique	Ref.
di-14:0	0.50	electron paramagnetic resonance	77
16:0-18:1	0.50		78
di-16:0	0.325	neutron scattering	79
di-16:0	0.54 ± 0.02	X-ray diffraction	80
di-14:0	0.44		82
	0.40		81
18:0-18:1	0.47		82
di-18:1	0.40		82

[a]Lipids are listed by the number of carbons and degree of unsaturation of their tails (e.g. DMPC is di-14:0-PC). [b]The mole fraction of cholesterol above which signatures of cholesterol bilayer domains are reported.

that aggregate to form larger superlattice clusters over time.[83] Also, for χ_C less than 0.50, the umbrella and superlattice models yield similar characteristic values of χ_C.[68]

2.4.2 Condensed-complex stoichiometry and χ_{CBD}

From our two cholesterol population model, we derived values pertinent to the condensed-complex and cholesterol bilayer domain models (Table 2.5). We determined the values of the phospholipid-cholesterol complex stoichiometries that result from applying the condensed-complex model to our data. This stoichiometry is equivalent to the ratio of the number of cholesterol molecules in the less accessible (slow) pool to the total number of PC-lipid molecules in the bilayer. We compute this ratio as,

$$\text{complex stoichiometry} = \frac{n_s(0)}{n_L} = \frac{\chi_s^0}{1 - \chi_C(0)}. \tag{2.11}$$

In the context of the cholesterol bilayer domain model, we determine the mole fraction of cholesterol above which cholesterol bilayer domains would form in the bilayer, χ_{CBD}. This quantity is approximated by assuming that all cholesterol in the more accessible population is located in cholesterol bilayer domains. This value is most directly comparable to the

Table 2.5: Values derived from the two cholesterol population model.

Lipid	Complex stoichiometry[a]	χ_{CBD}[b]	k_f/k_s[c]
DMPC	1.150 ± 0.006	0.535 ± 0.001	24.1 ± 0.4
SOPC	0.92 ± 0.01	0.479 ± 0.004	16.8 ± 0.4
DOPC	0.67 ± 0.01	0.399 ± 0.005	37.9 ± 3.3

[a]The average number of PC-lipid molecules complexed with a single cholesterol molecule in the context of the condensed complex-model. [b]The mole fraction of cholesterol above which cholesterol bilayer domains would be expected to exist in the context of the cholesterol bilayer domain model. This value is most directly comparable to the characteristic χ_C values in Table 2.1. [c]The ratio of depletion rate constants between the fast and slow populations of cholesterol. [a-c]The method of generating uncertainties is described in the Curve Fitting section.

characteristic χ_C values reported in Table 2.1. We determine,

$$\chi_{\mathrm{CBD}} = \frac{n_s(0)}{n_L + n_s(0)} = \frac{\chi_s^0}{1 - \chi_C(0) + \chi_s^0}. \tag{2.12}$$

We also compute the ratio of the depletion rate constants of the two populations of cholesterol (k_f/k_s).

2.4.3 Depletion rate coefficient

Because the two-component membranes we investigate appear homogeneous, it is natural to think of the depletion process as pseudo-first order in n_C with a composition-dependent rate coefficient of depletion, k_D:

$$-\frac{dn_C(t)}{dt} = k_D(\chi_C[t])n_C(t), \tag{2.13}$$

$$k_D(\chi_C[t]) = \frac{-1}{n_C(t)}\frac{dn_C(t)}{dt} \tag{2.14}$$

$$= \frac{-1}{\chi_C(t)\,(1 - \chi_C(t))}\frac{d\chi_C(t)}{dt}. \tag{2.15}$$

Our depletion rate coefficient is proportional to the average accessibility of all cholesterol in the bilayer. Encapsulated within k_D is the effect of the concentration of mβCD on the rate

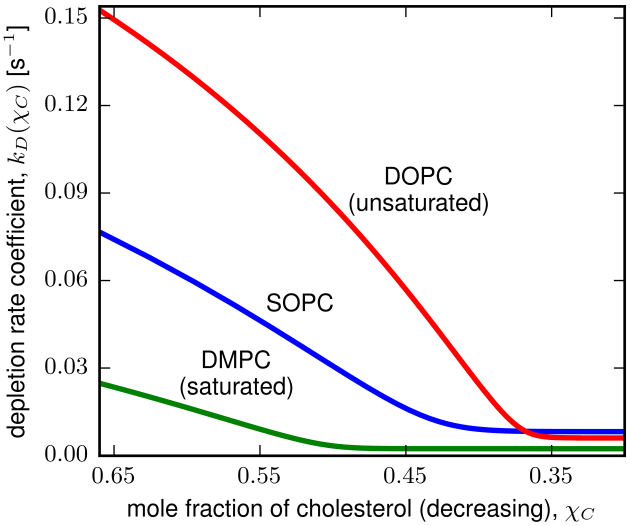

Figure 2.5: The depletion rate coefficient as a function of the mole fraction of cholesterol in the bilayer, $k_D(\chi_C)$. The rate coefficient decreases sharply as the more accessible population of cholesterol is depleted. The fraction of cholesterol in this population increases with increasing PC-lipid tail unsaturation from DMPC (green) to SOPC (blue) to DOPC (red). At a given χ_C, the rate coefficient increases with increasing lipid tail unsaturation. We treat the depletion process as second order in mβCD[22] and scale k_D for DOPC by a factor of 6.25.

of depletion. For purposes of comparison with other literature values, we treat the depletion as second order in mβCD[22] and therefore scale our results for k_D of DOPC by a factor of 6.25 (2.5^2) to account for differences in the concentration of mβCD used (Table 2.2).

In Figure 2.5, we show that at a given χ_C, k_D increases with the degree of unsaturation of the PC-lipid tails. This is consistent with cholesterol interacting more favorably with saturated lipids than unsaturated lipids.[53] k_D decreases sharply as the more readily accessible population of cholesterol is depleted. The proportion of cholesterol in this population at high χ_C increases with the degree of lipid tail unsaturation.

2.4.4 Advantages and disadvantages of the mβCD area depletion assay

With our area depletion assay, a single experiment yields data for up to fifteen individual SLBs over a wide range of cholesterol concentrations, enabling rapid acquisition of replicate data. The cholesterol-dependent cytolysin and cholesterol oxidase assays also report on the accessibility of membrane cholesterol but require a separate experiment for every χ_C tested.

In addition, the experimental observable in our assay, namely membrane area visualized by fluorescence microscopy, enables us to directly witness any evidence of large scale structural changes of the membrane during the course of our experiment. A disadvantage of our assay is that the signal to noise diminishes in the low-cholesterol regime ($\leq$ 30 mol%) because at these χ_C, a_{avg} increases sharply as cholesterol is removed, meaning that large changes in χ_C yield very small changes in the total bilayer area remaining. Our discussion focuses on the accessibility of cholesterol. A vast literature of complementary techniques exists to assess cholesterol-lipid interactions and has been reviewed by others.[84] As only one example, isothermal titration calorimetry detects non-ideal lipid-cholesterol mixing in bilayers at $\chi_C \geq 0.3$, although the membrane partition coefficient of cholesterol appears to increase with χ_C.[22]

2.5 Conclusion

We found that there are two populations of cholesterol with distinct accessibilities in lipid bilayers comprised of DMPC, SOPC, or DOPC at high concentrations of cholesterol. The accessibility of cholesterol decreases sharply as the more accessible population is depleted from the bilayer, yielding a single abrupt change in slope in all three traces of k_D versus χ_C in Figure 2.5. The proportion of cholesterol initially in the more accessible population increases with the degree of unsaturation of the PC-lipid tail. Treating the depletion rate coefficient as a measure of accessibility that is proportional to chemical activity,[32] our results are consistent with cholesterol activity being higher in membranes comprised of monounsaturated lipids as compared to those comprised of saturated lipids. Our results are consistent with the condensed-complex and cholesterol bilayer domain models of lipid membranes and complement previous experiments using different systems in order to build a body of work elucidating how the chemical potential of cholesterol changes with its mole fraction in membranes.[33,46–48,54–58] We converted our results into predictions about these two models (Table 2.5). Our assay enables robust determination of the accessibility of cholesterol in lipid bilayers as a function of both phospholipid structure and cholesterol concentration.

2.6 Methods

2.6.1 Chemicals

1,2-dimyristoyl-sn-glycero-3-phosphocholine (DMPC, di-14:0); 1-stearoyl-2-oleoyl-sn-glycero-3-phosphocholine (SOPC, 18:1-18:0); 1,2-dioleoyl-sn-glycero-3-phosphocholine (DOPC, di-18:1); 1,2-dipalmitoyl-sn-glycero-3-phosphoethanolamine-N-(cap biotinyl) (biotinyl cap DPPE); and 1,2-dimyristoyl-sn-glycero-3-phosphoethanolamine-N-(lissamine rhodamine B sulfonyl) (rhodamine DMPE) were from Avanti Polar Lipids (Alabaster, AL). Cholesterol was from Sigma-Aldrich (St. Louis, MO). All lipids were used without further purification and were stored at -20 °C. Biotinyl cap DPPE was stored in chloroform/methanol/water (65/35/8 by volume), and all other lipids were stored in chloroform. Streptavidin and mβCD were from Sigma-Aldrich. Glucose and sucrose were from Fisher Scientific (Waltham, MA). All water was purified to 18 MΩ-cm with a Barnstead filtration system from Thermo Scientific (Waltham, MA).

2.6.2 Giant unilamellar vesicle formation

GUVs were generated by electroformation as in previous experiments (Fig. 2.2a).[19] Electroformation was conducted using mixtures of PC-lipid/cholesterol/rhodamine DMPE/biotinyl cap DPPE (25/75/0.8/0.05 by mole) to produce GUVs saturated in cholesterol at 66 mol%; excess cholesterol precipitates as crystalline cholesterol monohydrate.[16,17] Briefly, 0.25 mg of lipids were dissolved in chloroform and spread onto two 37.5 x 25 mm glass slides coated with indium-tin-oxide (Delta Technologies, Loveland, CO). The lipid-coated slides were placed under vacuum for 30 minutes to remove solvent. Pairs of slides were assembled face-to-face separated by a 1 mm gap maintained by two Teflon spacers. The gap was filled with 200 mM sucrose and the edges were sealed with vacuum grease. The two indium-tin-oxide surfaces were connected to an AC voltage of 1.5 V at 10 Hz for 1 hour at 60 °C. The resulting GUV-rich solution was diluted with 3.5 mL of 200 mM sucrose at 60 °C and then cooled to room temperature (24-26 °C). This temperature is above the gel-liquid coexistence temperature of all vesicles studied.[85,86] All experiments reported here featured vesicles that ruptured smoothly onto solid supports and that exhibited uniform distributions of dye-labeled lipids.

We find that vesicles in the gel phase (e.g. 100% DMPC vesicles below 24 °C) often do not rupture smoothly and that the dye-labeled lipids often accumulate at the edges of the resulting SLBs. Experiments were performed within four hours of vesicle formation.

2.6.3 Supported lipid bilayer formation and cholesterol depletion

A 25 x 25 mm glass cover slip (Fisher Scientific) was plasma etched (Harrick, Ithaca, NY) for 50 seconds. 1.5 mL of 0.1 mg/mL streptavidin in water was deposited on the cover slip. After 20 minutes, the water was poured off, and the cover slip was adhered with vacuum grease to form the base of a cylindrical well with a radius of 10 mm and a height of 12 mm. The chamber was gently rinsed with water five times and placed on the stage of an inverted epifluorescence microscope.

1 mL of 200 mM glucose was added to the chamber, followed by 20-50 μL of GUV-rich solution. GUVs sank to the bottom of the chamber (Fig. 2.2b). Within 1-2 minutes, hundreds of vesicles ruptured onto the cover slip to create a field of heart-shaped SLBs spatially separated by bare glass (Figs. 2.2c and 2.3). The asymmetric rupture mechanism that produces heart-shaped SLBs has been explored previously,[87] and we found our protocol predominantly yields this rupturing pattern. The chamber was washed with 1 mL of 200 mM glucose ten times. Care was taken to ensure that SLBs were never directly exposed to air. After an initial image was collected, 2 mL of 3.75 mM (for membranes with DMPC or SOPC) or 1.5 mM (for membranes with DOPC) mβCD in 200 mM aqueous glucose was added to the experimental chamber, yielding 3 mL of 2.5 mM (for membranes with DMPC or SOPC) or 1 mM (for membranes with DOPC) mβCD in 200 mM aqueous glucose. Approximately 5 seconds later, images were collected every 2 s with 500 ms exposures for a total of 300 s (DMPC or DOPC) or 100 s (SOPC) (Figs. 2.2d and 2.3). All experiments were performed at 24-26 °C. Two different concentrations of mβCD were used because 2.5 mM mβCD removes cholesterol from DOPC bilayers too quickly to accurately measure the rate of area depletion, whereas 1 mM mβCD depletes cholesterol prohibitively slowly from SOPC and DMPC bilayers. In total, we obtained data from 82 distinct bilayers of cholesterol with DMPC, 95 with SOPC, and 49 with DOPC.

At concentrations lower than 5-20 mM, mβCD selectively removes cholesterol from PC-

lipid bilayers, leaving the phospholipids behind and the membrane intact.[22,23,88,89] As a control to ensure that our procedure does not remove significant amounts of PC-lipids from the bilayer, we performed our assay using SLBs of pure DMPC, SOPC, or DOPC. No area depletion was observed on the time scale of our experiment.

It is likely that mβCD pulls cholesterol from only the upper leaflet of the SLBs. Because the rate of cholesterol flip-flop is on the order of milliseconds in fluid phase lipid bilayers[24–27] and our experiment occurs on the order of seconds, we expect that cholesterol equilibrates across the leaflet of our bilayers faster than we could detect. If cholesterol flip-flop were hindered and cholesterol could only move between the two leaflets by edge diffusion, we would expect to see depletion rates vary with SLB size. We found no correlation between SLB size and cholesterol depletion rate (see Fig. S1 in Supporting Info), nor did we find evidence of an asymmetric distribution of cholesterol across the two leaflets in our observations.

2.6.4 Images and image processing

Epifluorescence microscopy was performed with a 10x objective on an inverted Nikon microscope (Melville, NY) with a Photometrics Coolsnap *fx* charge-coupled device camera (Tucson, AZ). All micrographs were analyzed using the open-source software package Fiji.[90] Each time series of images was converted to a series of binary images using Fiji's isodata algorithm. The number of pixels in each SLB as a function of time was determined using Fiji's "Analyze Particles" function. The fraction of bilayer area remaining is determined by dividing the area remaining of each bilayer by its initial area. We imaged 3-15 separate SLBs per experiment. Data for any bilayer with an initial area of fewer than 250 μm^2 was discarded to limit sensitivity to noise in the area measurement. Occasionally, over the course of an experiment, a free-floating GUV or other lipid debris drifted over one of the bilayers being imaged, briefly obfuscating measurement of the bilayer area. In this case, the affected data points were discarded.

2.6.5 Curve fitting

We fit all data using the freely available Python module PyMC.[91] PyMC implements Markov chain Monte Carlo algorithms to provide a computationally tractable approach to Bayesian

curve fitting. For each fit, we started with a uniform prior probability distribution and generated 100,000 samples of the posterior distribution using a likelihood function that assumes independent, unbiased, and normally distributed errors in the data. The first 20,000 of these samples were discarded as 'burn-in' to avoid sampling from the Markov chain before it reached its equilibrium distribution. We determined the means and standard deviations of the fitting parameters given in Table 2.2 and derived values given in Table 2.5 directly from these sets of 80,000 samples (see Fig. S2 for plots of the sampled posterior distribution).

2.6.6 Bilayer area per molecule

We aggregated published bilayer electron density peak-to-peak distances, d_{pp}, determined by X-ray diffraction[29,82,92] and area per unit cell data, A_{UC}, determined by neutron scattering[93,94] or jointly analyzed neutron and X-ray scattering[30,95] for bilayers comprised of cholesterol and either DMPC, SOPC, or DOPC at 30 °C (see Tables S1-S5 in Supporting Information for all data used).

From X-ray experiments, we determined the thickness of the approximately incompressible hydrocarbon region of the bilayer as a function of mole fraction of cholesterol, $d_{HC}(\chi_C)$, as:

$$d_{HC}(\chi_C) = d_{pp}(\chi_C) - 2d_{H1}, \tag{2.16}$$

where d_{H1} is the distance from the peak of the X-ray scattering electron density profile to the interface of the hydrocarbon region of the bilayer as determined by the joint analysis of X-ray and neutron scattering data for single-component bilayers consisting of the appropriate PC-lipid.[30,95] It is likely that d_{H1} varies with χ_C, but there are no published values of this relationship for the systems we studied. We therefore approximated d_{H1} as constant with respect to χ_C.

From d_{HC}, we determined the average area per molecule in the bilayer, a_{avg}, as

$$a_{\mathrm{avg}}(\chi_C) = \frac{2V_{HC}(\chi_C)}{d_{HC}(\chi_C)}, \tag{2.17}$$

where V_{HC} is the average volume per molecule in the hydrophobic portion of the bilayer,

Table 2.6: Fitting parameters for the average area per molecule in a bilayer as a function of mole fraction of cholesterol, $a_{\text{avg}}(\chi_C)$ (Fig. 2.6, Eq. 2.20).

Lipid	p_1 (Å^2)	p_2 (Å^2)	p_3
DMPC	38.1 ± 2.4	21.0 ± 2.4	5.1 ± 1.4
SOPC	38.5 ± 3.0	26.8 ± 2.9	2.9 ± 0.7
DOPC	36.5 ± 2.1	31.1 ± 2.1	2.2 ± 0.3

computed as

$$V_{HC}(\chi_C) = (V_L - V_H) \times (1 - \chi_C) + V_C \chi_C, \tag{2.18}$$

and where V_L, V_H, and V_C are the reported volumes of the PC-lipid,[96,97] the PC-headgroup,[98,99] and a single cholesterol molecule in a PC-lipid bilayer,[97] respectively. It is likely that cholesterol does not lie entirely within the hydrocarbon portion of the bilayer,[29,33] but no value for the fraction of excluded volume has been reported. We therefore approximated cholesterol as being completely located within the hydrocarbon region of the bilayer.

From neutron scattering experiments, we determined a_{avg} as

$$a_{\text{avg}}(\chi_C) = A_{UC}(\chi_C) \times (1 - \chi_C)\,. \tag{2.19}$$

We found that a_{avg} is well-described as exponentially increasing with decreasing χ_C,

$$a_{\text{avg}}(\chi_C) \approx p_1 + p_2 e^{-p_3 \chi_C}, \tag{2.20}$$

where p_1, p_2, and p_3 are the fitting parameters (Fig. 2.6). The fitting parameters are summarized in Table 2.6. We do not assign a physical meaning to these fitting parameters or relationship, and we use this analytic form only as an approximation of a_{avg} to enable further analysis.

2.7 Supporting Information

All data used to determine the average area per molecule in a bilayer as a function of the mole fraction of cholesterol, $a_{\text{avg}}(\chi_C)$, are given in Tables 2.7-2.11. d_{pp} is the electron

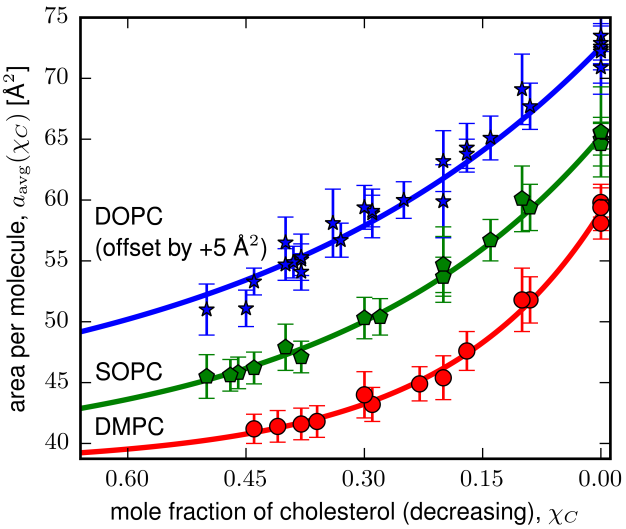

Figure 2.6: The average area per molecule as a function of mole fraction of cholesterol, $a_{\text{avg}}(\chi_C)$, for two-component bilayers of cholesterol with DMPC (circles, red line), SOPC (pentagons, green line), or DOPC (stars, blue line). All data (symbols) shown here are determined from previously reported measurements of bilayer thickness or area per unit cell conducted at 30 °C.[29,30,82,92–95] The average area per molecule is well-approximated as exponentially increasing with decreasing cholesterol mole fraction (colored lines). DOPC data is offset (increased) by 5 Å^2 to avoid overlap with the SOPC data.

density peak-to-peak distance as determined by X-ray diffraction. d_{H1} is the distance from the peak of the electron density profile to the interface of the hydrocarbon region of the bilayer as determined by the joint analysis of X-ray and neutron scattering data. A_{UC} is the area per unit cell as determined by neutron scattering or the joint analysis of X-ray and neutron scattering data. V_L, V_H, and V_C are the volumes of a PC-lipid, a PC-headgroup, and cholesterol in a bilayer, respectively.

Data and uncertainties from references 82, 29, and 93 were interpreted from graphs. Uncertainties in 95, 30, and 92 were reported as less than 2%; we treated the uncertainty as ±2%.

The equation of fit for the three population fit is

$$A_R(t) = \left(1 - \chi_C(0) + \chi_1 e^{-k_1 t} + \chi_2 e^{-k_2 t} + (\chi_C(0) - \chi_1 - \chi_2) e^{-k_3 t}\right) \times \frac{a_{\text{avg}}(\chi_C[t])}{a_{\text{avg}}(\chi_C[0])}, \quad (2.21)$$

where χ_1, χ_2, k_1, k_2, and k_3 are the five fitting parameters.

Table 2.7: Literature d_{pp} and A_{UC}, and calculated a_{avg} values for DMPC.

χ_C	Lit. d_{pp} (Å)	Lit. A_{UC} (Å^2)	Ref.	Calc. a_{avg} (Å^2)
0.00	34.9 ± 0.7	59.8 ± 1.2	30	59.8 ± 1.2
0.00	35.3 ± 0.3		29	59.4 ± 1.9
0.00	35.9 ± 0.1		82	58.1 ± 1.3
0.09	38.4 ± 0.1		82	51.8 ± 1.9
0.10	38.3 ± 0.5		29	51.8 ± 2.6
0.17	40.3 ± 0.1		82	47.6 ± 1.6
0.20	41.5 ± 0.4		29	45.4 ± 1.8
0.23	41.6 ± 0.1		82	44.9 ± 1.4
0.29	42.5 ± 0.1		82	43.2 ± 1.4
0.30	41.8 ± 0.5		29	44.0 ± 1.9
0.36	43.2 ± 0.1		82	41.8 ± 1.3
0.38	43.3 ± 0.1		82	41.6 ± 1.3
0.41	43.3 ± 0.1		82	41.4 ± 1.2
0.44	43.3 ± 0.1		82	41.2 ± 1.2

Table 2.8: Literature d_{pp} and A_{UC}, and calculated a_{avg} values for SOPC.

χ_C	Lit. d_{pp} (Å)	Lit. A_{UC} (Å^2)	Ref.	Calc. a_{avg} (Å^2)
0.00	38.7 ± 0.8		92	65.6 ± 3.7
0.00	38.6 ± 0.8	65.5 ± 1.3	30	65.5 ± 1.3
0.00	39.0 ± 0.1		82	65.0 ± 1.3
0.00	39.2 ± 0.3		29	64.6 ± 1.8
0.09	40.8 ± 0.1		82	59.4 ± 1.9
0.10	40.3 ± 0.5		29	60.1 ± 2.7
0.14	41.7 ± 0.1		82	56.7 ± 1.7
0.20	42.1 ± 0.5		29	54.7 ± 2.3
0.20	42.1 ± 0.8		92	54.7 ± 3.1
0.20	42.7 ± 0.1		82	53.7 ± 1.6
0.28	43.8 ± 0.1		82	50.4 ± 1.5
0.30	43.6 ± 0.3		29	50.3 ± 1.7
0.38	44.8 ± 0.1		82	47.1 ± 1.3
0.40	43.9 ± 0.5		29	47.9 ± 1.9
0.44	44.6 ± 0.1		82	46.2 ± 1.3
0.46	44.6 ± 0.1		82	45.8 ± 1.3
0.47	44.6 ± 0.1		82	45.6 ± 1.3
0.50	44.2 ± 0.5		29	45.5 ± 1.8

Table 2.9: Literature d_{pp} and A_{UC}, and calculated a_{avg} values for DOPC.

χ_C	Lit. d_{pp} (Å)	Lit. A_{UC} (Å^2)	Ref.	Calc. a_{avg} (Å^2)
0.00		68.5 ± 2.3	93	68.5 ± 2.3
0.00	36.6 ± 0.1		82	67.9 ± 1.4
0.00	36.7 ± 0.3		29	67.6 ± 1.9
0.00	36.9 ± 0.7		92	67.2 ± 3.5
0.00	36.8 ± 0.7	67.4 ± 1.3	95	67.4 ± 1.3
0.00		65.9 ± 1.3	94	65.9 ± 1.3
0.09	38.0 ± 0.1		82	62.7 ± 1.9
0.10	37.2 ± 0.5		29	64.1 ± 2.9
0.14	38.7 ± 0.1		82	60.1 ± 1.8
0.17		71.5 ± 2.4	93	59.3 ± 2.0
0.17		70.8 ± 1.4	94	58.8 ± 1.2
0.20	39.0 ± 0.5		29	58.2 ± 2.5
0.20	40.9 ± 0.8		92	54.9 ± 3.0
0.25	40.2 ± 0.1		82	55.0 ± 1.5
0.29		76.2 ± 1.8	94	54.1 ± 1.3
0.29		76.0 ± 2.9	93	53.9 ± 2.0
0.30	39.9 ± 0.3		29	54.4 ± 1.8
0.33	41.2 ± 0.1		82	51.7 ± 1.4
0.34		79.3 ± 4.2	93	53.1 ± 2.8
0.38		81.1 ± 3.0	93	50.3 ± 1.9
0.38	41.6 ± 0.1		82	50.1 ± 1.3
0.38		79.2 ± 2.4^a	94	49.1 ± 1.5
0.39	41.6 ± 0.1		82	49.9 ± 1.3
0.40	40.4 ± 0.5		29	51.5 ± 2.1
0.40	41.6 ± 0.1		82	49.7 ± 1.3
0.44		86.2 ± 1.9	93	48.3 ± 1.1
0.45		83.9 ± 2.7^a	94	46.1 ± 1.5
0.50		91.9 ± 4.1	93	46.0 ± 2.1

[a]The authors reported signatures of pauci-lamellar vesicles in this sample.

Table 2.10: Literature d_{H1} values.

Lipid	d_{H1} (Å)	Ref.
DMPC	4.61 ± 0.09^a	30
SOPC	4.35 ± 0.09^a	30
DOPC	3.9 ± 0.1^a	95

[a]There are no published values for the χ_C dependence of d_{H1} for these phospholipids, so we estimated uncertainties at $\pm 5\%$ for all $\chi_C > 0$.

Table 2.11: Literature V_L, V_H, and V_C values.

Lipid	V_L (Å^3)	V_H (Å^3)	V_C (Å^3)
DMPC ($\chi_C < 0.24$)	1099.6 ± 0.5^a	325 ± 6^c	565.1 ± 3.4^a
DMPC ($\chi_C \geq 0.24$)	1076.8 ± 1.3^a	325 ± 6^c	637.5 ± 1.8^a
SOPC	1309.5 ± 1.3^b	325 ± 6^c	630 ± 10^a
DOPC	1302.2 ± 0.4^a	325 ± 6^c	632.9 ± 0.9^a

[a]Reference 97. If not reported, the uncertainty was obtained by refitting published data. [b]Reference 96. [c]References 98 and 99. Uncertainty estimated from the spread of published values.

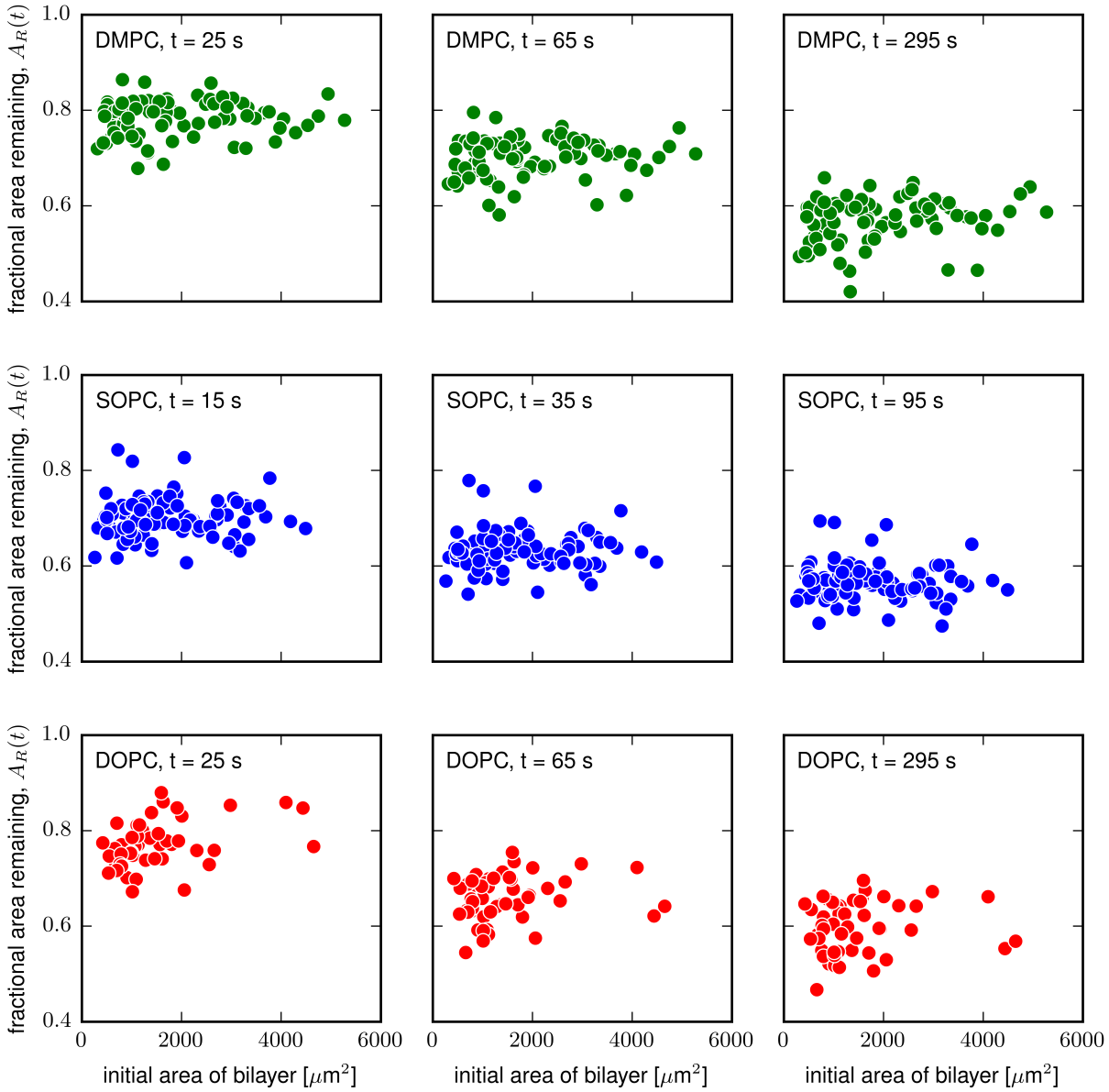

Figure 2.7: There is no apparent correlation between the initial area of the supported lipid bilayer and the fraction of bilayer area remaining as a function of time after mβCD is added, $A_R(t)$, for the systems we studied.

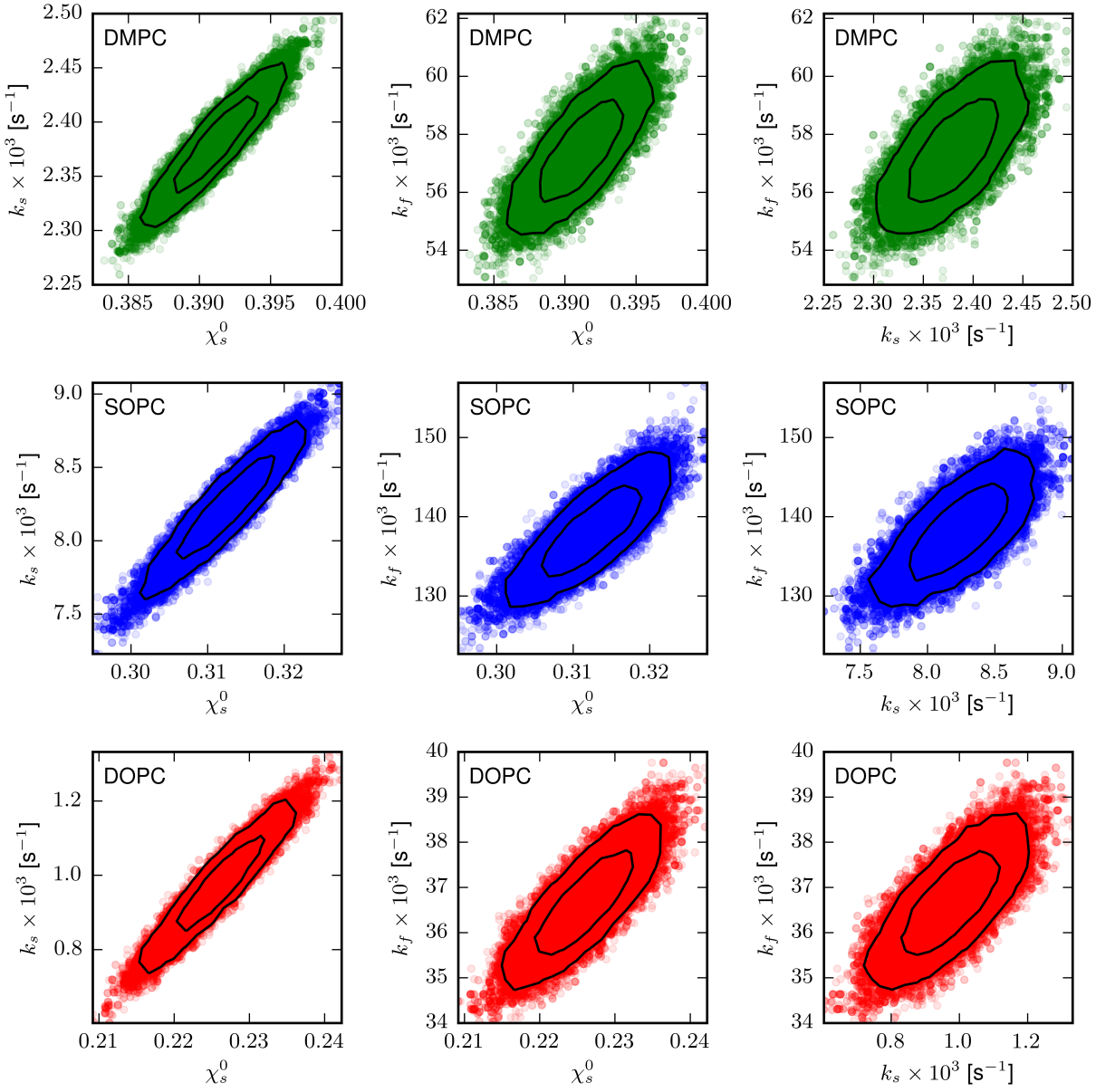

Figure 2.8: Samples of the posterior distribution of fitting parameters corresponding to the two cholesterol population model (see Fig 4, Table 2, and Eq. 10). Contours correspond to one and two standard deviations of the marginalized posterior samples.

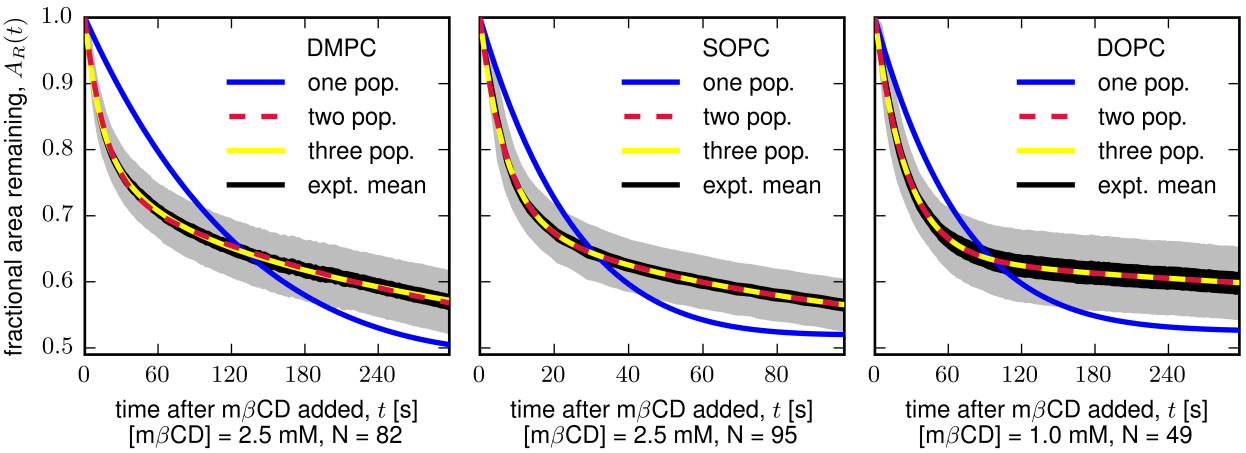

Figure 2.9: The fraction of bilayer area remaining as a function of time, $A_R(t)$ after addition of mβCD. The black region depicts our experimental mean ± two standard errors, and the gray region depicts the standard deviation of our data. The model with two cholesterol populations (three fitting parameters) describes our data well (crimson dotted line, main text eq. 10). The model with one cholesterol population (one fitting parameter, main text eq. 6) underfits our data (blue line). The model with three cholesterol populations (five fitting parameters, SI eq. 2.21) is unwarranted by our data (yellow line).

We define the average area per molecule ratio as follows:

$$a_R(\chi_C) = \frac{a_{\text{avg}}(\chi_C)}{a_{\text{avg}}(\chi_C = 0.66)}. \tag{2.22}$$

2.8 Acknowledgements

This research was funded by the National Science Foundation (MCB-07444852 and MCB-1402059). J.P.L. and N.T. were supported by National Science Foundation Graduate Research Fellowships DGE-0718124 and DGE-1256082, respectively. T.P. was supported by the Raymond and Beverly Sackler Foundation and the Fondation Bettencourt Schueller. The authors thank Matthew C. Blosser for comments on the manuscript.

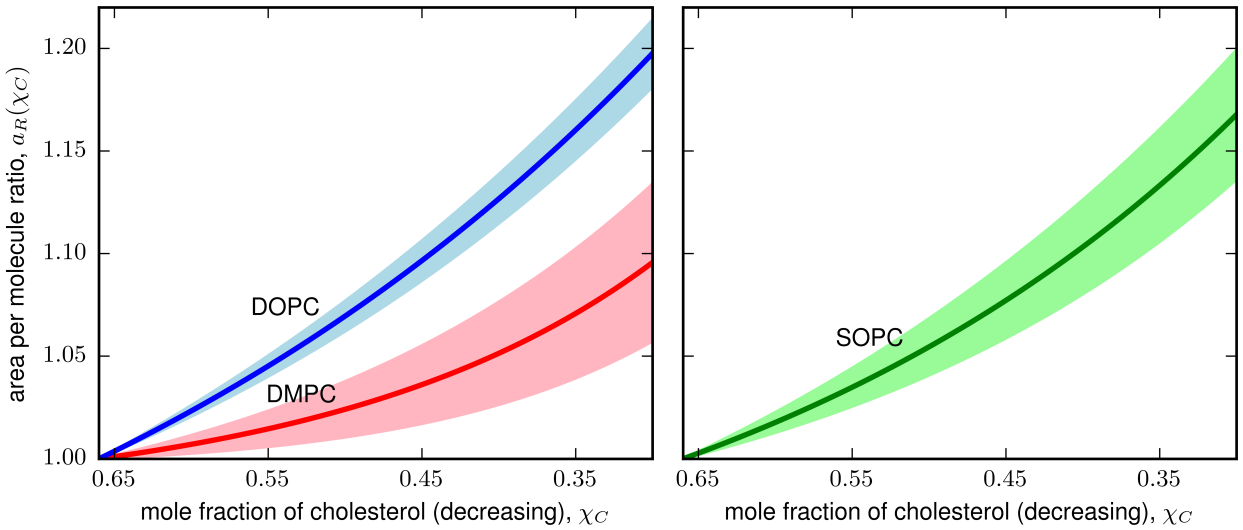

Figure 2.10: The average area per molecule ratio as a function of the mole fraction of cholesterol, $a_R(\chi_C)$ (solid lines) and the uncertainty in these values (one standard deviation, encompassed by the shaded area overlaying each line). Eq. 1 of the main text shows how the observable of our experiments, the fraction of bilayer area remaining as a function of time $A_R(t)$, is proportional to the ratio of the average area per molecule in the bilayer at time t and the average area per molecule in the bilayer at time $t = 0$. This figure shows that over the regime of $\chi_C > 0.3$ in which our experiment takes place, uncertainty resulting from $a_R(\chi_C)$ is small.

Chapter 3

A PLAUSIBLE EXPLANATION OF THE LINK BETWEEN SATURATED FATS AND HYPERCHOLESTERMIA

It is well-established that diets high in saturated fats are hypercholesterolemic in comparison to diets high in monounsaturated fats.[52,100,101] It is also known that the lipid composition of human red blood cells depends heavily on long-term dietary fat intake (Ref. 102 and references therein). In particular, populations of humans who consume high levels of saturated fats have increased percentages of saturated fats in the membranes of their red blood cells, whereas those who consume high levels of monounsaturated fats have increased percentages of monounsaturated fats in their red blood cells.[102]

Likewise, the surface accessibility of cholesterol for removal from a model membrane comprised of cholesterol and a single phosphatidylcholine (PC)-lipid has been shown to increase sharply above a threshold cholesterol concentration.[4,33,46–48,54–56] This threshold concentration increases with an increasing degree of saturation of the acyl tails of the PC-lipid. In other words, for a given cholesterol concentration, the accessibility of cholesterol in a saturated PC-lipid bilayer is lower than the accessibility of cholesterol in an unsaturated PC-lipid bilayer. Cholesterol accessibility is hypothesized to be proportional to the chemical activity, or effective concentration, of cholesterol.[38]

Recently, Radhakrishnan and co-workers have demonstrated that the accessibility of cholesterol in a mammalian cell's plasma membrane and endoplasmic reticulum increases sharply above the physiological set point of 35 mol% cholesterol for the plasma membrane[49] and 5 mol% cholesterol for the endoplasmic reticulum.[46] In the case of the endoplasmic reticulum, this cholesterol concentration set point is equal to that at which SREBP-2 activation is halted.[46] This halting leads to the down-regulation of cholesterol synthesis and uptake.[103–106]

Lange and Steck have long hypothesized that cholesterol homeostasis is mediated by

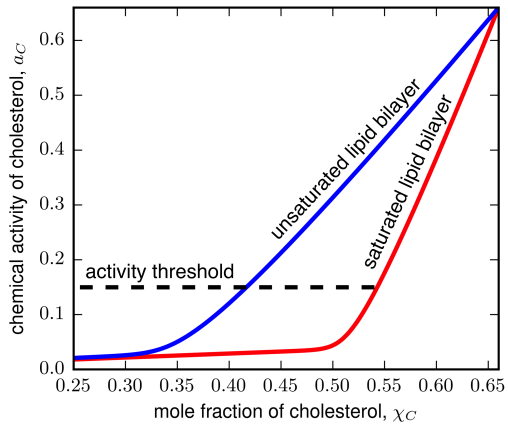

Figure 3.1: Schematic of the chemical activity (effective mole fraction) of cholesterol, a_C versus the (actual) mole fraction of cholesterol, χ_C. The values plotted here are in qualitative agreement with results from Ref. 4. For membranes with the same total mole fraction of cholesterol, the chemical activity of cholesterol in a membrane composed of unsaturated lipids (blue) is greater than that of cholesterol in a membrane composed of saturated lipids (red). It is possible that saturated fats decrease a_C in cells, causing the cells to produce cholesterol in excess of the desired physiological set point. In this figure, it is assumed that the solubility limit of cholesterol in all membranes is 66 mol%.

'active' cholesterol in excess of the physiological set point.[35,40,41,44,107] It is plausible that saturated fats induce hypercholesterimia by reducing the activity of cholesterol in cellular membranes with respect to the total concentration of membrane cholesterol (Fig. 3.1); the cell maintains homeostasis of cholesterol activity, not cholesterol total concentration. At high absolute concentrations of cholesterol, the plasma membrane may act as a nucleation site for the formation of pathological cholesterol crystals.[76]

Chapter 4

PRELIMINARY WORK WITH HYDROXYPROPYL-α-CYCLODEXTRIN

In 2013, Huang and London reported that hydroxypropyl-α-cyclodextrin (HPαCD) selectively removes phospholipids from model membranes, leaving cholesterol behind.[23] This inspired graduate student Christina Faller, under my guidance, to begin replicating my work from Ref. 4 using HPαCD in place of mβCD, and using an initial χ_C that is low in place of an initial $\chi_C = 0.66$. The reason we are doing these experiments are twofold: First, we want to provide further evidence that there are two populations of cholesterol in the composition range of $\chi_C \geq 0.3$. In particular, we will be able to elucidate effects of systematic error in our mβCD experiments by comparing our previous results with the HPαCD results. Second, depletion with HPαCD may enable us to probe bilayer compositions of $\chi_C < 0.3$ that were problematic in our previous experiments. Specifically, in our mβCD experiment as we deplete cholesterol from the bilayer the average area per molecule increases. When χ_C drops below 0.3, the area depletion caused by removing cholesterol is almost entirely negated by the increase in average area per molecule of the bilayer. In contrast, when depleting phospholipids with HPαCD, the average area per molecule will decrease as the depletion occurs, which will amplify the decrease in bilayer area. HPαCD may enable us to test predictions about regular distributions of cholesterol at compositions of $\chi_C \leq 0.3$.

Our main accomplishment on this project thus far has been mapping out the appropriate concentration of HPαCD to use such that the bilayer maintains its structural integrity while providing rapid enough depletion of PC-lipid to minimize the need to refocus the microscope during the experiment. Our preliminary HPαCD results are given in Table 4.1.

Two caveats are relevant for future graduate students who might continue this project. First, the mechanism by which HPαCD pulls different phospholipids from the bilayer may be different for each lipid type. Experimental results will reveal if the rate of depletion is

Table 4.1: Preliminary HPαCD depletion concentration screening results

PC-lipid	initial χ_C	[HPαCD] (mM)	comment on [HPαCD]
di-14:0	0.30	12.5	Too low
		25.0	**Good**
		50.0	Too high
	0.50	12.5	Too low
		25.0	**Good**
		50.0	Too high
18:0-18:1	0.30	25.0	Too low
		50.0–75.0	**Good**
		100.	Too high
	0.50	12.5	Too low
		25.0–50.0	**Good**
		100.	Too high
di-18:1	0.30	25.0	Too low
		37.5–50.0	**Good**
		75.0	Too high
	0.50	25.0	Too low
		100.0	Too high

first order or not for each lipid, but a comparison of absolute rate across different lipid types will not be meaningful if the mechanisms are different. Second, if phospholipid-phospholipid interactions are more favorable than phospholipid-cholesterol interactions, the first population of phospholipid that is depleted by HPαCD could actually be the population that interacts more strongly with cholesterol. If this is the case, as phospholipids interacting with cholesterol are removed, cholesterol will diffuse rapidly into the cholesterol-poor regions of the bilayer, which will increase the apparent size of the first pool of phospholipids.

Chapter 5

TERNARY PHASE DIAGRAMS OF MIXTURES OF DI-18:1-PC, DI-16:0-PC, AND EITHER β-SITOSTEROL, STIGMASTEROL, OR ERGOSTEROL

All images and transition temperatures in this chapter were recorded by undergraduate Ranee James.

5.1 Introduction

Giant unilamellar vesicles (GUVs) comprised of ternary mixtures of a phospholipid with a low melting temperature, T_{melt}, a phospholipid with a high T_{melt}, and cholesterol are known to exhibit liquid-liquid phase separation over a wide range of temperatures and compositions.[18,19] In 2005, Beattie et al. showed that 1:1:1 mixtures of di-18:1-PC, di-16:0-PC, and certain cholesterol analogues (namely, epicholesterol, dihydrocholesterol, or 25-hydroxycholesterol) exhibit liquid-liquid phase separation, whereas mixtures containing structurally similar cholesterol analogues (namely cholestenone, coprostanol, or lanosterol) do not (Fig. 5.1).[60] Small changes in sterol structure also yield large differences in sterol solubility limit: cholesterol is soluble up to 65-70 mol% in PC-lipid bilayers, whereas its analogues β-sitosterol (∼ 40 mol%), stigmasterol (20-25 mol%), and ergosterol (∼ 35 mol%) have far lower solubility limits (Fig. 5.3).[16,17]

Here we explore the phase behavior of GUVs comprised of di-18:1-PC, di-16:0-PC, and the naturally abundant cholesterol analogues β-sitosterol, stigmasterol, and ergosterol. β-sitosterol and stigmasterol are the two most common phytosterols (sterols found in plants), whereas ergosterol is the primary sterol in fungi and protozoa. These sterols are abundant in cellular plasma membranes, with plant plasma membranes having a phytosterol:phospholipid molar ratio of ∼0.6:1 (∼70% β-sitosterol and ∼20% stigmasterol) and yeast plasma membranes possessing an ergosterol:phospholipid ratio of ∼0.5:1.[12,108] For comparison, mammalian plasma membranes have a cholesterol:phospholipid molar ratio of ∼1:1.[12]

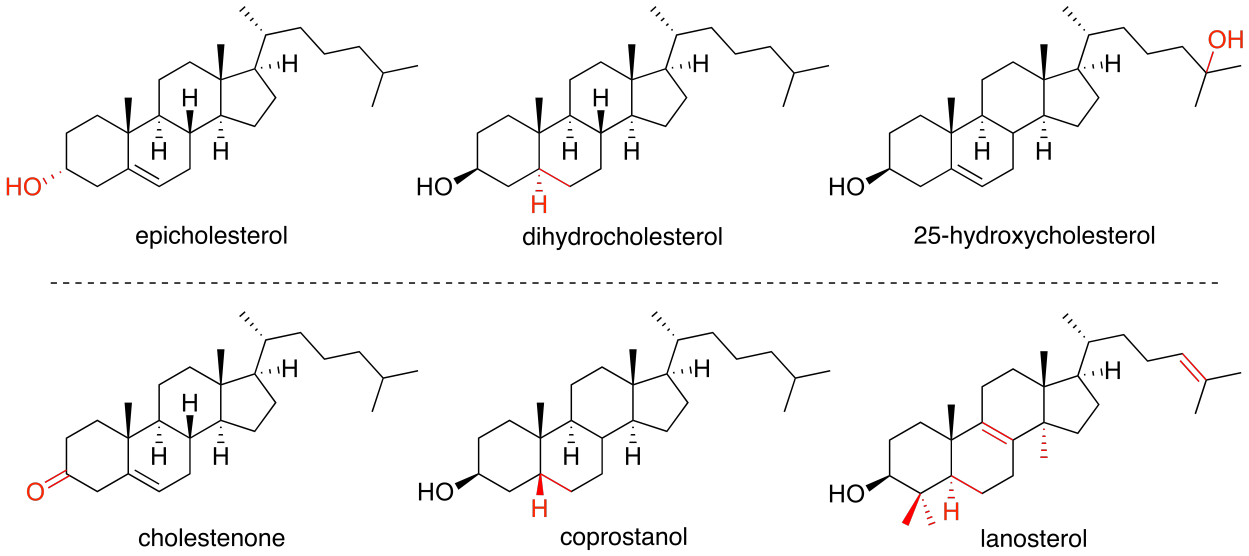

Figure 5.1: Chemical structures of cholesterol-analogues epicholesterol, dihydrocholesterol, 25-hydroxycholesterol, cholestenone, coprostanol, and lanosterol with differences from cholesterol drawn in red (see Fig. 5.2). GUVs comprised of 1:1:1 di-18:-1-PC, di-16:0-PC and epicholesterol, dihydrocholesterol, or 25-hydroxycholesterol (top) exhibit liquid-liquid phase separation, whereas those containing cholestenone, coprostanol, or lanosterol (bottom) do not.[60]

Mapping miscibility phase diagrams of membranes composed of lipids and sterols is important because there is still much that is unknown about which structural attributes of a sterol are required for a membrane to achieve liquid-liquid phase separation. This topic relates to the literature in three ways. First, if liquid-liquid phase separation is a mechanism for raft formation in biological membranes, it is unknown if rafts could form in biological systems free of cholesterol.[18] In this case, showing that phytosterols and ergosterol induce liquid-liquid phase separation over a wide range of temperatures and membrane compositions would imply that the lipid raft hypothesis is not unique to animal cell membranes. Second, providing miscibility phase diagrams of systems containing non-cholesterol sterols will enable theorists to test the flexibility of current models of membrane phase behavior by simulating systems with cholesterol analogues. Third Toulmay and Prinz recently discovered micron-scale lipid domains in the vacuoles of live yeast cells;[109,110] understanding the phase behavior of a simplified version of the vacuole will be key to interpreting these new results.

5.2 Assigning phase behavior

All GUVs are made with 0.8 mol% Rhodamine DMPE. This fluorescent, headgroup-labeled lipid is sterically bulky and partitions to the less ordered membrane phase of the GUV. We identify which phases are present in the membrane at a given membrane composition and temperature by identifying which phase is enriched in the fluorescently-labeled lipid and by observing the shape and merging behavior of phase-separated domains.

5.2.1 No phase separation

A membrane that exhibits no phase separation is characterized by a macroscopically homogenous distribution of Rhodamine DMPE across the surface of the GUV.

5.2.2 Liquid-liquid coexistence

A membrane that exhibits coexisting liquid phases is characterized by two features: first, the minority phase forms circular domains to minimize the energy penalty due to line tension; second, when two domains come into contact they readily and smoothly coalesce to form a new circular domain.

5.2.3 Gel-liquid coexistence

A membrane that exhibits gel-liquid coexistence is differentiated from one that exhibits liquid-liquid coexistence in two ways: first, gel domains are often noncircular; second, when two gel domains come into contact, they do not merge into a single, circular domain.

5.2.4 Gel-liquid-liquid coexistence

Gel-liquid-liquid (or three-phase) coexistence can be difficult to differentiate from liquid-liquid coexistence for two reasons. First, gel phase domains are typically embedded within liquid-ordered phase domains. Second, Rhodamine DMPE poorly labels both the liquid-ordered phase and the gel phase. Domains of each of these phases appear equally dark in fluorescence micrographs. The signature of three-phase coexistence is the observation of circular domains merging to form noncircular, smooth-edged domains (e.g. ovals or hourglasses). Noncircular, smooth-edged domains form when two liquid-ordered domains, each enveloping a gel subdomain, coalesce; the inability of the two gel subdomains to merge prevents the final coalesced structure from appearing circular.

5.3 Results and Discussion

The ternary phase diagrams of di-18:1-PC, di-16:0-PC, and β-sitosterol, stigmasterol, or ergosterol are shown in Fig. 5.4. An image of a characteristic vesicle from each composition is shown in Fig. 5.5. For purposes of comparison, the phase diagram of di-18:1-PC, di-16:0-PC, and cholesterol is shown in Fig. 5.2.

It is immediately evident that a large fraction of the symbols in the phase diagrams for GUVs containing either β-sitosterol or stigmasterol are circles with colored interiors. This result means that these systems exhibit liquid-liquid phase separation over a wide range of compositions below the solubility limit of the sterol in the bilayer. T_{mix} for these systems are a few degrees lower than the analogous systems containing cholesterol, implying that phase separation is slightly less favored in GUVs with β-sitosterol or stigmasterol than it is in GUVs with cholesterol. Structurally, this makes sense because cholesterol is known to partition somewhat preferentially to the liquid-ordered phase;[111] if phase separation arises

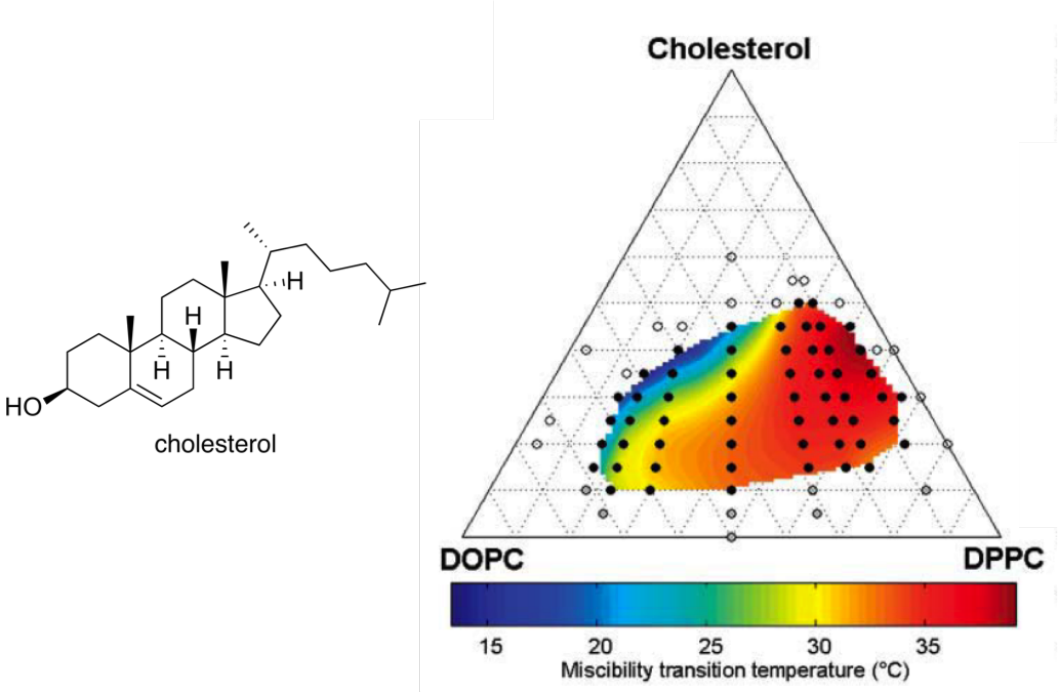

Figure 5.2: Chemical structure of cholesterol (left), and ternary phase diagram of DOPC (di-18:1-PC), DPPC (di-16:0-PC), and cholesterol (right, copied from Fig. 4 in Ref. 19 with permission). The colored region in the ternary phase diagram denotes the composition-space over which GUVs demix into coexisting liquid phases; the color at a given point corresponds to the highest temperature at which a GUV of that composition demixes, T_{mix}. Colors between symbols are interpolated.

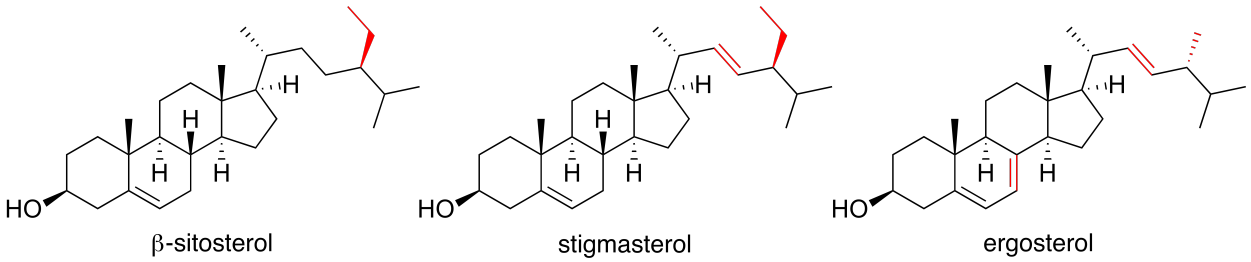

Figure 5.3: Chemical structures of β-sitosterol, stigmasterol, and ergosterol with differences from cholesterol drawn in red (see Fig. 5.2). The solubility limit of these sterols in PC-lipid bilayers is much lower than that of cholesterol: 65-70 mol% for cholesterol, ∼40 mol% for β-sitosterol, 20-25 mol% for stigmasterol, and ∼35 mol% for ergosterol.[16,17] These stark differences in solubility limits highlight the complexity of phospholipid-sterol interactions in lipid bilayers.

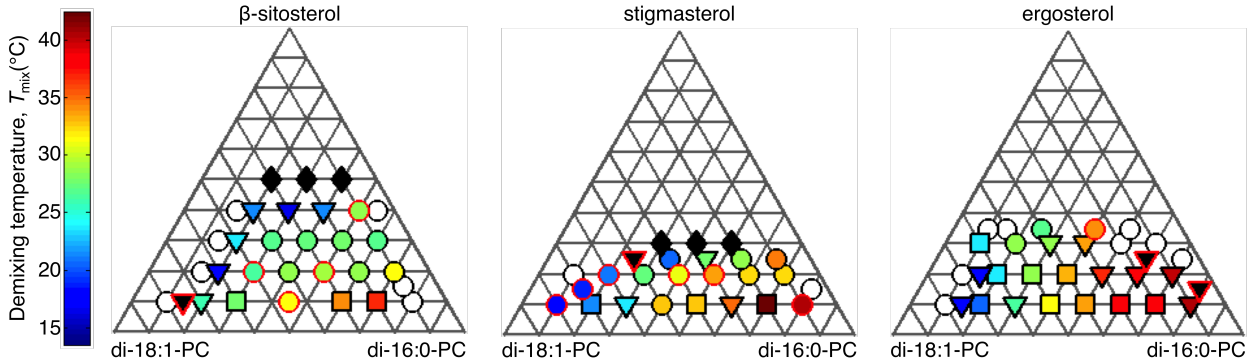

Figure 5.4: Ternary phase diagrams of mixtures of di-18:1-PC, di-16:0-PC, and either β-sitosterol, stigmasterol, or ergosterol. The interior color of a colored symbol corresponds to the temperature, T_{mix}, at which a uniform GUV of the given composition demixes into two or three coexisting phases upon cooling. Non-white circles represent liquid-liquid phase separation. Squares represent gel-liquid or gel-liquid-liquid phase separation. Triangles represent systems that phase separate but must be re-imaged before the type of phase separation can be assigned. White circles represent systems that do not phase separation at temperatures above 10 °C. Black diamonds represent systems in which pure sterol crystals were detected by darkfield microscopy. These compositions lie above the solubility limit of the sterol. Colored symbols with black outlines have a corresponding image in Fig. 5.5, whereas those with red outlines do not.

primarily due to a difference in order between the different phospholipid types[112] and if the ethyl group on the phytosterols disfavors tight packing of lipids in the liquid-ordered phase, then T_{mix} would occur at lower temperatures.

From the current state of Fig. 5.4, it is more difficult to tell how wide the range of liquid-liquid coexistence is for GUVs containing ergosterol. Gel-liquid coexistence occurs for GUVs with higher mole fractions of ergosterol than it does for GUVs containing cholesterol. It is possible that the extra degree of unsaturation in the ring structure of ergosterol causes it to be more planar than cholesterol and induces greater order in the bilayer.

The results in Figs. 5.4 and 5.5 do not shed light on the stark difference in solubility limit between cholesterol and its structural analogues in PC-lipid bilayers. It is possible that the solubility limit of sterols in bilayers is governed by sterol-sterol interactions and not PC-lipid-sterol interactions. The stability of proposed cholesterol bilayer domains[73–76] coupled with the instability of bilayer domains composed of other sterol types[113] may explain the high solubility limit of cholesterol in PC-lipid bilayers.

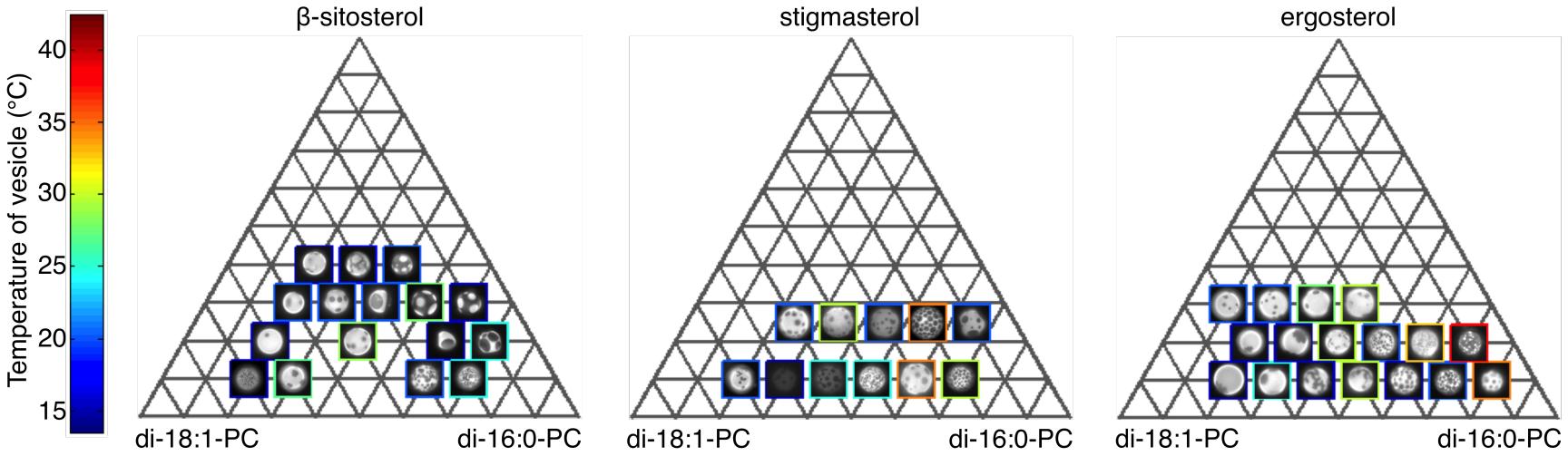

Figure 5.5: Images of giant unilamellar vesicles composed of ternary mixtures of di-18:1-PC, di-16:0-PC, and either β-sitosterol, stigmasterol, or ergosterol at a range of temperatures and compositions. The color outlining each image corresponds to the temperature at which the micrograph was taken. Each image corresponds to a point on the ternary phase diagrams shown in Fig. 5.4.

Chapter 6

THICKNESS MISMATCH OF COEXISTING LIQUID PHASES IN NON-CANONICAL LIPID BILAYERS

My contribution to this work: I developed the technique used to intentionally photo-oxidize GUVs presented in the manuscript. I also made major contributions in writing and editing the manuscript.

6.1 Abstract

Lipid composition dictates membrane thickness, which in turn can influence membrane protein activity. Lipid composition also determines whether a membrane demixes into coexisting liquid-crystalline phases. Previous measurements of demixed lipid membranes have always found a liquid-ordered phase that is thicker than the liquid-disordered phase. Here we investigated non-canonical ternary lipid mixtures designed to produce bilayers with thicker disordered phases than ordered phases. The membranes were comprised of short, saturated (ordered) lipids; long, unsaturated (disordered) lipids; and cholesterol. We found that few of these systems yield coexisting liquid phases above 10°C. For membranes that do demix into two liquid phases, we measured the thickness mismatch between the phases by atomic force microscopy and found that not one of the systems yields thicker disordered than ordered phases under standard experimental conditions. We found no monotonic relationship between the demixing temperature of these ternary systems and the physical parameters single-component membranes comprised of the individual lipids. These results highlight the surprising robustness of a membrane's liquid-ordered phase to be thicker than the liquid-disordered phase, regardless of the membrane's lipid composition.

6.2 Introduction

The activity of membrane proteins can vary dramatically with local lipid composition.[114,115] Because lipid composition dictates many physical properties of a membrane, including thickness, lateral pressure, order, and elasticity,[116] isolation of the relationship between an individual physical parameter and protein activity is difficult. This difficulty is exacerbated when the protein explores different regions of the membrane with distinct compositions. Here we study the relationship between composition and membrane thickness in model membranes with micron-scale heterogeneities. Nanoscopic heterogeneities in cell membrane thickness have been proposed to be a key parameter in membrane trafficking.[117,118]

For a single-component lipid bilayer, membrane thickness is positively correlated with both the NMR order parameter of its acyl tail and the temperature at which the lipid melts from a gel phase to a liquid crystalline phase (T_{melt}).[119,120] All three of these parameters

increase when the length or degree of saturation of the lipid tails is increased.[119,120] However, when there is a simultaneous increase in lipid tail length and decrease in lipid tail saturation, the correlation between membrane thickness, lipid order, and T_{melt} breaks down. Namely, single-component membranes comprised of monounsaturated phosphatidylcholine (PC)-lipids are thicker than membranes composed of saturated PC-lipids containing two fewer carbons per tail, despite the fact that the monounsaturated lipids are less ordered and have a lower T_{melt} than the saturated lipids.[30,95,119,121]

Some ternary membranes comprised of a high-T_{melt} lipid, a low-T_{melt} lipid, and cholesterol (chol) demix below a threshold temperature (T_{mix}) into micron-scale regions of coexisting liquid phases.[18] The resulting phases are termed the liquid-ordered (Lo) and liquid-disordered (Ld) phases in reference to the lipid tail order within each phase.[122] A schematic of our experimental setup is given in Figure 6.1. The giant unilamellar vesicles (GUVs) contain a fluorescently labeled lipid that partitions into the Ld phase, making it brighter than the Lo phase.[111,123,124] To measure the thickness differences of the Lo and Ld phases, we deposited phase separated vesicles on mica (Figure 6.1, a3). The vesicles ruptured to form isolated supported lipid bilayers (Figure 6.1, a4). We scanned the supported bilayers with atomic force microscopy to measure thickness differences. Our procedure is described fully in the Materials and Methods section.

An example of a GUV before and after rupture is shown in Figure 6.1b. The center image is a fluorescence micrograph of a phase-separated vesicle comprised of 18:1-PC/16:0-PC/cholesterol/Texas Red DHPE (40/40/20/0.8 mol/mol) at room temperature resting on a mica substrate. The Lo phase is difficult to distinguish from the background, so a schematic of the vesicle is provided to the left. The image on the right shows the isolated supported lipid bilayer formed after the vesicle ruptures. Canonically, the Lo phase, which is enriched in saturated low-T_{melt} lipids, is thicker than the Ld phase.[125]

Here we examine a series of non-canonical ternary systems composed of short-tailed ordered lipids and long-tailed disordered lipids. In particular, we study systems in which a single-component membrane comprised of the disordered lipid is thicker than a single-component membrane comprised of the ordered lipid. The lipids used in the ternary systems we investigate are listed in Table 6.1, along with previously reported thickness differences

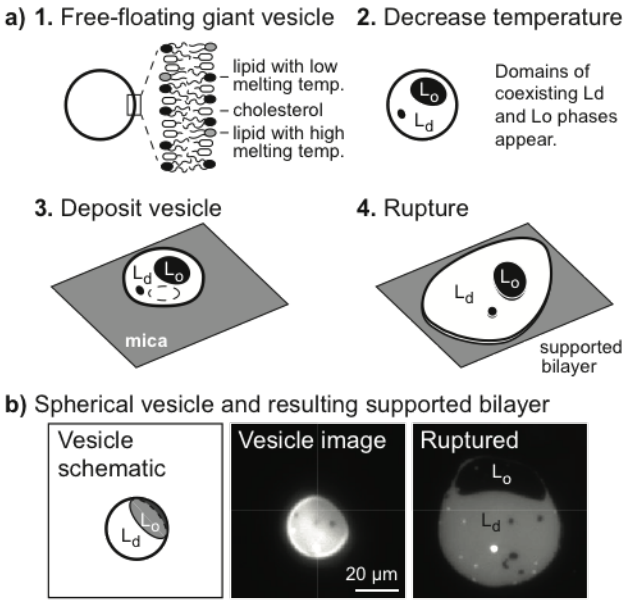

Figure 6.1: (a) Schematic of procedure to rupture phase separated giant unilamellar vesicles (GUVs) to form isolated supported lipid bilayers. (b) A phase-separated vesicle rests on a mica substrate, shown schematically in the left panel and in a fluorescence image in the center panel. The right panel shows the supported lipid bilayer that formed from the ruptured vesicle. The bilayer is comprised of 40/40/20 mol% 18:1-PC/16:0-PC/cholesterol and 0.8 mol% Texas Red DHPE.

between the corresponding single-component membranes.[30,95] Because the Ld phase is enriched in low-T_{melt} lipids, we hypothesized that these systems would produce membranes with thicker Ld than Lo phases.

Our motivation to study noncanonical membranes derives from recent literature in both physical chemistry and biophysics. Within the limited set of previous reports on thickness mismatch between Lo and Ld phases, there are no direct observations of a thicker Ld phase.[21,126–137] By producing membranes from unusual lipid mixtures that complement the canonical mixtures used in previous reports, we seek to provide a broader set of model systems for future studies on thickness-modulated protein activity and to constrain computational models that incorporate thickness mismatches between the Lo and Ld phases.[138–140] In addition, we seek to understand previously reported indirect results consistent with a thicker Ld phase. In that work, the authors interpreted changes in fluorescence signals as evidence that mutants of perfringolysin O of different lengths partition into different liquid phases of a model membrane.[141] The membrane used was a quaternary mixture that does not produce micron-scale liquid domains.

We narrowed our systems to those that are readily replicable, free of gel phase, and amenable to study by both fluorescence microscopy and room-temperature AFM. These constraints translate into four specific criteria. (1) To maximize reproducibility, we used lipids with at most one degree of unsaturation in each acyl chain, thereby minimizing the potential for photo-oxidation.[142–144] (2) To visualize the Lo and Ld phases by fluorescence microscopy, we chose membranes that demix into domains that are > 1 μm (larger than the diffraction limit of visible light). (3) To assess membrane thickness via room-temperature AFM, we examined vesicles that demix above room temperature. (4) To avoid preferential interactions between the AFM tip and different lipid headgroups, we used only lipids with the same headgroup (PC) and the same linkages (glycerol-ester).

We determined if each system is capable of liquid-liquid phase separation by fluorescence microscopy. For those that demix into coexisting liquid phases above room temperature, we measured the thickness difference between the two phases by atomic force microscopy (AFM). Our results below show the robustness of the correlation between lipid tail order, T_{melt}, and membrane thickness in systems containing coexisting liquid phases.

low-T_{melt}	high-T_{melt}	$d_{\text{high}} - d_{\text{low}}$ (Å)[a]	Lo/Ld coexist at $\geq$25 °C[b]	Fig.[c]
4Me-16:0-PC	13:0-PC	-0.7[d]	Yes	6.2a
20:1-PC	16:0-PC	-3.5	Yes	6.2a
22:1-PC	16:0-PC	-7.4	Yes[e]	6.2a
4Me-16:0-PC	12:0-PC	-2.8	No	6.2b
20:1-PC	14:0-PC	-5.8	No	6.2b
22:1-PC	17:0-PC	-5.8[d]	No	6.2c
24:1-PC	16:0-PC	-13.2	No	6.2c
24:1-PC	18:0-PC	-10.0	No	6.2c

[a]Difference in membrane thickness between single component membranes comprised of the high-T_{melt} (d_{high}) and low-T_{melt} (d_{low}) lipids.[30,95] [b]Whether or not the ternary system (with cholesterol) exhibits coexisting liquid phases above 25°C. [c]Location of phase diagrams in Figure 6.2. [d]Data estimated as an average of thicknesses of membranes comprised of lipids with tails containing one more and one fewer carbon. [e]Requires exposure to light to undergo phase separation into Lo and Ld phases.

Table 6.1: Thickness difference of single-component lipid membranes; Phase behavior of ternary lipid membranes

6.3 Results

We produced three-component GUVs by mixing cholesterol with the pairs of lipids listed in each row of Table 6.1. Structures of all lipids appear in the Supporting Information (Fig. S2). We used fluorescence microscopy to determine whether the resulting vesicles exhibited liquid-liquid phase separation in the temperature range of 10-50°C. We plot our results on Gibbs phase triangles (Figure 6.2). Of these eight systems, only two demix into coexisting liquid phases above 25°C (Figure 6.2a), and two others exhibit coexisting liquid phases below 25°C (Figure 6.2b).

As expected, we find that the dye-labeled lipid (Texas Red DHPE) preferentially partitions to the Ld phase of the model membranes in Figure 6.2a and b. Specifically, we observe larger area fractions of brightly-labeled membrane within vesicles made from lipid ratios with significant fractions of low-T_{melt} lipids (namely that fall to the left side of the two-phase coexistence regions in Figure 6.2a and b). This result is consistent with observations of the same dye preferentially partitioning to the Ld phase in other lipid systems.[19,123]

Three systems (Figure 6.2c) do not separate into coexisting liquid phases, but instead exhibit gel-liquid coexistence. It is necessary to probe only a few compositions in order to determine that no liquid-liquid phase coexistence occurs in these systems because any such coexistence would appear at the upper boundary of the gel-liquid region.[111,145–150] The system consisting of 22:1-PC/16:0-PC/cholesterol (Figure 6.2d) also does not exhibit liquid-liquid coexistence except in the case of intentional photo-oxidation, which is explicitly avoided elsewhere in our experiments. Photo-oxidation, which typically raises T_{mix},[142,144] produces coexisting liquid phases at the composition marked with the colored circle (Figure 6.2d).

In Figure 6.3, we quantify the relationship between the demixing temperature of the ternary systems and the physical properties of single-component bilayers comprised of the high-T_{melt} lipid and those comprised of the low-T_{melt} lipid. Specifically, we graph the highest system T_{mix} versus the difference in the number of carbons in the two PC-lipid tails (Figure 6.3a), the highest lipid T_{melt} (Figure 6.3b), the difference in thicknesses of the single-component membranes (Figure 6.3c), and the difference in T_{melt} of the single-component membranes (Figure 6.3d). We find that there is no monotonic relationship between the

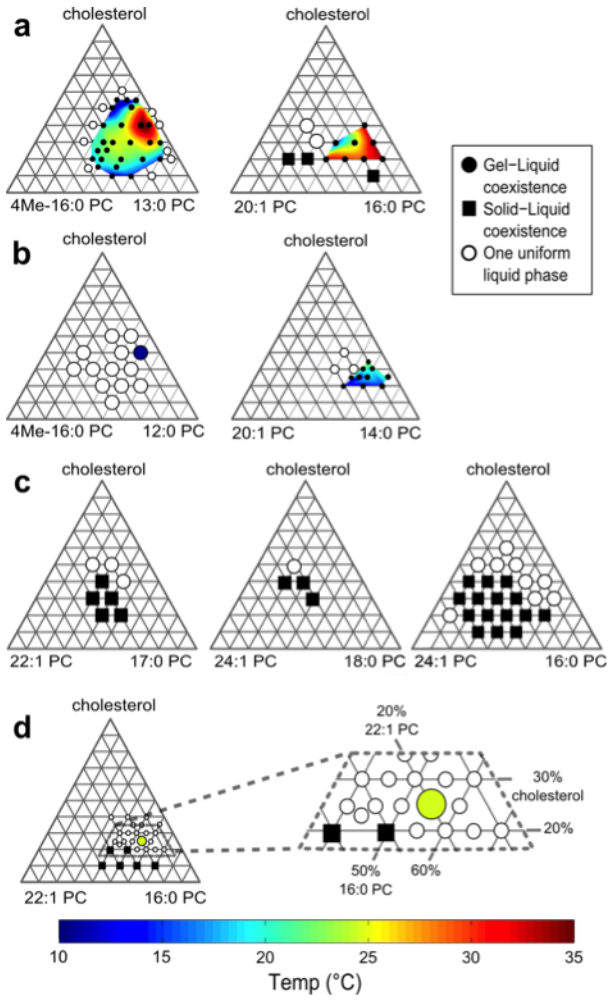

Figure 6.2: Miscibility phase diagrams of giant unilamellar vesicles (GUVs) as determined by fluorescence microscopy. Points within each triangle in the figure denote ratios of the three components. The colored regions in Figure 6.2a,b denote the liquid-liquid coexistence regions and the corresponding T_{mix}. The single colored circles in the leftmost panels of rows b and d give the single ratio of lipids that separate into coexisting liquid phases between 10-50°C in those systems. Rows differentiate membranes with ternary compositions that (a) exhibit coexisting liquid phases at or above 25°C, (b) exhibit coexisting liquid phases only below 25°C, (c) do not exhibit coexisting liquid phases, (d) exhibit coexisting liquid phases only after exposure to light. The two systems in row a and the system in row b were also investigated with room-temperature AFM.

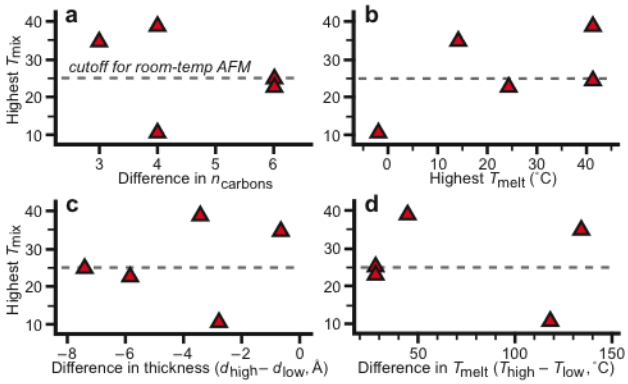

Figure 6.3: Data demonstrating a lack of correlation between the highest T_{mix} of five different ternary membranes and the physical parameters of single-component membranes of the constituent PC-lipids. The five ternary systems are given in Fig. 6.2a, 6.2b, and 6.2d. Plotted are the highest liquid-liquid demixing temperature (T_{mix}) of the ternary systems versus (a) the difference in the number of carbons in the two PC-lipid tails, (b) the highest single-component lipid gel-to-liquid melting temperature (T_{melt}), (c) the difference in thicknesses of the single-component membranes ($d_{\mathrm{high}} - d_{\mathrm{low}}$), or (d) the difference in T_{melt} of the single-component membranes ($T_{\mathrm{high}} - T_{\mathrm{low}}$). Numerical values are compiled in Table S1.

highest T_{mix} of the ternary system and any of these single-component system parameters. This lack of a clear correlation demonstrates the difficulty of predicting T_{mix} of ternary mixtures from the physical properties of the component lipids alone.

We also determined the thickness mismatch between the ordered and disordered phases in membranes exhibiting liquid-liquid phase coexistence above 25°C (Table 6.2). For the two systems in Figure 6.2a, we identified the thicknesses of the Lo and Ld phases by comparing the Lo:Ld area ratios in fluorescence microscopy to the thick:thin area ratios in AFM for a population of vesicles. In these cases, we examined two different molar ratios per system: one rich in the Lo phase and the other rich in the Ld phase, for a total of four molar ratios.

To verify that the rupturing process does not change phase behavior, we measured the Lo:Ld area ratios of free floating GUVs and the resulting supported lipid bilayers. We found no significant change in area ratio. Values appear in the Materials and Methods section.

Next we scanned the topography of individual supported lipid bilayers by AFM and measured the thick:thin area ratio and the thickness difference between the two phases. We determined that all four molar ratios described above produce membranes with thicker Lo phases than Ld phases. Figure 6.4 shows fluorescence micrographs and AFM scans of

Table 6.2: Lo:Ld and Thick:Thin membrane area ratios, with measured thickness mismatches.

Ternary membrane[a] (mol %)	Lo:Ld area GUVs[b]	Lo:Ld area SLBs[c]	Thick:Thin area AFM[d]	Thickness Mismatch (Lo-Ld,)[e]
20:1-PC/16:0-PC/chol (20/60/20)	67:33 ± 2 (N = 23)[f]	78:22 ± 3 (N = 8)	73:27 ± 2 (N = 3)	9.6 ± 0.1 (N = 3)
20:1-PC/16:0-PC/chol (50/30/20)	24:76 ± 2 (N = 25)	25:75 ± 3 (N = 7)	32:68 ± 9 (N = 4)	8.3 ± 0.1 (N = 4)
4Me-16:0-PC/13:0-PC/chol (30/40/30)	43:57 ± 2 (N = 23)	43:57 ± 1 (N = 10)	40:60 ± 8 (N = 3)	3.3 ± 1.2 (N = 3)
4Me-16:0-PC/13:0-PC/chol (20/40/40)	64:36 ± 3 (N = 13)	69:31 ± 1 (N = 46)	75:25 ± 7 (N = 4)	5.9 ± 1.0 (N = 4)
22:1-PC/16:0-PC/chol (20/55/25)	–	direct identification	–	-4.4 (N = 1)

[a]All systems contain 0.8 mol% Texas Red DHPE. [b]Ratio of Lo:Ld domain areas comprising free floating giant unilamellar vesicles (GUVs) determined by fluorescence microscopy. [c]Ratio of Lo:Ld domain areas comprising supported lipid bilayers (SLBs) made from ruptured GUVs as determined by fluorescence microscopy. [d]Ratio of SLB thick:thin domain areas determined by AFM. [e]Thickness mismatch of Lo and Ld phases determined by AFM with standard error of the mean. [f]Number of vesicles measured.

bilayers comprised of 20/40/40 mol% 4Me-16:0-PC/13:0-PC/cholesterol. AFM data and height values are compiled in Tables S2-S6.

We found that GUVs comprised of 20/55/25 mol% 22:1-PC/16:0-PC/cholesterol phase separated only upon exposure to light. To enable intense light exposure to bilayers within the AFM apparatus, we moved from the original AFM setup to an AFM coupled to a fluorescence light source. The coupled fluorescence microscope-AFM had the added advantage of allowing us to directly compare the Lo and Ld phases in fluorescence microscopy with the thicker and thinner phases in AFM (Figure 6.4d,e). We found that the Ld phase was thicker than the Lo phase in this photo-oxidized system (Table 6.2).

6.4 Discussion

Our finding that ternary membranes comprised of long-chain low-T_{melt} lipids, short chain high-T_{melt} lipids, and cholesterol produce thicker Lo than Ld phases under standard experimental conditions is surprising. Given that low-T_{melt} lipids partition preferentially into the Ld phase (and high-T_{melt} lipids into the Lo phase) and that single-component membranes made of the low-T_{melt} lipid are thicker than those made of the high-T_{melt} lipid, we expected to find some cases of thicker Ld than Lo phases. We find none (Table 6.2), except when vesicles are intentionally photo-oxidized.

The reasons that thickness differences between Lo and Ld phases in ternary systems do not simply reflect thickness differences of single-component membranes arise from the fact that the Lo and Ld phases contain mixtures of the low-T_{melt} lipid, the high-T_{melt} lipid, and cholesterol.[111] Cholesterol thickens membranes. As the cholesterol fraction in a membrane increases, the Lo phase becomes thicker than the Ld phase for two reasons. First, in PC-lipid membranes, the Lo phase contains marginally higher fractions of cholesterol than the Ld phase does.[111,145–148] Second, the Lo phase contains higher fractions of saturated lipids, and cholesterol preferentially thickens the hydrophobic regions of single-component membranes comprised of saturated lipids more than it thickens those comprised of unsaturated lipids.[29,82] Cholesterol likely increases the thickness of the lipid headgroup regions within membranes as well,[151] perhaps differentially.

In theory, preferential thickening of the Lo phase by cholesterol could be overcome by

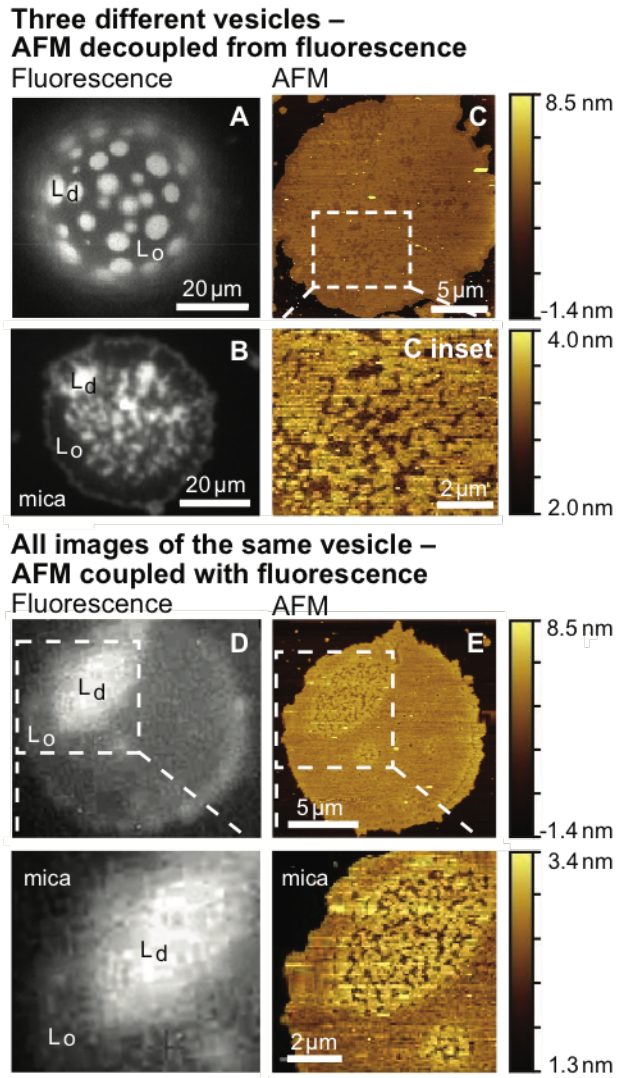

Figure 6.4: Room temperature fluorescence microscopy (left) and AFM topography (right) of membranes composed of 20/40/40 mol% 4Me-16:0-PC/13:0-PC/chol (top) and 20/55/25 mol% 22:0-PC/16:0-PC/chol (bottom). All membranes contain 0.8 mol% Texas Red DHPE. (A) Fluorescence microscopy image of a giant unilamellar vesicle (GUV) and (B) an isolated supported lipid bilayer formed by rupturing a GUV onto mica. (C) AFM topography of a different supported lipid bilayer made from the same lipid composition. (D) Fluorescence microscopy image of a supported lipid bilayer. (E) AFM topography of the same region.

introducing shorter high-T_{melt} lipids or longer low-T_{melt} lipids into bilayers. However, we find that this drives the liquid-liquid coexistence region to temperatures below 25 °C (Figure 6.2b) or eliminates it altogether (Figure 6.2c). For systems that exhibit liquid-liquid phase separation, there is no monotonic relationship between the highest T_{mix} and any of several physical parameters of the lipid components, such as the difference in thicknesses or T_{melt} values of single-component bilayers (Figure 6.3). This lack of a clear correlation implies that the properties of lipid mixtures depend on nuances of membrane structure that are not captured by the properties of single-component bilayers.

Taken broadly, our work shows that it is challenging to translate physical data for single-component membranes into quantitative predictions of the highest temperature at which Lo and Ld phases appear in ternary membranes. This task is more tractable in the case that only one of the three components of the ternary membrane is varied. For example, in membranes in which a saturated lipid is mixed with 4Me-16:0-PC and cholesterol, the highest T_{mix} increases monotonically as the chain length of the saturated lipid increases. In this system, the highest T_{mix} reaches 11, 35, and 47 ± 1°C for saturated lipids of 12:0-PC, 13:0-PC, and 16:0-PC,[145] respectively. This trend is reversed in membranes in which an unsaturated lipid is mixed with 16:0-PC and cholesterol. In this case, the highest T_{mix} increases monotonically as the chain length of the unsaturated lipid decreases such that the highest T_{mix} = 25, 39, and 40 ± 1°C for unsaturated lipids of 22:1-PC, 20:1-PC, and 18:1-PC,[19] respectively. The reversal of the trend illustrates why predicting the highest T_{mix} for an arbitrary ternary membrane is difficult.

To date, quantitative measurements of the thickness difference between coexisting Lo and Ld phases have been reported for only a few systems.[21,126–137] Those published data, combined with our thickness difference measurements in Table S7 provide evidence about the alignment of bilayers on solid supports. In a supported bilayer, if all phospholipid headgroups that face the substrate lie in the same plane, then any thickness mismatch is accommodated entirely in the monolayer furthest from the surface. Evidence in support of this scenario is found in some reported thickness differences between Lo and Ld phases in 40/40/20 18:1-PC/16:0-PC/cholesterol supported lipid bilayers. Measurements by AFM, which are sensitive to the difference in height between the top leaflets of each phase, give

values of 1.2 ± 0.1 (from our data in Table S7), 1.2 ± 0.2, and 0.65 ± 0.02 nm.[129,152] Our value agrees well with the results from reference.[129] All of these AFM values are larger than the thickness difference for the same system of 0.56 ± 0.2 nm measured by X-ray diffraction, which is sensitive to the phosphate-to-phosphate distance.[130] On the other hand, Nielsen and Simonsen make the opposite argument[136] based on their reported thickness difference measured by ellipsometry, which, like X-ray diffraction, is sensitive to the total thickness difference. Their value of 1.69 nm is significantly larger than step heights reported by AFM, from which they conclude that thickness differences in supported bilayers are distributed on both faces of the membrane.

Our results, along with the data in Tables S2 through S6 in the Supporting Information, provide a broad context within which to assess supported membranes and AFM measurements of membrane thickness. AFM is noted for its sub-Ångstrom-level height resolution, yet sample-to-sample variation in measured membrane thickness is at least one order of magnitude greater than this resolution. Moreover, different scanning methods yield different values. Previous authors have advocated the use of low-force, contact-mode methods, citing that tapping mode methods yield wide variation and/or drifts in thickness measurements.[135] Consideration of whether the AFM tip penetrates the membrane and of whether compressibilities of the two membrane phases differ significantly may also be important in some systems.[135,153–155] Spurious height differences between phases can result from known AFM artifacts such as edge overshoot, which results from hysteresis in the z-piezoelectric ceramic, and from overly limited data as in a single line profile.[156] The AFM field has yet to converge upon a single, best method that yields a measurement of membrane thickness or of thickness mismatch that is consistently repeatable between different research groups, and details such as scanning forces are not always reported. This situation underscores the utility of interrogating the same membrane region by multiple techniques, such as fluorescence microscopy and AFM. Complementary methods of assessing membrane thicknesses include X-ray and neutron diffraction,[30,82,95,130,157] cryo-electron microscopy,[158] and imaging ellipsometry.[136] A strong advantage of the experimental design of our AFM study is that it focuses on the sign of the thickness mismatch rather than the magnitude, such that the sign should be replicable by other AFM methods.

Table 6.2 reports a direct measurement of a thicker Ld phase, with the major caveat that the phenomenon occurs for a single lipid ratio and requires photo-oxidation, which perturbs the membrane composition. A less important caveat is that the origin and significance of the small-scale structure in Figure 6.4e is unclear; it may not exist in a corresponding membrane of a free-floating vesicle. For instance, submicron inhomogeneity may arise due to an offset between the temperature of the AFM and the temperature at which vesicles are ruptured, or due to a shift in miscibility transition temperature between a vesicle and a supported bilayer. Indeed, shifts in T_{mix} can result from membrane adhesion to surfaces.[159–162] As a result of such temperature shifts, the membrane may approach a critical point,[143,146,163] or new solid or liquid domains may nucleate but be hydrodynamically hindered from coarsening.[164–166] Temperature shifts that result in three-phase (Lo-Ld-gel) membranes provide a particularly compelling explanation of the appearance of noncircular, small domains in supported membranes made from ruptured GUVs.[146,167]

More generally, our report of a thicker Ld than Lo phase in a photo-oxidized membrane is important because it suggests that future searches for thicker Ld phases in unoxidized membranes will eventually yield positive results. Review of the data amassed in Table 6.1 and Figure 6.3 suggests tactics to be employed in those future searches. A lack of temperature control in our AFM setup required room-temperature phase separation in membranes. Methods that assess membrane thickness below room temperature could be applied to 20:1-PC/14:0-PC/cholesterol, which is a promising system both because of the large difference in lipid tail lengths and because of implications by Lin and London that a similar system (20:1-PC/16:0-PC/14:0-PC/cholesterol) features thicker Ld than Lo phases.[141] Another tactic would be to employ chemical synthesis to produce low-T_{melt} lipids with longer methylated chains than 4Me-16:0-PC. Any tactic that involves replacing the low-T_{melt} lipid with a polyunsaturated lipid (e.g. 22:6-PC) should be undertaken with caution because acyl chains of polyunsaturated lipids are readily photo-oxidized and because those chains are more likely than chains of singly unsaturated lipids to fold back on themselves such that their methyl carbons lie near lipid head groups, negating the expected thickening from adding carbons to the tail.[168]

6.5 Conclusion

We combined fluorescence microscopy and room temperature AFM to measure transition temperatures and the Lo-Ld thickness mismatch in model membranes. We used non-canonical ternary lipid mixtures for which the one-component membrane of the low-T_{melt} lipid is thicker than a one-component membrane of the high-T_{melt} lipid. We found that not one of the systems in Table 6.2 produced thicker Ld than Lo phases under standard experimental conditions (i.e. without photo-oxidation of the membrane). Moreover, we found no simple monotonic relationship between the highest possible miscibility transition temperature in these ternary membranes and the relative properties of single-component membranes comprised of the low-T_{melt} and high-T_{melt} lipids. It is a common[169,170] and even textbook assertion[171,172] that rafts within cell membranes contain lipids with more ordered acyl chains and are thicker than the surrounding cell membrane. Even when we employed the lipid mixtures in Table 6.1, we found no physical reason to challenge this assertion. Future direct searches for thicker Ld regions may find it productive to employ low-temperature methods or to incorporate lipids with longer methylated chains in the membranes.

6.6 Materials and Methods

6.6.1 Lipids

All phosphocholine (PC) lipids (Avanti Polar Lipids, Alabaster, AL), Texas Red dihexadecanoyl-PE (DHPE; Life Technologies, Grand Island, NY), and cholesterol (chol; Sigma, St. Louis, MO) were purchased and used without further purification. The PC-lipids and their single-component membrane Tmelt values are as follows: dilauroyl-PC (12:0-PC, -2°C), ditridecanoyl-PC (13:0-PC, 14°C), dimyristoyl-PC (14:0-PC, 24°C), dipalmitoyl-PC (16:0-PC, 41°C), diheptadecanoyl-PC (17:0-PC, 50°C), distearoyl-PC (18:0-PC, 55°C), dioleoyl-PC (18:1-PC, -17°C), dieicosenoyl-PC (20:1-PC, -4°C), dierucoyl-PC (22:1-PC, 13°C), dinervonoyl-PC (24:1-PC, 27°C), and diphytanoyl-PC (4Me-16:0-PC, <-120°C).[85,173,174] Structures of the lipids are given in Figure S1.

6.6.2 Giant Unilamellar Vesicles

To avoid the problem that sonicated vesicles, which are commonly used in AFM studies to produce supported lipid bilayers, do not always contain the same lipid and sterol composition as the large vesicles from which they are made,[46] we interrogated GUVs. Miscibility phase behavior was determined by fluorescence microscopy of intact, free-floating giant unilamellar vesicles. Thicknesses of the two liquid phases were determined by AFM of supported lipid bilayers made by rupturing GUVs of the same composition.

Taut GUVs were produced by electroformation[18,175] at 60 °C for 1 hr. with the application of 1.5 V at 10 Hz. Vesicles to be assessed by AFM were made in 200 mM sucrose; the freshly-made vesicle solution was cooled to room temperature and diluted in 3 mL of 200 mM sucrose. Vesicles to be assessed by fluorescence microscopy alone were made in 18 MΩ-cm water and further diluted before viewing. Electroformation in sucrose does not significantly shift T_{mix} for vesicles containing zwitterionic lipids (as opposed to those containing lipids with a net charge).[176] Vesicles for fluorescence microscopy were labeled with 0.8 mol% Texas Red DHPE[177] and used within 4 hours of electroformation.

6.6.3 Determination of T_{mix} in GUVs

Vesicles were imaged by fluorescence microscopy and T_{mix} values were determined as described in detail previously.[19,143] Briefly, the vesicle solution was placed between two coverslips, sealed with vacuum grease, and thermally coupled to a temperature-controlled stage on a fluorescence microscope. As temperature decreased, the percentage of vesicles exhibiting micron-scale liquid-liquid phase separation was recorded, and the resulting data were fit with a sigmoidal curve to determine T_{mix}, the temperature at which 50% of vesicles phase separated. Variation in T_{mix} arises from small vesicle-to-vesicle compositional differences.[18] Gel domains were visually identified by their lack of coalescence and rigid, noncircular shapes; liquid domains are circular and coalesce.[166]

6.6.4 Rupture of GUVs into spatially separated supported lipid bilayers

The top layers of a mica disk (Highest Grade V1, Ted Pella, Redding, CA) were cleaved with Scotch tape (3M, St. Paul, MN) to reveal a clean, smooth surface. Then 500 μL of 200 mM glucose/5mM $CaCl_2$ was pipetted onto the mica, followed by 50 μL of GUV-rich sucrose solution. After 15 min., the bilayer was rinsed with 1 mL aliquots of water 20 times, taking care that the surface was never exposed to air. This process resulted in a mica surface densely covered with individual supported lipid bilayers separated by areas of bare mica (Figure 6.1b). This surface remained submerged under water for the remainder of the experiment.

6.6.5 Conservation of area fraction upon GUV rupture

In Figure 1b, the total surface area of the free-floating vesicle was the same ($2.57 \pm 0.40 \times 10^3$ μm^2) as the supported lipid bilayer that it became ($2.50 \pm 0.08 \times 10^3$ μm^2). The average area fraction of the Ld phase was the same before (75 ± 4%) and after rupture (77 ± 2%). Reported uncertainties are the standard deviations of area fractions determined using the inner and the outer edges of the vesicle, specifically the inner and outer the edges determined after Canny-Deriche filtering of the image for edge detection (setting parameter $\alpha = 1.00$ in Fiji[90]). The observation of equivalent area fractions in free-floating vesicles and supported lipid bilayers is consistent with an absence of a significant shift in miscibility tie-line endpoints upon rupture.

6.6.6 Measuring Lo:Ld area fractions

To determine Lo:Ld area ratios, free-floating, fluorescently labeled GUVs were imaged with light from a mercury arc light source (USH-102DH, Ushio, Tokyo, Japan) that was filtered through a Texas Red HYQ filter, which was housed within a Nikon YFL microscope equipped with a 40x, 0.60 N.A. objective (Nikon, Melville, NY). The GUVs were ruptured onto a mica disk to form supported lipid bilayers as described above, and the area ratio was measured again by fluorescence microscopy. Fluorescence images were captured on a Coolsnap HQ charge-coupled device camera (Photometrics, Tucson, AZ).

6.6.7 AFM decoupled from fluorescence microscopy

GUVs were ruptured onto a mica disk to form supported lipid bilayers. The disk was adhered with Vaseline (Unilever, Englewood Cliffs, NJ) to the bottom of a perfusion cell (Bruker, Santa Barbara, CA). Images were acquired on a Dimension Icon Atomic Force Microscope (Bruker, Santa Barbara, CA) in quantitative nanomechanical mapping mode using SCANASYST-AIR cantilevers (k = 0.4 N/m, Bruker). We determined the thick:thin area ratio of an individual supported lipid bilayer by imaging its entire surface. We compared the Lo:Ld area ratio to the thick:thin area ratio in order to associate the phases measured by AFM with the phases measured by fluorescence.

6.6.8 AFM coupled with fluorescence microscopy

Fluorescently labeled vesicles of 20/55/25 mol% 22:1-PC/16:0-PC/chol were introduced to a solution of 200 mM glucose/5mM $CaCl_2$ above the mica substrate and imaged on a Nikon YFL microscope with a mercury arc light source (USH-102DH, Ushio, Tokyo, Japan). The light was filtered through a Texas Red HYQ filter block (Nikon) and focused on the sample through a CFI Plan Fluor 60X objective (Nikon). GUVs were exposed to light for approximately 5 minutes. Vesicles that remained unexposed to the light source did not phase separate. Bilayers were imaged with an MFP-3D-BIO Atomic Force Microscope (Asylum Research) seated on a Nikon Eclipse Ti microscope.[178] Fluorescence images were captured on a Spot FX1520 CCD Camera (Spot Imaging Solutions, Sterling Heights, MI). Scans were performed in contact mode using DNP-10 tips (0.12 N/m, Bruker) at a constant scanning force from 0.2 - 0.4 nN, such that experiments here and by other researchers[135] were conducted under the same conditions.

6.6.9 AFM image processing

AFM images were flattened in Gwyddion as described in the Supporting Information.[179] Height histograms were exported to MATLAB (MathWorks, Natick, MA) and fit with two Gaussian peaks corresponding to the thick and thin phases using the program ipf.m[180] as described in methods in the Supporting Information. Reported membrane thicknesses are

differences between the centers of these peaks and are summarized in Tables S2-S6.

6.7 Acknowledgements

This research was supported by National Science Foundation grants MCB07444852 and MCB1402059. J.V.B. was supported by NIH Training in Molecular Biophysics T32 GM008268. P.A.C. acknowledges support from NSF DMR-1306079. P.A.C. and the laboratory of David Ginger thank AFOSR for supporting instrumentation of an AFM coupled to a fluorescence light source. J.P.L. was supported by National Science Foundation Graduate Research Fellowship DGE0718124. D.G.C. and R.N.F. were supported by NIH grant EB-002027 to the National ECSA and Surface Analysis Center for Biomedical Problems (NESAC/BIO). We thank Scott Rayermann for comments on the manuscript.

Supporting Information

Thickness mismatch of coexisting liquid phases in non-canonical lipid bilayers.

Joan V. Bleecker, Phillip A. Cox, Rami N. Foster, Jonathan P. Litz, Matthew C. Blosser, David G. Castner, and Sarah L. Keller

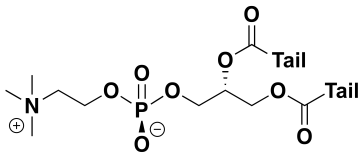

Lipid:	Tail:	single-component bilayer thickness (Å)	T_{melt} (°C)
12:0-PC		32.6, at 30 °C	-2
13:0-PC		N/A	14
14:0-PC		36.7, at 30 °C	24
16:0-PC		39.0, at 50 °C	41
17:0-PC		N/A	50
18:0-PC		42.2, at 60 °C	55
20:1-PC		42.5, at 30 °C	-4
22:1-PC		46.4, at 30 °C	13
24:1-PC		65.7, at 30 °C	27
4Me-16:0-PC		35.4, at 30 °C	< -120

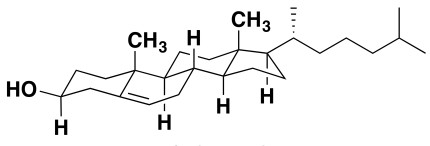

cholesterol

Figure S1: Lipid structures, including values of melting temperatures[1-3] and thicknesses of corresponding single-component bilayers.[4,5]

Table S1: Detailed origin of values in Table 1 and Figure 3 of the main text

high-T_{melt} lipid[a]	low-T_{melt} lipid[a]	T_{high}[b] (°C)	T_{low}[b] (°C)	Δn_{carbon}[c]	$T_{high} - T_{low}$[d] (°C)	$d_{high} - d_{low}$[e] (Å)	Max T_{mix}[f] (°C)
12:0 PC[g]	4Me-16:0 PC[h]	– 2	– 120	4	118	– 2.8	11
13:0 PC	4Me-16:0 PC[h]	14	– 120	3	134	– 0.7[i]	35
14:0 PC	20:1 PC	24	– 4	6	28	– 5.8	23
16:0 PC	20:1 PC	41	– 4	4	45	– 3.5	39
16:0 PC	22:1 PC	41	13	6	28	– 7.4	25[j]

[a]High and low melting temperature (T_{melt}) lipids. [b]Gel to liquid-crystalline melting temperature of single-component membranes made from the high-T_{melt} or low-T_{melt} lipid.[1-3] [c]Difference in number of carbons of the acyl chains of the high-T_{melt} and low-T_{melt} lipids. [d]Difference in gel-liquid melting temperatures of the high-T_{melt} and low-T_{melt} lipids. [e]Difference in thicknesses of single-component membranes made from the high-T_{melt} and low-T_{melt} lipid membranes.[4,5] [f]Maximum observed miscibility transition temperature for membranes containing ternary mixtures of low-T_{melt} lipid / high-T_{melt} lipid / cholesterol. [g]This notation connotes (lipid acyl chain length):(number of double bonds within each of the two lipid tails), with a PC lipid head group. [h]"4Me" denotes four methyl groups along the acyl tail. [i]Data were estimated as an average of two values, one for the lipid with one less carbon in its tail, and one for the lipid with one more carbon. [j]Vesicles require exposure to light to phase separate.

Method: AFM image processing (flattening) in Gwyddion[6,7]

AFM images produce a false color topographic map. The default gray color is set to gold (Figure S2). Mean plane subtraction is used to eliminate background tilt that obscures bilayer thicknesses (Figure S2A). Next, scan lines are corrected by matching height medians, and the image is corrected for horizontal scars. The mica and the lipid membrane, which may contain both thick and thin regions, produce at least two distinct height populations. To avoid non-physical flattening results due to these populations, we mask out each layer individually using the marks grains tool and perform a median line scan correction on each layer separately (Figure S2C). Last, we mask out of the lowest feature, which is either the mica or thin membrane, and perform a zeroth order background subtraction to set this feature to ~ 0 nm. We then use Gywddion's 1D statistical functions to obtain the height histogram. We export height histogram values to Excel, read the Excel file into Matlab and fit the data with peaks using 100 bootstrap trial method as part of the peak fitting program ipf.m.[8]

.

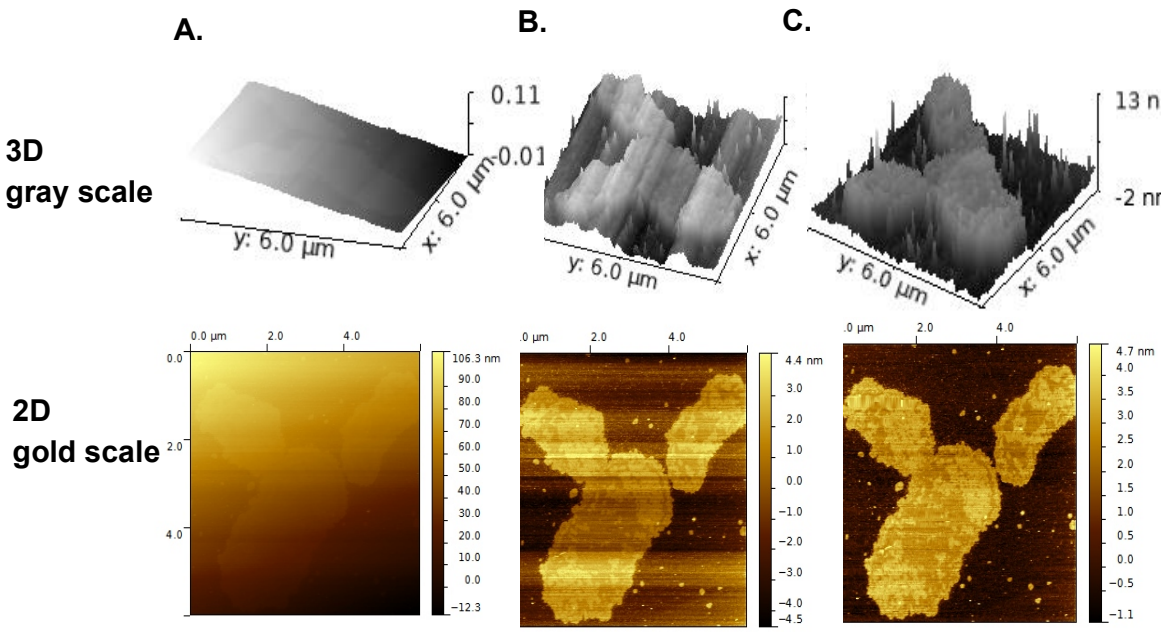

Figure S2 Processing a raw AFM image of supported bilayers of 30/40/30 mol% 4Me-16:0 PC/13:0 PC/chol on mica. AFM scans are shown axiometrically in gray (top) and 2-dimensionally in gold (bottom). (A) Image before processing. (B) Image after plane correction, median line scan correction, and horizontal scar correction. (C) Image after median line corrections of the bilayer and mica layer and after zeroing the mica layer. The height histogram of this final image is processed with Matlab peak-fitting software.

Method: Fitting AFM height histogram peaks to determine thickness mismatch

The interactive Matlab peak-fitting program ipf.m uses an unconstrained non-linear optimization algorithm to decompose separate and/or overlapping-peaks into component peaks.[8] This process gives us differences in thickness between membrane regions, standard deviations in thickness, and areas of the peaks, which allows us to calculate the percent of the membrane area covered by thin and thick phases.

The default peak shape is Gaussian, and other peak types are available. We find that changing peak type from Gaussian to other peak types, such as Lorentzian, results in larger fit uncertainties and larger standard deviations from bootstrap methods. Running ipf.m produces a scatter plot of the height histogram data within an interactive graph. The user then selects the range of x-values (heights in nm) that encompasses all peaks of interest. The program requires first guesses for the peak positions, which we accomplished by clicking on peaks because this procedure is recommended for data like ours for which peaks are not evenly spaced.

We next performed a 100 trial bootstrap fit. In each trial, the data set is divided into two sub-sets, each of which is fit, and then the process is repeated. Our reported values for thickness differences between thick and thin regions of membranes (Tables S3-S7) are the differences in the bootstrap mean value of the fitted peaks from the bootstrap fit. The reported uncertainties in the values for each image are the propagated errors from standard deviations produced by the bootstrap method. These uncertainties range from very small values (requiring three decimal places) to two unusually large values. The two examples of large uncertainties appear in Table S5 #2 and Table S6 #4, for which the bootstrap standard deviation is larger than the interquartile range, indicating that at least one trial fit is significantly different from the average fit. For those cases, the standard deviation from the interquartile range is used instead of the bootstrap standard deviation, because the interquartile range is less susceptible to outliers.

Only two images (Table S5 #1 and #3) presented cases in which the bootstrap calculation failed to produce a physically plausible, stable fit. This is unsurprising because the two bilayer peaks significantly overlap for these two images. For these two images, we surveyed the trial fits until we found a fit that made physical sense. We then pinned the peak means to the means of these fits and performed a bootstrap fit to determine the areas of the two bilayer peaks. We did not report standard deviations for these fits. Inclusion of these images does not skew our data because we would obtain similar results from the image in Table S5 #2 alone.

Table S2: Method 1 AFM images, peak fits, and resulting data for 20/60/20 mol% 20:1-PC/16:0-PC/chol supported lipid bilayer

#	AFM image[a]	(Top) Height histogram[b] (Bottom) Peak fit[c]	Difference in thickness between thin and thick membrane regions (nm)[d]	Ratio of areas of thick:thin regions[e]	Avg. thickness mismatch (nm) and ratio of areas of thick:thin regions[f]
1	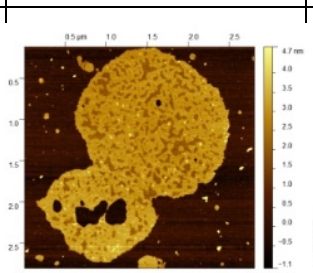	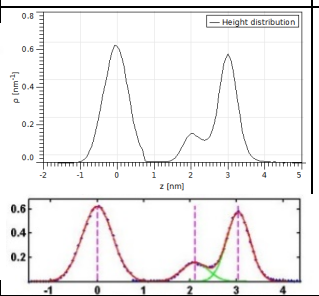	0.938 ± 0.391	77:23	0.95 ± 0.06 73:27 ± 2
2[g]	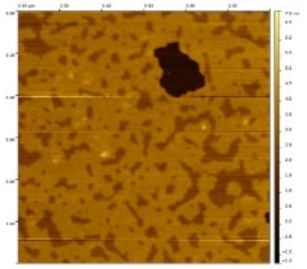	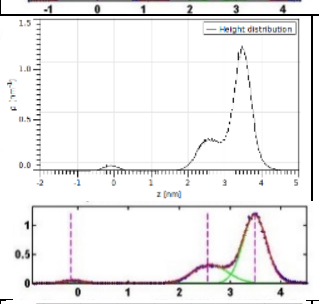	0.872 ± 0.004	72:28	
3	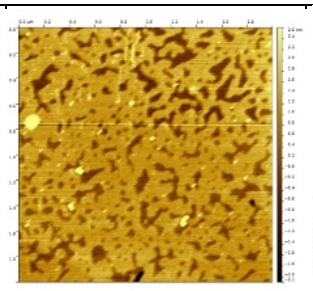	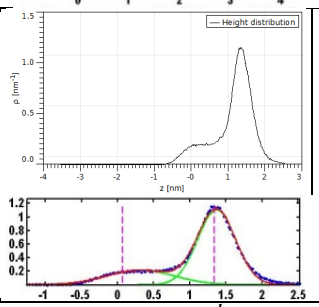	1.037 ± 0.066	74:26	

[a]Flattened AFM image with height scale bar in gold. [b]Height histogram in Gwyddion. [c]Typical peak fit trial of the height histogram in a 100-trial bootstrap fit. Blue dots fit by the dark red line is the total peak fit, light green lines are the component peaks, and magenta dashed lines show the first guess at peak position from the previous trial. [d]Difference between thickness of the thin and thick regions of the membrane reported as the mean difference in the location of the peaks determined by the bootstrap method. The reported uncertainty is the propagated standard deviation from the bootstrap fit of the two bilayer peaks. [e]Ratio of areas of thick and thin membrane regions from the bootstrap average areas of the two bilayer peaks. [f]Average thickness difference from column 4. The reported uncertainty is the standard error of the three values. [g]The image in row 2 is a higher-magnification region of the vesicle in row 1.

Table S3: Method 1 AFM images, peak fits, and resulting data for 50/30/20 mol% 20:1-PC/16:0-PC/chol supported lipid bilayer

#	AFM image[a]	(Top) height histogram[b] (Bottom) peak fit[c]	Difference in thickness between thin and thick membrane regions(nm) [d]	Ratio of areas of thick:thin regions [e]	Avg thickness mismatch (nm) and ratio of areas of thick:thin regions [f]
1	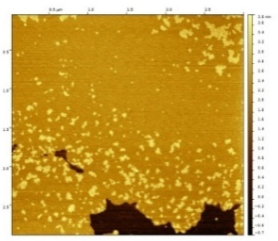	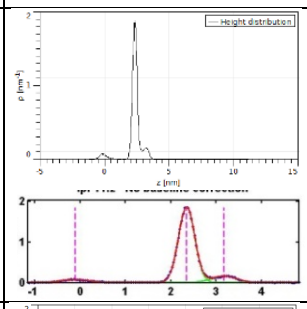	0.824 ± 0.003	12:88	0.83 ± 0.08 32:68 ± 9
2	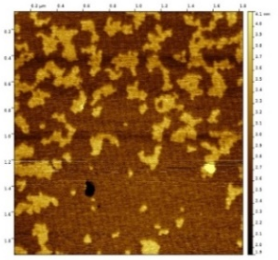	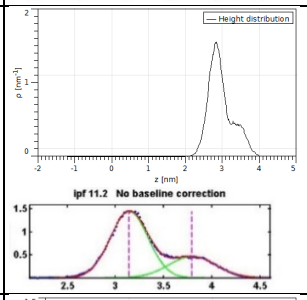	0.652 ± 0.002	29:71	
3	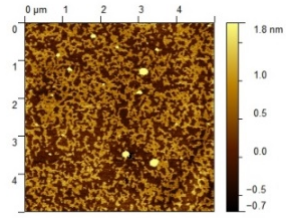	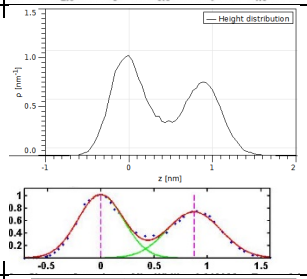	0.874 ± 0.002	46:54	
4	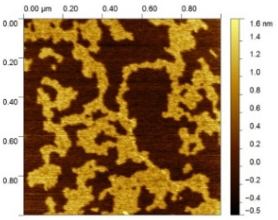	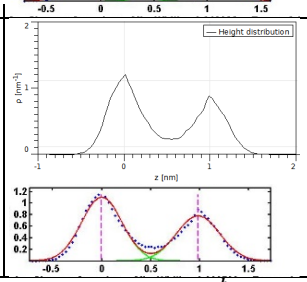	0.985 ± 0.002	43:57	

[a]Flattened AFM image with height scale bar in gold. [b]Height histogram in Gwyddion. [c]Typical peak fit trial of the height histogram in a 100-trial bootstrap fit. Blue dots fit by the dark red line is the total peak fit, light green lines are the component peaks, and magenta dashed lines show the first guess at peak position from the previous trial. [d]Difference between thickness of the thin and thick regions of the membrane reported as the mean difference in the location of the peaks determined by the bootstrap method. The reported uncertainty is the propagated standard deviation from the bootstrap fit of the two bilayer peaks. [e]Ratio of areas of thick and thin membrane regions from the bootstrap average areas of the two bilayer peaks. [f]Average thickness difference from column 4. The reported uncertainty is the standard error of the three values.

Table S4: Method 1 AFM images, peak fits, and resulting data for 30/40/30 mol% 4Me-16:0-PC/13:0-PC/chol

#	AFM image[a]	(Top) height histogram[b] (Bottom) peak fit[c]	Difference in thickness between thin and thick membrane regions(nm) [d]	Ratio of areas of thick:thin regions [e]	Avg thickness mismatch (nm) and ratio of areas of thick:thin regions [f]
1	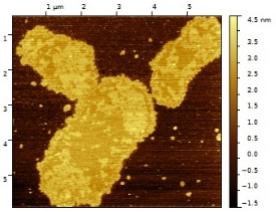	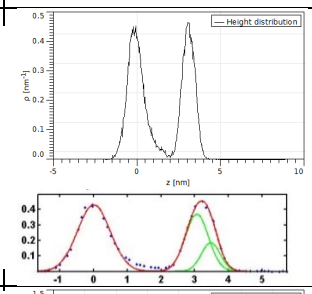	0.413[g]	29:71	0.37 ± 0.07 40:60 ± 8
2[h]	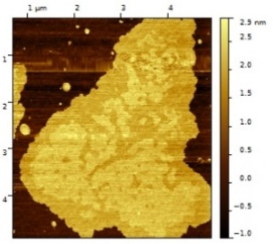	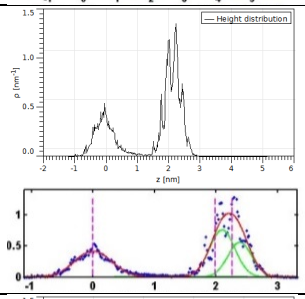	0.392 ± 0.217[i]	41:59	
3[h]	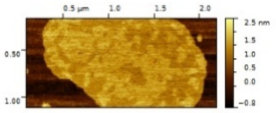	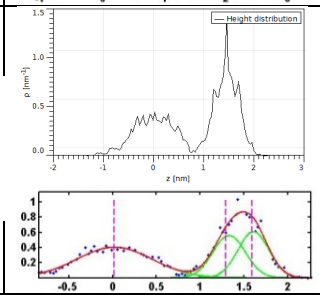	0.296[g]	51:49	

[a]Flattened AFM image with height scale bar in gold. [b]Height histogram in Gwyddion. [c]Typical peak fit trial of the height histogram in a 100-trial bootstrap fit. Blue dots fit by the dark red line is the total peak fit, light green lines are the component peaks, and magenta dashed lines show the first guess at peak position from the previous trial. [d]Difference between thickness of the thin and thick regions of the membrane reported as the mean difference in the location of the peaks determined by the bootstrap method. The reported uncertainty is the propagated standard deviation from the bootstrap fit of the two bilayer peaks. [e]Ratio of areas of thick and thin membrane regions from the bootstrap average areas of the two bilayer peaks. [f]Average thickness difference from column 4. The reported uncertainty is the standard error of the three values. [g]The bootstrap calculation failed to produce a physically-plausible, stable fit. For these two images, we surveyed the trial fits until we found a fit that made physical sense. We then pinned the peak means to the means of these fits and performed a bootstrap fit to determine the areas of the two bilayer peaks. We did not report standard deviations for these fits. [h]The experiment in row 1 was conducted on a different day than the experiments in rows 2 and 3. [i]For this system the bootstrap standard deviation is much larger than the bootstrap interquartile range (IQR), indicating that at least one trial had a significantly different fit. IQR is more robust to outliers. In this case, a better indicator of experimental uncertainty is the standard deviation given by IQR/1.34896,[8] which is the value given in the table.

Table S5: Method 1 AFM images, peak fits, and resulting data for 20/40/40 mol% 4Me-16:0-PC/13:0-PC/chol

#	AFM image[a]	(Top) height histogram[b] (Bottom) peak fit[c]	Difference in thickness between thin and thick membrane regions(nm) [d]	Ratio of areas of thick:thin regions [e]	Avg thickness mismatch (nm) and ratio of areas of thick:thin regions [f]
1[g]	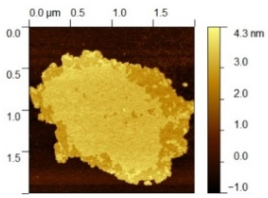	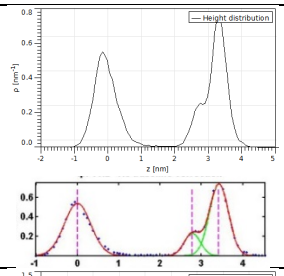	0.642 ± 0.005	79:21	0.59 ± 0.10 75:25 ± 7
2[g]	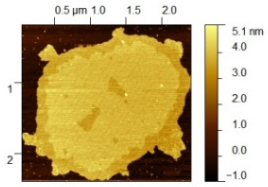	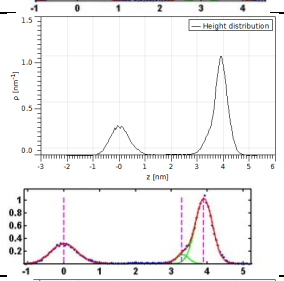	0.592 ± 0.067	90:10	
3[h]	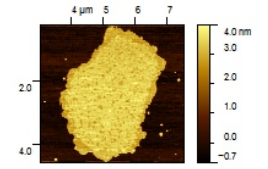	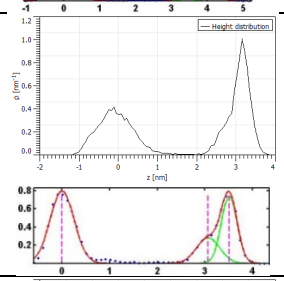	0.450 ± 0.046	66:34	
4[h]	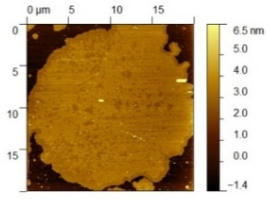	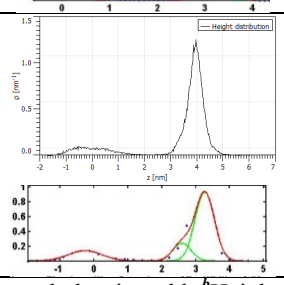	0.676 ± 0.406[i]	65:35	

[a]Flattened AFM image with height scale bar in gold. [b]Height histogram in Gwyddion. [c]Typical peak fit trial of the height histogram in a 100-trial bootstrap fit. Blue dots fit by the dark red line is the total peak fit, light green lines are the component peaks, and magenta dashed lines show the first guess at peak position from the previous trial. [d]Difference between thickness of the thin and thick regions of the membrane reported as the mean difference in the location of the peaks determined by the bootstrap method. The reported uncertainty is the propagated standard deviation from the bootstrap fit of the two bilayer peaks. [e]Ratio of areas of thick and thin membrane regions from the bootstrap average areas of the two bilayer peaks. [f]Average thickness difference from column 4. The reported uncertainty is the standard error of the three values. [g]Vesicles were made without dye. [h]Experiments #3 and #4 were conducted on a different day than #1 and #2. [i]For this system, the bootstrap standard deviation is much larger than the bootstrap interquartile range (IQR), indicating that at least one trial had a significantly different fit. IQR is more robust to outliers. In this case, a better indicator of experimental uncertainty is the standard deviation given by IQR/1.34896,[8] which is the value given in the table.

Table S6: Method 2 AFM image, peak fits, and resulting data for 55/20/25 mol% 22:1-PC/16:0-PC/chol

AFM image[a]	(Top) height histogram[b] (Bottom) peak fit[c]	Lo-Ld thickness mismatch[d] (nm) and ratio of areas of thick:thin membrane regions[e]
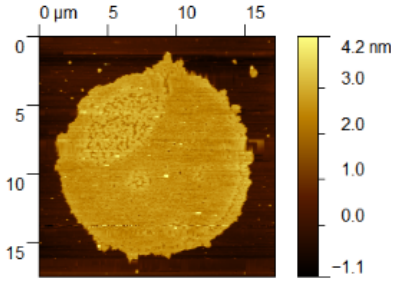	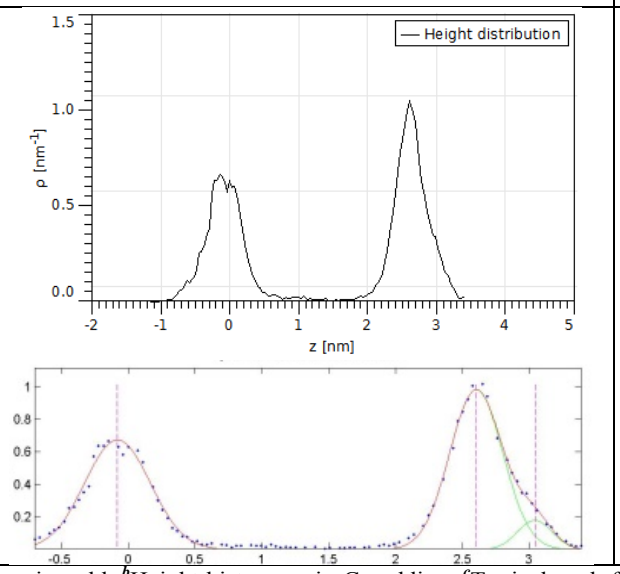	– 0.44 ± 0.01 89:11

[a]Flattened AFM image with height scale bar in gold. [b]Height histogram in Gwyddion. [c]Typical peak fit trial of the height histogram in a 100-trial bootstrap fit. Blue dots fit by the dark red line is the total peak fit, light green lines are the component peaks, and magenta dashed lines show the first guess at peak position from the previous trial. [d]Difference between thickness of the thin and thick regions of the membrane reported as the mean difference in the location of the peaks determined by the bootstrap method. The reported uncertainty is the propagated standard deviation from the bootstrap fit of the two bilayer peaks. [e]Ratio of areas of thick and thin membrane regions from the bootstrap average areas of the two bilayer peaks.

Table S7: 40/40/20 mol% 18:1-PC/16:0-PC/chol control system for AFM Method 2

T_{mix} [a] (°C)	$L_o - L_d$ [b] AFM (nm)	Average $L_o - L_d$ [c] AFM (nm)	Literature $L_d - L_o$ AFM (nm)
34 ± 1 [15]	1.240 ± 0.018 1.182 ± 0.019 0.958 ± 0.011 1.381 ± 0.004	1.19 ± 0.10	1.2 ± 0.2 [16] 0.65 ± 0.02 [17]

[a]Miscibility transition temperature of the Lo and Ld phases. [b]Thickness mismatch of Lo and Ld phases determined by a bootstrap peak fitting procedure for AFM images. Uncertainties are given as standard deviations derived from the bootstrap method. [c]Average of the four thickness mismatch values in Column 2.

REFERENCES

(1) Lindsey, H.; Petersen, N. O.; Chan, S. I. *Biochim. Biophys. Acta* **1979**, *555*, 147-67.
(2) Silvius, J. R. In *Lipid-Protein Interactions*; John Wiley & Sons: New York, 1982.
(3) Marsh, D. *CRC Handbook of Lipid Bilayers*; CRC Press: Boca Raton, FL, 1990.
(4) Kučerka, N.; Gallová, J.; Uhríková, D.; Balgavy, P.; Bulacu, M.; Marrink, S.-J.; Katsaras, J. *Biophys. J.* **2009**, *97*, 1926-32.
(5) Kučerka, N.; Nieh, M.-P.; Katsaras, J. *Biochim. Biophys. Acta* **2011**, *1808*, 2761-71.
(6) Nečas, D.; Klapetek, P. *Cent. Eur. J. Phys.* **2012**, *10*, 181-8.
(7) Eaton, P.; West, P. *Atomic Force Microscopy*; Oxford University Press: New York, 2010.
(8) O'Haver, T. *ipf.m Peak Fitter* http://terpconnect.umd.edu/~toh/spectrum/InteractivePeakFitter.htm.

Chapter 7

SPATIAL, SPECTRAL, AND COHERENCE MAPPING OF SINGLE-MOLECULE SERS ACTIVE HOT SPOTS VIA THE DISCRETE-DIPOLE APPROXIMATION

My contribution to this work: I designed and performed the research that yielded figures 2-4. I generated figures 2-4. I was actively involved in editing the manuscript and the peer-review process.

This article has been cited 23 times as of November 16, 2015.[1,181]

THE JOURNAL OF PHYSICAL CHEMISTRY Letters

LETTER

pubs.acs.org/JPCL

Spatial, Spectral, and Coherence Mapping of Single-Molecule SERS Active Hot Spots via the Discrete-Dipole Approximation

Jonathan P. Litz,[†] Jon P. Camden,[‡] and David J. Masiello*[,†]

[†]Department of Chemistry, University of Washington, Seattle, Washington 98195-1700, United States

[‡]Department of Chemistry, University of Tennessee, Knoxville, Tennessee 37996-1600, United States

ABSTRACT: The electromagnetic scattering properties of Ag nanoparticle aggregates known to be antennas for single-molecule surface-enhanced Raman scattering are investigated from a continuum electrodynamics perspective. High-resolution mappings of the spatial, spectral, and polarization dependence of the volumes of the aggregate's electromagnetic hot spots reveal multiple active regions for enhanced Raman scattering activity by molecular chromophores. Further analysis of these regions using maps of polarization surface-charge density shows that some hot spots are due to the collective and phase-coherent excitation of localized surface-plasmon resonances, whereas others derive from interfering plasmonic excitations resulting from scattering from gaps and surfaces. The latter are still capable of generating intense local fields at certain excitation energies, whereas the former tend to provide the most spatially delocalized regions of high electromagnetic-field strength.

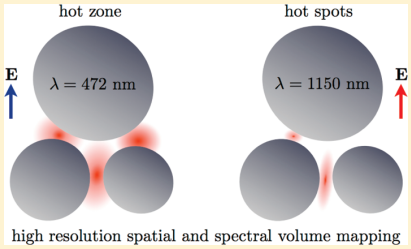

SECTION: Nanoparticles and Nanostructures

Over 30 years ago, a giant Raman scattering effect now known as surface-enhanced Raman scattering (SERS) was discovered.[1] In 1997, Nie and Emory[2] and Kneipp et al.[3] harnessed this effect to measure the Raman-scattering spectrum from a single molecule. Since these discoveries, numerous research efforts have focused on optimizing single-molecule SERS (SMSERS) with particular attention paid to understanding the properties of the nanoconfined light established by nanoscale metallic particles.[4,5] Initially believed to require electromagnetic enhancement factors as great as 10^{14}, in 2007, Etchegoin and coworkers[6] proved that hot spots with enhancement factors on the order of 10^{7} to 10^{8} are sufficient to support SMSERS. Recently, Willets and coworkers[7] and Zhang and coworkers[8] performed high-resolution imaging of the hot spots of a variety SMSERS-active metallic nanoparticle aggregates. Each determined the 2D spatial distribution of hot-spot intensity: Willets with 10 nm resolution and Zhang with 1.2 nm resolution. However, in neither of these experiments were the nanoparticle aggregates themselves imaged, making it impossible to correlate the underlying localized surface-plasmon resonances (LSPRs) to the volume and magnitude of the hot spots.

In 2008, Camden et al. investigated the SMSERS activity of rhodamine 6G (R6G) adsorbed onto several colloidally formed silver nanoparticle aggregates using resonant Raman and dark-field scattering spectroscopies correlated with high-resolution transmission electron microscopy (HRTEM).[9] Particular attention was paid to the optical properties of the dimer shown in Figure 1 (left panel) at 532 nm, the wavelength at which the resonant Raman experiment was performed. There, calculations based on continuum electromagnetic theory revealed a ~100-fold enhancement of the local electric field in comparison with the incident due to the excitation of a LSPR in silver. This is consistent with an enhanced Raman-scattering cross section of $\sim 10^{-14}$ cm^2, which is eight orders of magnitude larger than the 10^{-22} cm^2 resonant-Raman cross section of R6G.[10] This value was found only within certain spatial regions lying in the junctions of the particles constituting the dimer.

Theoretical analyses like these aid in elucidating the role that LSPRs play in SMSERS and SERS in general. When high-resolution images are available from experiment, additional properties can be extracted from the theory that have yet to be explored and that may provide further insight.[11] One such example is the spatial and spectral mapping of the volumes of regions of high electric field strength. Both the total volume and spatial distributions of these hot spots are difficult to determine experimentally because of the diffraction limit of light,[7,8,12−16] and limited theoretical work has been performed to correlate the nature of the underlying LSPRs to these observables.[15−18] In this Letter, we use volume calculations, hot-spot spatial distributions, polarization surface-charge density mappings, extinction spectra, and enhancement-factor spectra together to investigate the electromagnetic scattering properties of three Ag nanoparticle aggregates experimentally determined to be SMSERS active at 532 nm.[9] These studies not only contribute to the understanding of SMSERS but also will aid in the design of plasmonic devices.[19] For example, understanding how to extremize hot-spot volume is key to the development of plasmon-enhanced solar cells, which benefit from large spatial areas of enhancement over broad spectral regions to maximize their efficiency.[20]

Received: June 2, 2011
Accepted: June 20, 2011
Published: June 20, 2011

   dx.doi.org/10.1021/jz200743t | *J. Phys. Chem. Lett.* 2011, 2, 1695–1700

Armed with this new, richer toolkit, we are able to discern highly localized electromagnetic hot spots generated by the collective yet interfering excitations of metallic conduction electrons from the more spatially delocalized hot "zones" resulting from the collective and phase-coherent excitation of LSPRs. For each of the three aggregates, we find hot zones to be responsible for the Raman enhancement of a single R6G molecule near 532 nm.[9] Nonetheless, the existence of the former opens the door to new properties and processes that may take advantage of these relatively smaller yet sometimes more intense hot spots. In addition, certain nanoaggregates possess multispectral regions of high local-field strength of both hot spot and hot zone character. Understanding the electromagnetic properties of such regions would be important in plasmon-enhanced nonlinear spectroscopies such as surface-enhanced hyper-Raman scattering.[21]

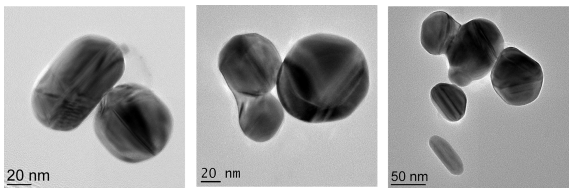

Figure 1. HRTEM images of three Ag nanoparticle aggregates experimentally determined to be SMSERS-active reproduced from ref 9.

The fact that certain nanoparticle aggregates possess polarization-dependent electromagnetic hot spots at multiple excitation wavelengths and spatial locations gives impetus to the following open questions: How large are these hot spots, that is, what is their accessible volume for varying enhancement-factor thresholds? Where are they located spatially with respect to the nanostructure, and are they contiguous or discontiguous? Are the underlying conduction electronic excitations in the metal phase-coherent? Must plasmon resonances be completely phase-coherent to be useful for enhanced molecular spectroscopy? We now seek to answer these questions through a detailed continuum-electrodynamics investigation based on the discrete-dipole approximation (DDA)[22] parametrized by bulk dielectric data;[23] the full

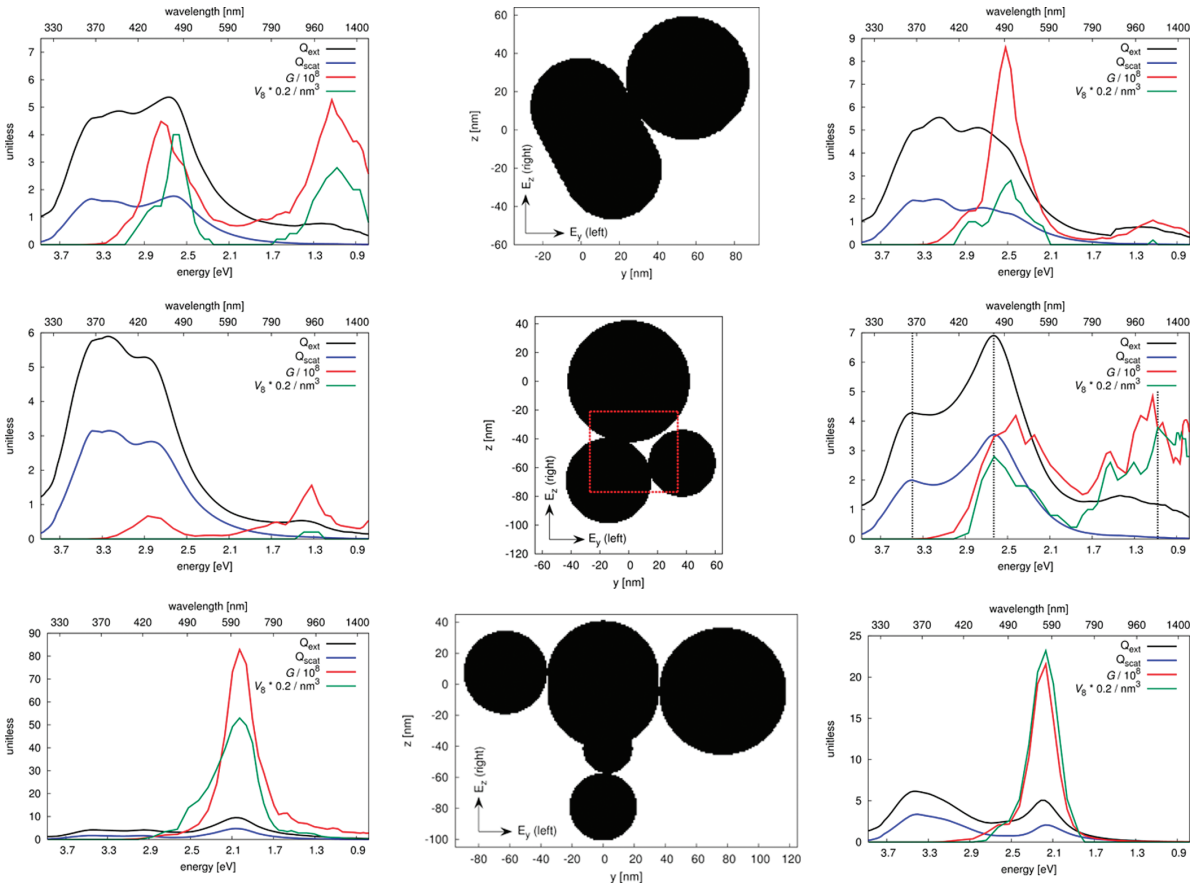

Figure 2. Extinction coefficient $Q_{ext} \equiv \sigma_{ext}/\sigma_{geom}$ (black), scattering coefficient $Q_{scat} \equiv \sigma_{scat}/\sigma_{geom}$ (blue), coarse-grained hot-spot volume V_8 (green), and spectral electromagnetic-enhancement factor G (red) versus excitation energy and wavelength. The wave vector of the plane-wave excitation field is propagating normally into the page and is linearly polarized along the y (left panels) and z (right panels) axis in the frame of the target (center panels). The red box overlaid upon the trimer (middle, center) corresponds to the magnified spatial region shown in Figure 3 where the high-resolution hot-spot volumes V_S are computed. The dotted lines in the trimer spectrum (middle, right) denote excitation wavelengths that are studied in Figures 3−5.

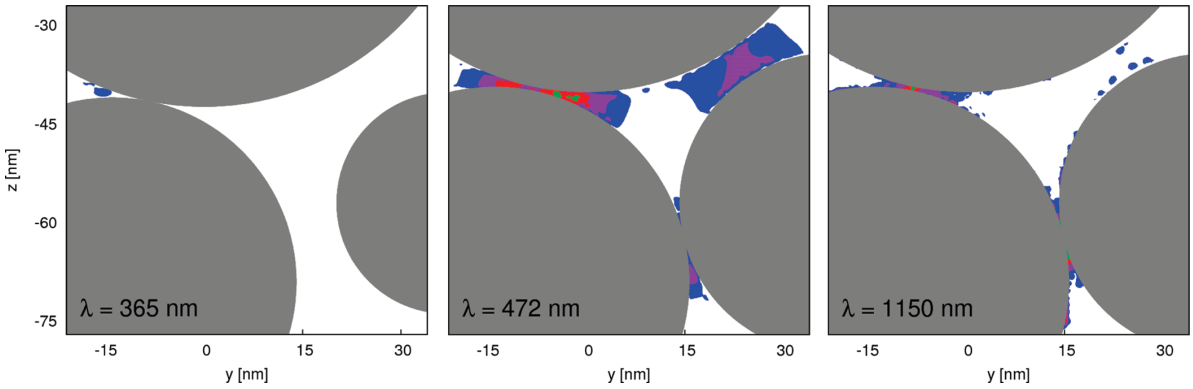

Figure 3. Magnified spatial maps of basic hot-spot volume elements $\tilde{v}_S(\mathbf{x}_k, \omega)$ at three different excitation wavelengths for initially z-polarized light. The x position is chosen so that each map is displayed in the $y-z$ plane where V_S takes its maximum value at wavelength λ. Because this plane coincides with the field grid and not the dipole grid (the two are offset by 0.5 nm in all three coordinate directions), we interpolate the boundaries of the target onto the field grid for the purpose of the Figure. Overlaid colors indicate the progression from $S = 5-8$ as V_5 (blue), V_6 (purple), V_7 (red), V_8 (green). Each panel corresponds to the region of the trimer enclosed in the red box in Figure 2.

effects of retardation are included, but all chemical effects are ignored.

Using the HRTEM images from ref 9, we have built 3D numerical representations (Figure 2, center panels) of the three Ag nanoparticle aggregates shown in Figure 1. Computation of the electromagnetic field scattered from each allows us to map the volume of the spatial region(s) where the local field is intense enough to boost the Raman signal from a single molecule to the point of detection. The threshold value for SMSERS activity of R6G is typically associated with an electromagnetic enhancement factor

$$g(\mathbf{x}, \omega) = |\mathbf{E}_{\mathrm{loc}}(\mathbf{x}, \omega)|^4 / |\mathbf{E}_0(\mathbf{x}, \omega)|^4 \qquad (1)$$

of 10^8, assuming that chemical enhancement effects are of order unity.[6] This means that the collection of all points $\mathbf{x}$ where the ratio of the fourth power of the local scattered electric field to the incident is $\geq 10^8$ would constitute a SMSERS-active region. Associated with each would be a finite hot-spot volume depending on the polarization state, frequency, and propagation direction of incident radiation

Numerically, the smallest discretized unit of volume is set by the spacing of the 3D grid used to compute the scattered electromagnetic field. We refine the field grid through a two-step process that allows us to image the hot spot in high resolution in a computationally tractable manner. First, a coarse-grained mapping of the field is computed on a set of uniformly spaced points separated by $l = 1$ nm in each direction; these points are displaced from the underlying dipole grid by 0.5 nm in all three coordinate directions where the dipoles $\mathbf{p}_j$ are also uniformly separated by $d = 1$ nm in each direction. This means that the closest distance between a dipole lying on the surface of the target and a point where the field is calculated is $3^{1/2} \cdot 0.5$ nm ≈ 0.87 nm and the closest distance between any two nanoparticles is 1 nm. These distances are larger than the critical distance of ~0.5 nm, below which quantum-mechanical effects such as charge transfer become important,[24,25] justifying our use of classical electromagnetic theory. Each field point that lies external to the target is then screened by the metric $g(\mathbf{x}_k, \omega) \geq 10^S$, for $S = 5-8$, and we define $v_S(\mathbf{x}_k, \omega) = \tilde{l}^3 = (1\ \mathrm{nm})^3$ to be the basic unit of field volume at $\mathbf{x}_k$ at the excitation frequency ω with $g(\mathbf{x}_k, \omega) \geq 10^S$; the dependence of v_S and g on excitation field wave vector and polarization is not explicitly indicated in the notation. The collection of all such volume elements $v_S(\mathbf{x}_k, \omega)$ comprises the total accessible volume

$$V_S(\omega) = \sum_{\mathbf{x}_k} v_S(\mathbf{x}_k, \omega) \qquad (2)$$

Therefore, the active hot-spot volume for SMSERS corresponds to V_8. It will be shown that neither the spatial nor the spectral distribution of V_S needs to be contiguous. Second, we search through all basic volume elements v_S in three dimensions for a fixed state of the excitation field and find the plane normal to the propagation direction, which is intersected by the largest number of v_S elements. We then enrich the field grid in this plane to have the uniform spacing $\tilde{l} = 0.1$ nm in both directions, corresponding to $\tilde{v}_S(\mathbf{x}_k, \omega) = \tilde{l}^3 = (0.1\ \mathrm{nm})^3$ for each observation point. Obtaining such images in other planes could be achieved in a similar manner, thereby yielding a high-resolution 3D map of the hot spot(s). The benefit of using this two-step process is that it allows us to compute the electromagnetic field in a computationally tractable manner. Without remeshing the field grid, as previously outlined, it would not be possible to perform such calculations at $\tilde{l} = 0.1$ nm because of the large sizes of the nanoparticle aggregates under consideration.

The spectral and polarization dependence of the coarse-grained hot-spot volumes V_8 (green) for the three SMSERS-active nanoparticle aggregates are presented in Figure 2. Two-dimensional projections of each 3D structure are displayed in the center panels; in each case, the background medium was chosen to be vacuum, and the exciting field's wave vector points normally into the page. The extinction (black) and scattering (blue) spectra are also displayed for comparison, as is the spectral dependence of the maximum enhancement factor (red)

$$G(\omega) = \max_{\mathbf{x}_k} g(\mathbf{x}_k, \omega) \qquad (3)$$

From G, it is evident that each of the three nanoparticle aggregates is able to support SMSERS at 532 nm, even though G is not maximized at this wavelength. In addition to the maximum in G near 532 nm, both the dimer (top) and the

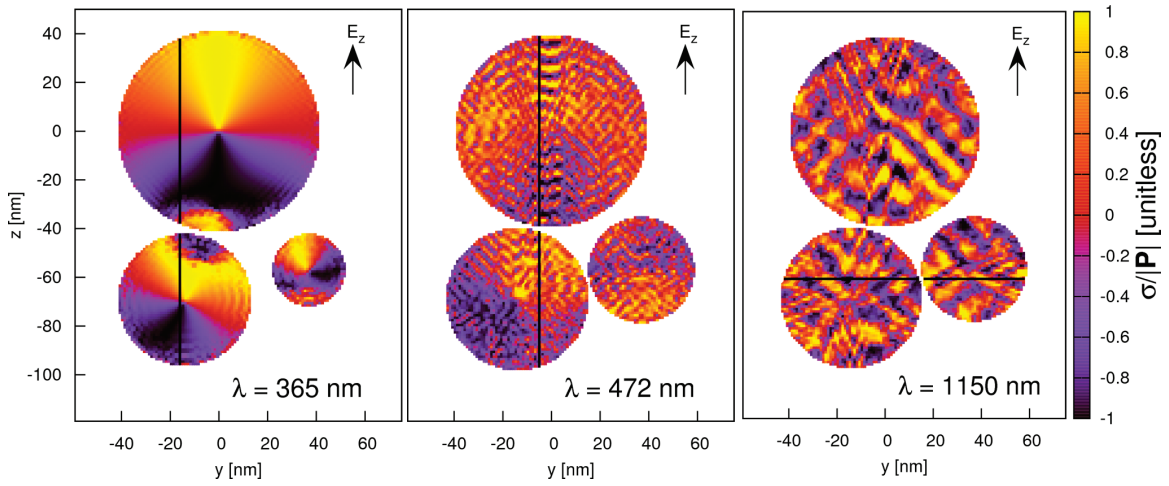

Figure 4. Spatial distribution of normalized polarization surface-charge density $\tilde{\sigma} = -\hat{\mathbf{n}}\cdot\mathbf{P}/|\mathbf{P}|$ of the Ag nanosphere trimer at three different excitation wavelengths for initially z-polarized light. The x position is chosen so that each map is rounded to the nearest $y-z$ plane of dipoles from where V_S takes its maximum value at wavelength λ. For each excitation energy, the vertical (horizontal) lines intersect the (x,y)-point ((x,z)-point) where G attains its maximum value on this plane. The variation of σ with z (y) along each line is displayed in Figure 5.

trimer (middle) exhibit secondary maxima in G further to the red that are also large enough to support SMSERS activity ($V_8 > 0$).

We now focus specifically on the silver trimer. Figure 3 presents high-resolution 2D spatial maps of the trimer's basic hot-spot volumes $\tilde{v}_S(\mathbf{x}_k, \omega)$ for $S = 5-8$ at the excitation wavelengths 365, 472, and 1150 nm for initially z-polarized light. These wavelengths are chosen because the trimer exhibits a local maximum in Q_{ext} at 365 nm and local maxima in V_8 at 472 and 1150 nm; they are denoted by the vertical dotted lines in Figure 2 (center, right). Although not shown explicitly, it should be noted that all calculations performed at 532 nm are qualitatively similar to those performed at 472 nm. The overlaying colors in Figure 3 indicate the progression in S from 5 to 8, $S = 5$ (blue), 6 (purple), 7 (red), and 8 (green). Each map is displayed in the $y-z$ plane intersecting the x position where V_S attains its maximum value. Interestingly, these volume maps demonstrate that the spatial region of high field strength at 472 nm is more delocalized than that at 1150 nm when all points with $g \geq 10^5$ are included. The former is also more discontiguous than the latter with local fields distributed across the junctions of all three constituent nanoparticles of the trimer. We call such a spatially delocalized region of high electric-field strength a hot zone. The Raman scattering of light from a molecule like R6G may be affected in a hot zone by the molecule's ability to access all components of its volume V_5-V_8. This would be possible if a chemical-enhancement mechanism existed with a magnitude on the order of 10^3, requiring only a factor of 10^5 from the electromagnetic enhancement effect to reach 10^8.[26] Nanoparticle aggregates exhibiting such hot-zone character may be well-suited for certain solar-cell architectures by allowing more chromophores to participate in the plasmon-enhanced absorption of solar radiation.[20]

To aid in our understanding of the previous results, we define the polarization surface-charge density

$$\sigma(\mathbf{r}_j, \omega) = -\hat{\mathbf{n}}_j \cdot \mathbf{P}_j(\mathbf{r}_j, \omega) \quad (4)$$

It is a measure of the degree of coherence of the electronic excitation (or electronic polarization) in the metal as induced to first order by the perturbing radiation field. Here $\mathbf{P}_j = \mathbf{p}_j/d^3$ is the polarization of the target in the region of volume d^3 centered at $\mathbf{r}_j$ and $\hat{\mathbf{n}}_j$ is the unit outward normal vector at each point within and along the target surface centered at $\mathbf{r}_j$. Because interior points $\mathbf{r}_j$ are also included, σ contains coherence information about the bulk as well; effects of higher-order multipoles beyond the electric dipole are partially included in σ through the interaction and collective motion of the DDA dipoles. Figure 4 displays spatial distributions of the normalized polarization surface-charge density $\tilde{\sigma} = -\hat{\mathbf{n}}\cdot\mathbf{P}/|\mathbf{P}|$ at the excitation wavelengths 365, 472, and 1150 nm for initially z-polarized light.

If the entire nanoparticle assembly is coherently excited its plasmon resonance(s) will be a hybridization of the individual plasmon resonances of its constituent monomers.[27] Coherence is manifested in the phases of the plasmon densities of all particles in the collection. At certain excitation wavelengths, the phase may be a slowly varying function of space except at a few isolated points where it suddenly changes sign, whereas at other excitation wavelengths it may oscillate repeatedly throughout the interior of the target. The latter may be attributed to the interference of surface plasmons generated by the light scattered from surface and gap features of the metal nanostructure.[28] For example, when illuminated by light, a gap of size $D = 1.12$ nm between two nanoparticles scatters radiation with wave vector magnitude $k_{gap} = 2\pi/D$; the energy E associated with this radiation is capable of driving surface conduction electrons into nearly free motion with energy $E = \hbar^2 k_{gap}^2/2m \approx 1.08$ eV $\approx hc/(1150\text{ nm})$, which may then interfere with the bulk plasmon density. Despite these interferences, such excitations are still coherent and may support local fields of large enough intensity to enable SMSERS as well as other plasmon-enhanced molecular-optical scattering processes.

From the spatial distributions of $\tilde{\sigma}$ in Figure 4, it is evident that the collective behavior of the metallic conduction electrons at 365 nm is phase coherent, yielding a hybridized plasmon resonance of the trimer similar to the first case discussed above. Interestingly, in addition to this delocalized coherent state made up largely from dipole plasmon resonances on each particle, there

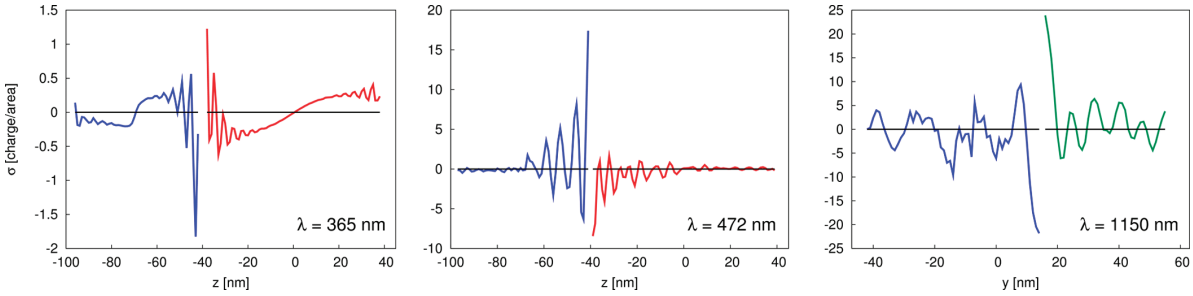

Figure 5. Spatial profile of (non-normalized) polarization surface-charge density $\sigma = -\hat{\mathbf{n}}\cdot\mathbf{P}$ of the Ag nanosphere trimer at three different excitation wavelengths for initially *z*-polarized light. For each excitation wavelength, the displayed spatial profiles correspond with the horizontal (vertical) lines shown in Figure 4. Blue is used to denote the left most, red the upper most, and green the right most particle of the trimer.

exists a small-scale polarization gradient localized at the junction between the upper and lower left particles; this feature signifies the emergence of new plasmons of different multipolar character. As the excitation wavelength is increased to 472 nm, small-amplitude phase oscillations emerge in the LSPR density across the three nanoparticles, growing larger near the interparticle junctions due to the interference of gap plasmons, as discussed previously in the second case. However, the trimer as a whole is still partially phase-coherent; a hybridized dipole-like resonance is clearly visible beneath the interference fringes. At the even longer excitation wavelength of 1150 nm, the density of metallic conduction electrons exhibits severe interference features, both in fringe contrast and spatial extent into the bulk. A hybridized plasmon resonance can no longer be seen beneath the large-scale modulations of its phase, yet even at 1150 nm the plasmon exhibits coherence but is dephased by the light diffracted from surfaces and gaps. Calculations on smaller nanoparticle dimers and monomers (with 50 nm diameters) with interdipole separations d ranging from 1, 0.75, 0.5, to 0.25 nm all reveal such interference effects with fringe contrast depending only weakly on d, validating our observations.

One might expect that the former resonance at 365 nm, being the most phase-coherent excitation of the three considered, would produce the largest electromagnetic enhancement factor. However, in light of the spectrum displayed in Figure 2, we see that this is not the case. Rather, the plasmonic excitation at 365 nm has the smallest value of G, and the excitation at 1150 nm has the largest value of G. This surprising observation can be rationalized, in part, by the data presented in Figure 5, which show the spatial profile of the polarization surface-charge density versus a single coordinate with the remaining two coordinates held fixed. The latter two are chosen to coincide with the spatial position where G attains its maximum value in the plane where V_S is maximized at each excitation wavelength; the former coordinate is varied along an axis that couples the two dominant particles participating in the resonance. It is evident that the 365 nm excitation yields the most phase-coherent response of the trimer's conduction electrons, with a large-scale dipole-like distribution of charge on each particle. Here the magnitude of the difference in surface-charge density on adjacent particles is $|\sigma_{top} - \sigma_{left}| \approx |1.2 - (-0.32)| = 1.5$ units of charge/area. The behavior of the electronic response at 472 nm is qualitatively similar to that at 365 nm but with the addition of small-amplitude phase oscillations in σ as well as the omission of the small-scale local polarization gradient between particles. Here we find the largest boost in magnitude of the difference in σ, a value of $|\sigma_{top} - \sigma_{left}| \approx |-8.4 - 17.4| = 25.8$ units of charge/area. This potential difference is a factor of 17.2 larger than the potential difference at 365 nm. The trend of increasing difference in polarization surface-charge density continues in the red at 1150 nm. There, the magnitude of the difference in σ is $|\sigma_{right} - \sigma_{left}| \approx |-22.8 - 23.9| = 46.7$ units of charge/area, which is a 1.8-fold increase from that at 472 nm and a 31-fold increase from that at 365 nm. Taken together with the spectra presented in Figure 2, these spatial profiles clearly indicate that it is the greater difference in polarization at the surface of the coupled nanoparticles that leads to the largest spectral enhancement factors and not necessarily the degree of phase coherence of the plasmon mode. Further studies of the spatial breadth of the polarization difference show that the hot zone at 472 nm dies off much more slowly than the hot spot at 1150 nm.

In summary, we have studied the optical-scattering properties of three Ag nanoparticle aggregates known to be SMSERS-active. Based on the HRTEM image of each, we have numerically investigated the spatial, spectral, and polarization dependence of their electromagnetic hot-spot volumes and their polarization surface-charge densities. We have learned that regions of high electromagnetic-field strength can be generated at multiple spectral and spatial locations and need not be contiguous. Some of these regions are spatially delocalized as well as intense and are due to the phase-coherent excitation of LSPRs. Other regions of high field strength stem from the collective and coherent excitations of conduction electrons that have interfered and dephased because of the scattering of plasmons and light from surface and gap features of metal nanoparticle aggregates. Both types of resonance may support a variety of plasmon-enhanced optical processes in nearby molecular chromophores.

AUTHOR INFORMATION

Corresponding Author

*E-mail: masiello@chem.washington.edu.

ACKNOWLEDGMENT

This material is based on work supported by the National Science Foundation Graduate Research Fellowship under grant no. DGE-0718124 (J.P.L.). This work was supported by the University of Tennessee, the UT/ORNL Joint Institute for Advanced Materials, and the U.S. Department of Energy, Office

of Basic Energy Sciences under award number DE-SC0004792 (J.P.C.). D.J.M. acknowledges financial support from the University of Washington College of Arts and Sciences and Department of Chemistry.

REFERENCES

(1) Jeanmaire, D. L.; Van Duyne, R. P. Surface Raman Spectroelectrochemistry: Part I. Heterocyclic, Aromatic, and Aliphatic Amines Adsorbed on the Anodized Silver Electrode. *J. Electroanal. Chem.* **1977**, *84*, 1–20.

(2) Nie, S.; Emory, S. R. Probing Single Molecules and Single Nanoparticles by Surface-Enhanced Raman Scattering. *Science* **1997**, *275*, 1102–1106.

(3) Kneipp, K.; Wang, Y.; Kneipp, H.; Perelman, L. T.; Itzkan, I.; Dasari, R. R.; Feld, M. S. Single Molecule Detection Using Surface-Enhanced Raman Scattering (SERS). *Phys. Rev. Lett.* **1997**, *78*, 1667–1670.

(4) Michaels, A. M.; Jiang, J.; Brus, L. Ag Nanocrystal Junctions as the Site for Surface-Enhanced Raman Scattering of Single Rhodamine 6G Molecules. *J. Phys. Chem. B* **2000**, *104*, 11965–11971.

(5) Hao, E.; Schatz, G. C. Electromagnetic Fields around Silver Nanoparticles and Dimers. *J. Chem. Phys.* **2004**, *120*, 357–366.

(6) Le Ru, E. C.; Blackie, E.; Meyer, M.; Etchegoin, P. G. Surface Enhanced Raman Scattering Enhancement Factors: A Comprehensive Study. *J. Phys. Chem. C* **2007**, *111*, 13794–13803.

(7) Stranahan, S. M.; Willets, K. A. Super-Resolution Optical Imaging of Single-Molecule SERS Hot Spots. *Nano Lett.* **2010**, *10*, 3777–3784.

(8) Cang, H.; Labno, A.; Lu, C.; Yin, X.; Liu, M.; Gladden, C.; Liu, Y.; Zhang, X. Probing the Electromagnetic Field of a 15-Nanometre Hotspot by Single Molecule Imaging. *Nature* **2011**, *469*, 385–388.

(9) Camden, J. P.; Dieringer, J. A.; Wang, Y.; Masiello, D. J.; Marks, L. D.; Schatz, G. C.; Van Duyne, R. P. Probing the Structure of Single-Molecule Surface-Enhanced Raman Scattering Hot Spots. *J. Am. Chem. Soc.* **2008**, *130*, 12616–12617.

(10) Shim, S.; Stuart, C. M.; Mathies, R. A. Resonance Raman Cross-Sections and Vibronic Analysis of Rhodamine 6G from Broadband Stimulated Raman Spectroscopy. *ChemPhysChem* **2008**, *9*, 697–699.

(11) Perassi, E. M.; Hernandez-Garrido, J. C.; Moreno, M. S.; Encina, E. R.; Coronado, E. A.; Midgley, P. A. Using Highly Accurate 3D Nanometrology to Model the Optical Properties of Highly Irregular Nanoparticles: A Powerful Tool for Rational Design of Plasmonic Devices. *Nano Lett.* **2010**, *10*, 2097–2104.

(12) Kim, K.; Shin, D.; Kim, K. L.; Shin, K. S. Electromagnetic Field Enhancement in the Gap between Two Au Nanoparticles: the Size of Hot Site Probed by Surface-Enhanced Raman Scattering. *Phys. Chem. Chem. Phys.* **2010**, *12*, 3747–3752.

(13) Chen, C.; Hutchinson, J. A.; Clemente, F.; Kox, R.; Uji-I, H.; Hofkens, J.; Lagae, L.; Maes, G.; Borghs, G.; Dorpe, P. V. Direct Evidence of High Spatial Localization of Hot Spots in Surface-Enhanced Raman Scattering. *Angew. Chem., Int. Ed.* **2009**, *48*, 9932–9935.

(14) Farcau, C.; Astilean, S. Mapping the SERS Efficiency and Hot-Spots Localization on Gold Film over Nanospheres Substrates. *J. Phys. Chem. C* **2010**, *114*, 11717–11722.

(15) Rang, M.; Jones, A. C.; Zhou, F.; Li, Z.-Y.; Wiley, B. J.; Xia, Y.; Raschke, M. B. Optical Near-Field Mapping of Plasmonic Nanoprisms. *Nano Lett.* **2008**, *8*, 3357–3363.

(16) Nelayah, J.; Kociak, M.; Stéphan, O.; Geuquet, N.; Henrard, L.; Garcia de Abajo, F. J.; Pastoriza-Santos, I.; Liz-Marzán, L. M.; Colliex, C. Two-Dimensional Quasistatic Stationary Short Range Surface Plasmons in Flat Nanoprisms. *Nano Lett.* **2010**, *10*, 902–907.

(17) Le Ru, E. C.; Etchegoin, P. G.; Meyer, M. Enhancement Factor Distribution around a Single Surface-Enhanced Raman Scattering Hot Spot and its Relation to Single Molecule Detection. *J. Chem. Phys.* **2006**, *125*, 204701.

(18) Perassi, E. M.; Canali, L. R.; Coronado, E. A. Enhancement and Confinement Analysis of the Electromagnetic Fields inside Hot Spots. *J. Phys. Chem. C* **2009**, *113*, 6315–6319.

(19) Willets, K. A.; Van Duyne, R. P. Localized Surface Plasmon Resonance Spectroscopy and Sensing. *Annu. Rev. Phys. Chem.* **2007**, *58*, 267–297.

(20) Catchpole, K. R.; Polman, A. Plasmonic Solar Cells. *Opt. Express* **2008**, *16*, 21793–21800.

(21) Kelley, A. M. Hyper-Raman Scattering by Molecular Vibrations. *Annu. Rev. Phys. Chem.* **2010**, *61*, 41–61.

(22) Draine, B. T.; Flatau, P. J. Discrete-Dipole Approximation for Scattering Calculations. *J. Opt. Soc. Am. A* **1994**, *11*, 1491–1499.

(23) Lynch, D. W.; Hunter, W. R. In *Handbook of Optical Constants of Solids*; Palik, E. D., Ed.; Academic Press: New York, 1985; pp 275−367.

(24) Zuloaga, J.; Prodan, E.; Nordlander, P. Quantum Description of the Plasmon Resonances of a Nanoparticle Dimer. *Nano Lett.* **2009**, *9*, 887–891.

(25) Zuloaga, J.; Prodan, E.; Nordlander, P. Quantum Plasmonics: Optical Properties and Tunability of Metallic Nanorods. *ACS Nano* **2010**, *4*, 5269–5276.

(26) Fromm, D. P.; Sundaramurthy, A.; Kinkhabwala, A.; Schuck, P. J.; Kino, G. S.; Moerner, W. E. Exploring the Chemical Enhancement for Surface-Enhanced Raman Scattering with Au Bowtie Nanoantennas. *J. Chem. Phys.* **2006**, *124*, 061101.

(27) Prodan, E.; Radloff, C.; Halas, N. J.; Nordlander, P. A Hybridization Model for the Plasmon Response of Complex Nanostructures. *Science* **2003**, *302*, 419–422.

(28) McMahon, J. M.; Gray, S. K.; Schatz, G. C. Optical Properties of Nanowire Dimers with a Spatially Nonlocal Dielectric Function. *Nano Lett.* **2010**, *10*, 3473–3481.

Chapter 8

SUPER-RESOLUTION IMAGING REVEALS A DIFFERENCE BETWEEN SERS AND LUMINESCENCE CENTROIDS

My contribution to this work: I helped to establish this UW-University of Texas collaboration with my former Harvey Mudd College classmate, Maggie Weber. I proposed using Eq. 2 to predict Maggie's unexpected experimental results. I performed the research that yielded Fig. 4B, 4D, 5C, 5D and S7. I generated figures 4B, 4D, 5C, 5D, and S7. I aided in writing the theory portions of the manuscript.

This article has been cited 45 times as of November 16, 2015.[2,181]

This article was highlighted in "In Nano," *ACS Nano* **2012**, *6*, 990-992.[182]

Super-Resolution Imaging Reveals a Difference between SERS and Luminescence Centroids

Maggie L. Weber,[‡] Jonathan P. Litz,[†] David J. Masiello,[†,*] and Katherine A. Willets[‡,*]

[†]Department of Chemistry, University of Washington, Box 351700, Seattle, Washington 98195-1700, United States, and [‡]Department of Chemistry and Biochemistry, The University of Texas at Austin, 1 University Station A5300, Austin, Texas 78712, United States

ABSTRACT Super-resolution optical imaging of Rhodamine 6G surface-enhanced Raman scattering (SERS) and silver luminescence from colloidal silver aggregates are measured with sub-5 nm resolution and found to originate from distinct spatial locations on the nanoparticle surface. Using correlated scanning electron microscopy, the spatial origins of the two signals are mapped onto the nanoparticle structure, revealing that, while both types of emission are plasmon-mediated, SERS is a highly local effect, probing only a single junction in a nanoparticle aggregate, whereas luminescence probes all collective plasmon modes within the nanostructure. Calculations using the discrete-dipole approximation to calculate the weighted centroid position of both the $|E|^2/|E_{inc}|^2$ and $|E|^4/|E_{inc}|^4$ electromagnetic fields were compared to the super-resolution centroid positions of the SERS and luminescence data and found to agree with the proposed plasmon dependence of the two emission signals. These results are significant to the field of SERS because they allow us to assign the exact nanoparticle junction responsible for single-molecule SERS emission in higher order aggregates and also provide insight into how SERS is coupled into the plasmon modes of the underlying nanostructure, which is important for developing new theoretical models to describe SERS emission.

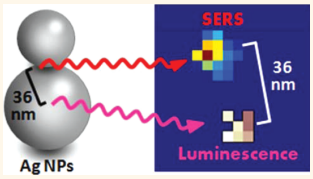

KEYWORDS: silver luminescence · surface-enhanced Raman scattering · hot spots · discrete-dipole approximation · plasmon

Many theoretical and experimental studies of metallic nanostructures have illustrated the importance of nanoparticle shape, size, and degree of aggregation upon the surface-enhanced Raman scattering (SERS) phenomenon, particularly the electromagnetic field enhancement in nanoparticle junctions.[1−6] Fully understanding how these variables, along with excitation wavelength and polarization, affect optical response will allow us to design reliable, robust SERS substrates. The challenge with characterizing SERS substrates is that the bulk of the enhancement occurs in "hot spots" located in the junctions between adjacent nanoparticles.[5,7] The small size of these hot spots in comparison to the diffraction limit of light, which restricts optical imaging resolution to roughly half the wavelength of the probing light, prevents optical imaging of hot spot size and geometry. Recently, super-resolution imaging was applied to the SERS problem in order to defeat the diffraction limit of light and probe the local behavior of molecules adsorbed to nanoparticle surfaces.[8−10] Our group and others have shown that a correlation exists between the super-resolution determined spatial origin of the SERS signal and the intensity of the measured SERS. This demonstrates the power of super-resolution imaging for understanding these complex nanoscale systems.[8−10]

In our previous work, we used super-resolution optical imaging to locate and track the spatial origin of the SERS signal from Rhodamine 6G (R6G) molecules on sodium-chloride-aggregated silver nanoparticle aggregates, taking advantage of the strong on/off signal fluctuations inherent to single- or few-molecule SERS.[8] During the periods when no SERS was observed, we found a weak silver photoluminescence background signal.[8] Using super-resolution imaging, we fit the spatial origin of both the SERS and luminescence signals and found that in some cases the strongest SERS emission was colocalized with the luminescence (within 5−10 nm), while in other cases, the position of the two signals was spaced by more than 50 nm. We speculated that the offset between the two signals was related to the structure of the nanoparticle aggregates, which are known to be diverse in these randomly assembled silver colloids.

To investigate the role of nanoparticle structure, we repeated this initial study using indium tin oxide (ITO)-coated glass coverslips as the substrate to enable correlated structural analysis with a scanning electron microscope (SEM).[9] However, the change in substrate and dielectric environment

* Address correspondence to masiello@chem.washington.edu, kwillets@mail.utexas.edu.

Received for review December 26, 2011 and accepted January 16, 2012.

Published online January 16, 2012
10.1021/nn205080q

modified the chemical dynamics of the system: where the on/off behavior of R6G SERS in the single-molecule concentration regime was exploited in previous studies, the comparative experiments on ITO glass showed fluctuating spectral features of R6G on top of an unstable background spectrum from sodium citrate, the reducing agent which caps the silver colloids during synthesis.[11−13] Figure 1A illustrates the type of R6G SERS spectra observed on ITO using NaCl-aggregated silver colloids. While the intensity time trace (Figure 1A, bottom) shows on/off signal behavior, there are peaks evident in the SERS spectra even when the signal intensity is low (Figure 1A, top). Moreover, the spectra corresponding to times when the SERS signal is "on" in the time trace (*e.g.*, 74 s) cannot be clearly identified as R6G. Thus, our reported SERS centroids are biased by a contribution from this unstable citrate background, and we are unable to assign the spatial origin of the silver luminescent background. This prevents us from explaining why the two signals are colocalized in some cases and offset in others.

In the present study, we address this problem by modifying the colloid aggregation chemical from sodium chloride to sodium bromide in order to improve citrate displacement, thereby eliminating any spectral signatures of citrate.[8,14,15] Figure 1B shows data collected from an R6G-labeled silver colloid sample aggregated with NaBr. The intensity time trace shows the same on/off behavior as in Figure 1A, but the associated spectra show characteristic R6G peaks only during the "on" times and a clean flat background during the "off" times (Figure 1B, bottom). Even though the spectra are featureless during the "off" times, we note that the intensity of the time trace never goes down to zero background, which indicates that silver photoluminescence is still present in the sample.[8] Thus, using this new nanoparticle aggregation strategy, we are able to relate the spatial origin of the observed luminescence to both the measured SERS signal from an adsorbed dye (as determined by super-resolution imaging) and the structure of the overall nanoparticle aggregate (as determined by electron microscopy). Computationally, Maxwell's equations are solved *via* the discrete-dipole approximation (DDA) to determine the continuum electromagnetic scattering properties of the metal nanoparticle aggregates.[16] From these calculations, the expected site of emission for plasmon-mediated processes following either $|\mathbf{E}|^2$ or $|\mathbf{E}|^4$ enhancement mechanisms is compared to the experimentally measured SERS and luminescence signals.

SERS super-resolution imaging is performed using wide-field epi-illumination with 532 nm excitation as described below. For each SERS-active aggregate of interest, we simultaneously collect a series of CCD images (1000 total at 0.1 s integration) and spectra (100 total at 1 s integration). The diffraction-limited

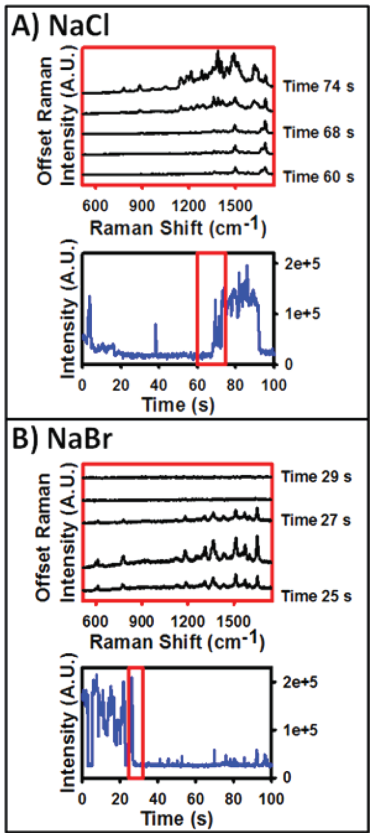

Figure 1. (A) Time trace of R6G SERS from a NaCl-aggregated silver colloid (bottom) and the associated SERS spectra for the red boxed region in the time trace (top). (B) Same as in (A) but for R6G SERS from a NaBr-aggregated silver colloid.

spot in each optical image, corresponding to a single SERS-active aggregate of interest, is fit to a two-dimensional Gaussian and its centroid determined so we can monitor the position of the SERS signal and the luminescence as a function of time.[8,9] This method, known as point spread function (PSF) fitting, was determined to be the most robust in low signal-to-noise situations such as single-molecule studies by Cheezum *et al.*,[17] and recently, Selvin *et al.* have reported PSF fitting with ∼1 nm resolution providing a significant advantage over the diffraction limit.[18,19] The PSF fit equations and method used in this article have been explicitly outlined in previous works.[8,9] Briefly, the Gaussian equation used to model the shape and intensity of a diffraction-limited spot is

$$I(x,y) = z_0 + I_0 e^{\left[-\frac{1}{2}\left[\left(\frac{x-x_0}{s_x}\right)^2 + \left(\frac{y-y_0}{s_y}\right)^2\right]\right]} \quad (1)$$

where I is the intensity for a given position (x,y) in space, z_0 is the background intensity, I_0 is the intensity at the center of the Gaussian fit, $s_{x,y}$ are the standard

deviation in x and y, respectively, and x_0 and y_0 are the centroid of the fit (see Supporting Information for more details). Individual frames in the image stack are assigned as originating from either nanoparticle luminescence or a combination of luminescence and SERS using the corresponding spectral data. A threshold is drawn in the intensity time trace such that all intensity events above the threshold have correlated Raman spectra exhibiting characteristic R6G peaks and all events below the threshold correspond to luminescence emission only (see Figure S-1 in Supporting Information for all time traces with thresholds and associated spectra for data described below). For all frames designated as luminescence emission only (*i.e.*, below the intensity threshold), a Gaussian function is fit to each emission pattern in order to determine its centroid position (*i.e.*, x_0 and y_0). The average position of the luminescence centroid is calculated over all frames and checked for positional stability by calculating the standard deviation in the centroid position. For all aggregates discussed in this article, the standard deviations of the fit of the luminescence centroids ranged from 1 to 6 nm (Figures S-3 and S-5). The theoretical accuracy of the luminescence centroid is 0.9 nm based on our pixel size, standard deviation of the fitted Gaussian, and signal-to-noise (Table S-1).[19] Once we establish that the luminescence originates from a single, stable location for a given SERS-active colloidal aggregate, we arbitrarily set the average position of the luminescence centroid to (0,0).

Next, all frames with intensities above the threshold are processed to exclude the contribution from the luminescence and then fit as a single 2-D Gaussian to extract the SERS centroid.[8] Although this analysis assumes that only a single R6G is contributing to the signal at a given time, we cannot exclude the possibility of multiple emitters contributing simultaneously to a single image. In this case, the emission centroid would be the superposition of the location of the different emitting species. We have chosen our dye concentration to be in a similar range to those used in single-molecule SERS proof-of-concept studies with identical colloid synthesis (Lee and Meisel method) in order to favor the likelihood that only a single molecule is present on the nanoparticle surface.[20−22] Moreover, in the case of two emitters present on the surface, we note that the fluctuating nature of the SERS signal would lead to times at which both molecules are emitting, times at which one or the other is emitting, and times when neither is emitting. Using a bianalyte technique, Van Duyne and co-workers have shown that even at high dye concentrations (~100 molecules per nanoparticle) signal is only observed from one molecular species at a time, suggesting that a single hot spot can only be occupied by one molecule at a time.[23] Thus, for events corresponding to two molecules emitting at the same time, the two molecules would have to occupy spatially distinct hot spots. We expect this to produce three distinct centroids, two of which correspond to the location of each unique hot spot determined when only a single molecule is emitting, as well as the superposition of the two centroids determined during times at which both are emitting simultaneously. In the data presented here, we do not observe multiple distinct SERS centroids, although we have previously reported this phenomenon in another system.[9] Thus, our data support that the SERS originates from a single emitter, although bianalyte studies are underway to rigorously verify this.

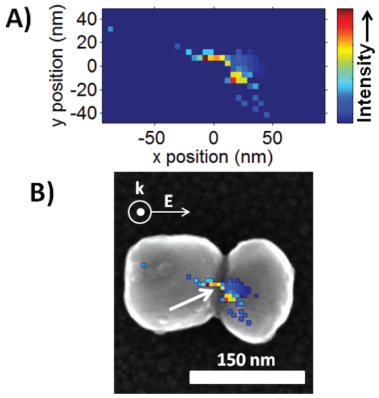

Figure 2. (A) SERS spatial intensity map, showing the relationship between the SERS intensity (color scale) and the spatial origin of the SERS signal with respect to the luminescence centroid at (0,0). (B) Overlay of the SERS spatial intensity map and luminescence centroid (tip of white arrow) with an SEM image of the SERS-active silver nanoparticle aggregate.

After we have determined the SERS centroid positions for all frames above the intensity threshold, the centroid data are binned to create a two-dimensional position histogram (0.1 pixel or 4.6 nm bin size). This bin size is chosen based on the theoretical resolution of ~5 nm for the weakest SERS signal (Table S-1). We then calculate the average SERS intensity for all points within a bin to create a SERS spatial intensity map, which illustrates where regions of most intense SERS scattering occur; an example is shown in Figure 2A (see Supporting Information for more details regarding fitting procedure and data processing).

RESULTS AND DISCUSSION

For the data shown in Figure 2A, there are two regions of "hot" SERS activity, located on either side of the luminescence centroid at (0,0). The corresponding SEM image, shown in Figure 2B, reveals that the SERS-active nanoparticle is a dimer, oriented parallel to the excitation polarization.

Theoretical calculations in the literature have long indicated that the most intense SERS is expected to originate from the junction between aggregated nanoparticles, especially for a dimer excited along its long

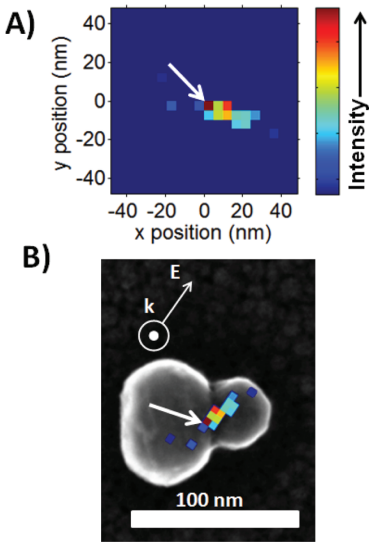

Figure 3. (A) R6G SERS spatial intensity map and associated luminescence centroid (arbitrarily set to (0,0) and indicated by a white arrow). (B) Overlay of luminescence centroid and spatial intensity map with correlated nanoparticle SEM image. Note that the spatial intensity map has been rotated to match the orientation of the SEM image.

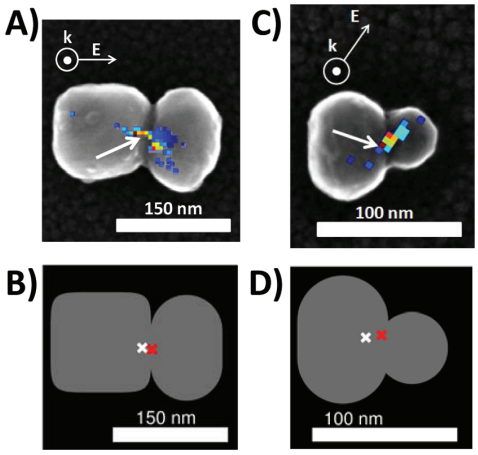

Figure 4. (B,D) DDA calculations for experimental nanoaggregates in Figures 2 and 3 (reproduced in A and C, respectively). The ε^2 centroids are identified by white Xs, and ε^4 centroids are identified by red Xs. The polarization angles for B and D match those of their corresponding experimental structures.

axis.[4,6,24−26] In the case of dimers with small gaps between them, the highest electromagnetic field enhancements are calculated to fall on the edges of the two nanoparticles that face the junction, with a minimum in the gap itself.[27] We note that the spatial intensity map in Figure 2A has a spatial distribution of the SERS signal that is similar to the predicted electromagnetic field distribution for nontouching dimers. For this reason, we overlay the SERS spatial intensity data onto the SEM data in Figure 2B such that the two regions of strong SERS are located on either side of the junction, consistent with the expectations from theory. Although this overlay is not mathematically rigorous, it agrees with theoretical expectations and serves as a reasonable initial guess. Attempts to quantitatively assign the spatial origin of the SERS centroid *via* triangulation using alignment markers produces an accuracy of ~50 nm, which is insufficient for assigning the hot spot location. We observe some variation in the position of the SERS emission centroid, which we attribute to a mobile dipole on the nanoparticle surface as discussed in our previous work.[8] On the basis of our super-resolution fits, we see colocalization of the average position of the luminescence signal (tip of white arrow) with the strongest SERS, indicating that if our placement of the spatial intensity map is correct, then the luminescence signal is also associated with the junction between the two nanoparticles in this dimer.

Figure 3 presents the SERS spatial intensity map (Figure 3A) and associated structure (Figure 3B) of an asymmetric dimer with one particle significantly larger than the other and whose long axis is oriented roughly 45° from the laser polarization. As before, we place the regions of strongest SERS signal on either side of the junction, consistent with the presence of a small gap. In this case, we observe that placing the SERS centroid on the nanoparticle junction leads to a small (~10 nm) offset in the luminescence centroid away from the junction and toward the larger nanoparticle.

To quantitatively assign the position of the SERS centroid, we use our SEM images to construct a three-dimensional numerical representation of each nanoparticle aggregate in DDA. From the output of DDA, one may construct a near-field mapping of the electromagnetic field enhancement surrounding the nanostructure.[2−5,28,29] We calculated the ratio of the magnitude of the local electric field **E** to the magnitude of the incident electric field $\mathbf{E}_{inc}$, $\varepsilon = |\mathbf{E}|/|\mathbf{E}_{inc}|$, on a grid with 1 nm^3 resolution in the region that encapsulates the near-field behavior of **E** at an excitation wavelength of 532 nm. The near-field map of ε was translated into a far-field centroid position, $\langle \mathbf{X} \rangle$, by calculating the weighted average of the position in the enhanced electromagnetic field distribution. The weighting factor was ε^2 for luminescence and ε^4 for SERS:

$$\langle \mathbf{x} \rangle(\omega) = \frac{\sum_i \mathbf{x}_i f(\varepsilon(\mathbf{x}_i, \omega))}{\sum_i f(\varepsilon(\mathbf{x}_i, \omega))} \qquad (2)$$

$$f(\varepsilon) = \begin{cases} \varepsilon^2 \text{ for luminescence} \\ \varepsilon^4 \text{ for SERS} \end{cases}$$

We chose to model both the ε^2 and ε^4 centroid positions because the former is associated with surface-enhanced fluorescence, while the latter is associated with SERS.[4,30]

Figure 4A,B shows the experimental and theoretical results for the first dimer structure from Figure 2. In this case, both the calculated ε^2 and ε^4 centroids are localized near the junction of the dimer in the theoretical calculations (Figure 4B). SERS is expected to track with the ε^4 centroid, and we find excellent agreement between the location of the calculated ε^4 centroid and our placement of the SERS spatial intensity map in Figure 4A. We also note that the location of the luminescence agrees with the location of both the calculated ε^2 and ε^4 centroids. Figure 4C,D shows the results for the heterodimer structure from Figure 3. Again, the ε^4 centroid is located in the junction between the two nanoparticles and is consistent with our experimental SERS assignment. Interestingly, the calculated ε^2 centroid is shifted away from the junction and toward the larger nanoparticle, similar to the luminescence centroid in our experimental data.

In our previous work, we speculated that colocalized SERS and luminescent centroids were indicative of a single hot spot dominating both the SERS emission and the silver luminescence.[8] This hypothesis is substantiated by the DDA calculations presented in Figure 4, with one small caveat. In the case of SERS emission, the signal is strongly coupled into and emitted by the longitudinal plasmon mode, based on polarization measurements performed by our group and others.[31−33] In Figure 4A,B, the longitudinal plasmon mode is aligned with the excitation polarization, which leads to strong excitation of this mode and the calculated centroids appearing colocalized with the nanoparticle junction. This is consistent with the proposed model of a single hot spot (or plasmon mode) dominating the two measured centroids.

On the other hand, the nanoparticle shown in Figure 4C,D is excited by light polarized at 45° to the long axis of the dimer. This results in excitation of both longitudinal and transverse dipolar plasmon modes (in addition to higher order modes), which can both contribute to the calculated ε^2 and ε^4 centroids. In the case of the ε^4 centroid, the enhanced electromagnetic field of the longitudinal mode is sufficiently high that it dominates the centroid calculation when raised to the fourth power; however, in the ε^2 centroid calculation, the contribution from the transverse plasmon associated with the larger nanoparticle contributes appreciable enhancement to the calculated centroid, shifting it away from the junction. Experimentally, if the luminescence is coupled to multiple plasmon modes, then its centroid will be a weighted superposition of the different emission sites associated with these different modes, analogous to multiple molecules emitting in a single diffraction limited spot. For the data shown in Figure 4C,D, we propose that the luminescence is emitted *via* coupling to both the longitudinal and transverse plasmons in the dimer nanostructure, which shifts the measured luminescence centroid toward the leftmost nanoparticle, as observed experimentally.

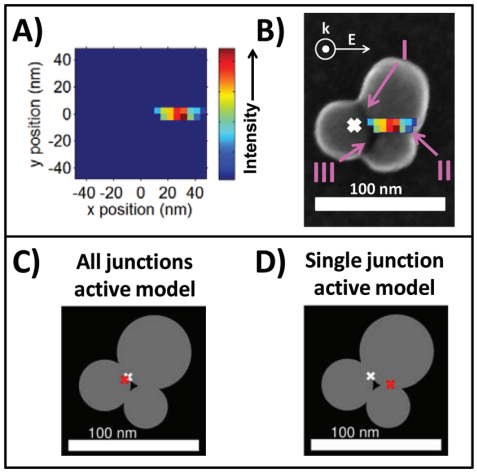

Figure 5. (A) SERS spatial intensity map with luminescence centroid arbitrarily set to (0,0). (B) Overlay of luminescence centroid (white x) and SERS spatial intensity map with SEM image of the nanoparticle structure. (C) DDA calculation of the ε^2 (white x) and ε^4 (red x) centroid positions for the modeled trimer, accounting for plasmonic enhancement over the entire structure. (D) DDA calculation of the ε^4 (red x) centroid position for the modeled trimer, accounting for plasmonic enhancement at the lower right junction only. The ε^2 (white x) centroid is the same as in (C).

Next, we present a nanoparticle trimer in Figure 5, in which the SERS and luminescent centroids are offset by more than 30 nm. Käll and co-workers have modeled a similar structure and found that all three junctions in a grouped trimer should experience enhanced electromagnetic fields capable of supporting SERS.[34] However, the spatial intensity map in Figure 5A shows only a single SERS hot spot, suggesting that only a single junction is SERS-active in the trimer. DDA calculations on this nanostructure show that the calculated ε^2 and ε^4 centroids are strongly colocalized and associated with the leftmost nanoparticle near the junction labeled I (Figure 5B,C). However, this calculation assumes that the emitter is sampling all plasmon modes across the nanoparticle trimer, and thus the centroid is a weighted superposition of these different emission sites. While we believe this to be the case for nanoparticle luminescence, SERS is expected to be a local effect in which the emission of the molecule is dominated by the hot spot in which it is located.[9,10,33,35] In this case, the geometries of junctions I and III are incongruous with the horizontal alignment of the SERS spatial intensity map, indicating that these junctions are not responsible for the measured SERS activity. Junction II not only has the proper horizontal alignment that matches with the line shape of the spatial intensity map but also results in the luminescence centroid positioned on the leftmost nanoparticle, as predicted by the DDA calculations. If we recalculate the

ε^4 centroid, assuming the molecule is only sampling the plasmon mode associated with junction II, we find excellent agreement between the spacing of the two centroids across the trimer surface (Figure 5D). These data show that SERS is emitted *via* coupling to a *local* plasmon mode, dictated by the position of the analyte molecule on the surface, while luminescence is best described by the *collective* plasmon enhancement, averaged over multiple plasmon emission sites over the entire nanoparticle structure. For this reason, it is possible for the SERS and luminescence centroids to be offset by many tens of nanometers, as we had previously speculated.[8]

To further support this idea, we present two additional examples in Figure 6, in which the SERS and luminescent centroids are offset from one another by tens of nanometers. For the trimer shown in Figure 6A, we again observe only a single SERS hot spot, despite the presence of two possible SERS-active junctions. As with the previous trimer example, we can use the luminescence centroid to assist us in assigning the SERS-active junction. Given our expectation that the luminescence centroid reports a superposition of all plasmon modes in the nanostructure, we expect the centroid position to be strongly influenced by both junctions in the trimer. In this case, junction I is "hotter" than junction II, given the polarization of the excitation light being aligned strongly with the long axis of this junction; thus, the luminescence centroid is expected to be weighted toward junction I. However, the presence of junction II will contribute some small, but significant, plasmon enhancement, biasing the luminescence centroid vertically upward. If we now look at the spatial intensity map in Figure 6A, we observe that the luminescence centroid is vertically displaced from the SERS hot spot. If we assign junction II as the SERS-active junction, the luminescence centroid would fall on the edge of the upper-most nanoparticle, which is inconsistent with plasmon-mediated emission. On the other hand, if junction I is occupied by the R6G, then the luminescence centroid falls on that same junction, just higher in the vertical direction, as expected. Thus, on the basis of our insight about the luminescence centroid, we assign junction I as the SERS-active junction in this example. Given the size and complexity of this nanostructure, it was too computationally demanding to calculate ε^2 and ε^4 centroids for a full-scale model of this aggregate. However, a rough theory calculation can be found in the Supporting Information and shows reasonable agreement with our assignment of junction I as the SERS-active junction. As with the dimer from Figure 3, the location of the luminescence centroid agrees better with the calculated ε^2 centroid.

As a final example, Figure 6B shows an asymmetric nanoparticle dimer, in which the SERS and luminescent centroids are displaced by nearly 50 nm. This example further strengthens our argument that the

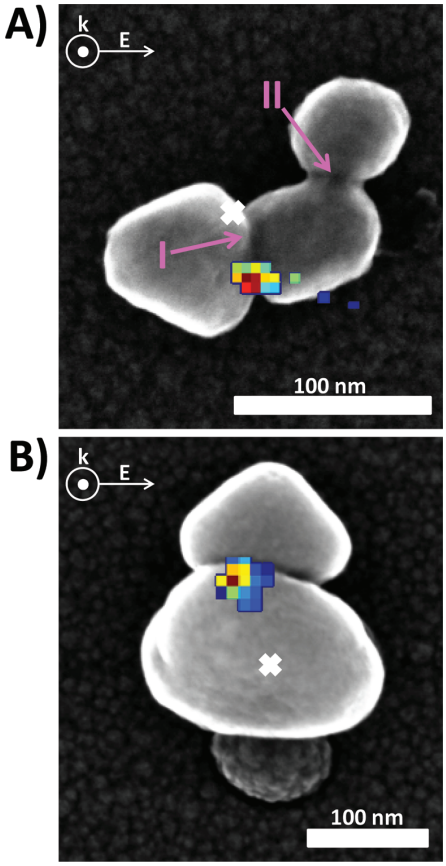

Figure 6. (A) Overlay of SERS spatial intensity map and luminescent centroid (white x) on the SEM structure of a trimer. (B) Overlay of SERS spatial intensity map and luminescent centroid (white x) on the SEM structure of a vertically oriented asymmetric dimer.

luminescence is not dominated by the "hot spot" in the nanostructure, but rather reports on a weighted superposition of all actively excited plasmon modes. If we position the SERS data such that it is near the junction between the two particles, the luminescence centroid clearly favors the much larger nanoparticle on the bottom (the lowest dark sphere is believed to be substrate material or some other nonplasmonic contaminant). For the SERS, the emission strongly couples to the junction-associated longitudinal plasmon mode, even though this mode is inefficiently excited by the horizontally polarized light.[33] On the other hand, the nanostructure is expected to support both longitudinal and transverse plasmon modes, both of which can couple to the luminescence. For a vertically oriented dimer excited with horizontally polarized light, little electromagnetic field enhancement would be expected in the junction.[2] Consequently, the transverse dipolar and multipolar plasmon modes will have a much stronger impact on the overall plasmonic enhancement of the nanoparticle.[2] In this case, we

predict that the transverse plasmon associated with the larger nanoparticle couples more strongly with the 532 nm excitation light, shifting the luminescence centroid toward the lower nanoparticle. The effect of the contaminant dielectric sphere in contact with the lower nanoparticle may also impact the plasmon modes of the aggregate, although this is more challenging to describe, given the uncertainty of its size and composition.

One challenge with SEM structural characterization is the loss of three-dimensional information about the exact geometry of the gap structure. In this case, the larger nanoparticle has curvature that extends over the lower edge of the triangular nanoparticle, obscuring the junction. This missing geometric information about the junction may help explain why strong SERS is observed from this nanostructure, even though the junction appears oriented parallel to the excitation light.

Notably, in several of our examples, the calculated ε^2 centroid agrees better than the ε^4 centroid with the experimentally determined luminescence centroid. One question that remains open is why nanoparticle luminescence would be an ε^2 process. Typical nanoparticle plasmon-mediated ε^2 processes include Rayleigh scattering and surface-enhanced fluorescence. In the case of the former, the scattering intensity depends on the polarizability of the nanostructure, which leads to the ε^2 dependence.[29,36] In the latter case, the intensity of the excitation field is enhanced (ε^2) but the emission is dominated by changes in the radiative rate due to the presence of the metal nanoparticle.[36−39] In the case of luminescence, we speculate that the excitation field is enhanced (ε^2), but that the emission does not experience a similar enhancement. As evidence that the excitation field is enhanced, we have observed that the intensity of the luminescence depends on the polarization of the excitation light, which is expected in the case of a plasmon-mediated excitation process.[26,40] On the other hand, we do not observe any overlap between the broad silver luminescence and the measured plasmon resonance spectra for the aggregates, indicating that the two processes are not intimately related; this is in stark contrast to gold luminescence, in which the emission spectrum mirrors the plasmon resonance spectrum in gold nanorod structures.[41]

To understand this in more detail, it is worth considering the possible origins of the luminescence signal in colloidal silver nanoparticles. Although the existence of the signal is widely accepted by researchers, the responsible mechanism remains a subject of debate.[42−46] Current hypotheses in the literature propose that luminescence is due to interband transitions, fluorescence of chemi- or physisorbed molecules on silver colloids, or small fluorescent clusters of silver atoms on the surface of larger colloids.[42,44−52] In addition to these mechanisms, we must also consider the possibility of electronic Raman scattering from "dirty" silver nanoparticles, as described by Brus and others.[53−55] We rule out the first two mechanisms as follows: first, the interband transition in silver is toward the ultraviolet and is not expected to be resonant with our 532 nm excitation light, suggesting that direct excitation of silver is not the responsible mechanism.[41,56] Second, fluorescence from adsorbed molecules is also unlikely, as we and others have observed luminescence in the absence of fluorescent dye molecules on the nanoparticles.[8,43] In the odd case of carbon contamination on the nanoparticle surface, we observe the appearance of sharp Raman bands rather than a broad, stable luminescence, suggesting that adsorbed molecules would produce strong SERS rather than luminescence if they were, in fact, resonant with our excitation light.[57]

The hypothesis that luminescence is caused by small clusters of silver atoms on the surface of the larger metal colloids remains a well-accepted mechanism to describe the photoluminescence background.[42,48,49] Recent reports in the literature have shown successful syntheses of isolated silver atom clusters (2−39 atoms) that are strongly photoluminescent, supporting the idea that small silver clusters on the nanoparticle surface could be responsible for the observed photoluminescence.[58−60] Work from Dickson and co-workers on Ag|Ag_2O films observed the formation of luminescent spots upon photoactivation,[50] while more recent work from Lupton and co-workers has shown similar behavior on the surface of silver island films;[49] in both cases, the luminescence was assigned to the formation of silver clusters on the film surface. A recent report from Wang and Palmer used aberration-corrected scanning transmission electron microscopy to show that so-called "magic number" gold nanoparticles are covered with single gold adatoms as well as gold adatom clusters, indicating that even in closed shell systems, the surface can be defected, rather than atomically smooth.[61] Although a similar study has not been done for silver nanoparticles, this study supports the idea that silver adatom clusters should be stable on the surface of larger nanoparticles. Here, we speculate that small, several-atom clusters could form spontaneously on the surface of the silver nanoparticles and produce the observed luminescence. Given that the nanoparticles are prepared in ambient air and not protected from oxygen, the photoreduction of surface silver oxides may play a role, as suggested by Dickson and co-workers.[50,51] Questions that remain are (1) why the luminescence emission from these clusters would not couple to the nanoparticle plasmons, leading to ε^4 enhancement, and (2) why the clusters would behave as entities independent from the "bulk" metal surface, to which they are in intimate contact.

The final mechanism involves electronic Raman excitation of silver, catalyzed by defect sites on the nanoparticle surface.[62] Brus *et al.* explained the presence of

the well-known continuum background that accompanies single-molecule SERS by characterizing the Raman analyte as a defect site that couples to the bulk silver and scatters with an ε^2 dependence, consistent with our data. In their work, they found that this continuum was only observed when the R6G molecule was present, acting as a defect site, due to the highly crystalline surfaces on their as-prepared nanoparticles. However, if our nanoparticles have surface defects, such as the clusters described above, we could expect these clusters to act as nucleation sites for electronic Raman scattering. This type of behavior was also reported for silver films and small silver clusters in the absence of adsorbed dyes.[62−64]

While we cannot rigorously prove the origin of the luminescence background in our samples, our results are consistent with the models of both luminescent clusters and surface defect-mediated electronic Raman excitation of the silver metal.[42,46,48,49] More investigation is needed to understand this phenomenon, but our results demonstrate that the luminescence is clearly linked to the collective excitation of plasmons within the silver nanoparticle aggregates, with the centroid reporting on a weighted superposition of different plasmon-mediated emission sites. Perhaps more important is the fact that the luminescence centroid location allows us to assign the SERS-active junction in the case of higher-order aggregates (*e.g.*, trimers, tetramers, *etc.*) by using theoretical calculations of plasmonic enhancement distributed over the entire nanoparticle structure (as in Figures 5 and 6). This is of critical importance as we continue to develop super-resolution imaging as a tool for studying SERS substrates, especially at the single- or few-molecule level.

CONCLUSIONS

In conclusion, we have shown that the offset between the luminescence and SERS centroids can be explained by different coupling mechanisms between each emission process and the plasmonic enhancement provided by the nanoparticle. In the case of SERS, the emission couples into a local plasmon mode, dictated by the position of the molecule on the nanoparticle surface, while the plasmon-mediated silver luminescence is coupled into all active plasmon modes in the nanoparticle structure. These different mechanisms lead to an offset between the SERS and luminescence centroids in our super-resolution imaging data when nanoparticles support more than one dominant plasmon mode. Our results also suggest that the luminescence is enhanced *via* an ε^2 mechanism, although further work is needed to rigorously prove this and explain the mechanism behind it.

METHODS

SERS samples are prepared using citrate-reduced silver colloids synthesized *via* the Lee and Meisel method.[20] A 2 mL aliquot of these as-prepared colloids is incubated with R6G dye (1 nM final concentration) and aqueous sodium bromide (9.52 mM final concentration) for 1 h. After incubation, 4 μL of this solution and a small amount of Spherotech Blue Sky fluorescent marker beads used for alignment purposes are drop-cast onto an ITO-coated glass coverslip that has been patterned with an aluminum alphanumeric grid, as described in previous work, to facilitate correlated studies.[9]

Samples are first analyzed optically using an inverted Olympus IX-71 microscope with linear-polarized 532 nm laser excitation in epi-illumination. After passing through a 550 nm longpass filter to block Rayleigh scattered laser light, the resulting emission is split with a 50/50 beamsplitter that sends half of the signal to a Princeton Instruments ProEM 512 electron-multiplying charge-coupled device (CCD) camera for SERS imaging, while the other half is dispersed by a PI ACTON SpectraPro 2500i spectrograph coupled to a Spec-10 camera for spectral acquisition. The SERS images consist of photons with wavelengths longer than 550 nm, allowing us to collect both luminescence and SERS signals with a single detector. The wavelength overlap between the two signals at 532 nm excitation precludes separation of the two signals into separate spectral domains. Each CCD pixel corresponds to 46 nm in the sample, calibrated using a USAF test target. Correlated structural data are collected using a high-resolution Hitachi S-5500 SEM (30 kV accelerating voltage). Complete sample preparation and experimental details are provided in the Supporting Information.

Acknowledgment. We thank Spherotech for the generous gift of fluorescent nanospheres used as alignment markers. We also thank the National Science Foundation (Grant No. 0821312) for funding the Hitachi S-5500 scanning electron microscope/scanning transmission electron microscope used in this work, and Texas Materials Institute for supporting this facility. This material is based on work supported by the Welch Foundation under Award No. F-1699 (K.A.W.), the Air Force Office of Scientific Research under AFOSR Award No. FA9550-09-0112 (K.A.W.), the National Science Foundation Graduate Research Fellowship under Grant No. DGE-0718124 (J.P.L.), and the University of Washington Royalty Research Fund (D.J.M.).

Supporting Information Available: Experimental details, SEM images of aggregates without overlays and their associated spectral and intensity timetrace data, super-resolution fitting technique details, scatter plots for luminescence centroid data, sample resolution calculation for Figure 2B luminescence and SERS data, and the DDA result for the aggregate in Figure 6A. This material is available free of charge *via* the Internet at http://pubs.acs.org.

Conflict of Interest: The authors declare no competing financial interest.

REFERENCES AND NOTES

1. Wustholz, K. L.; Henry, A.-I.; McMahon, J. M.; Freeman, R. G.; Valley, N.; Piotti, M. E.; Natan, M. J.; Schatz, G. C.; Van Duyne, R. P. Structure−Activity Relationships in Gold Nanoparticle Dimers and Trimers for Surface-Enhanced Raman Spectroscopy. *J. Am. Chem. Soc.* **2010**, *132*, 10903–10910.
2. Oubre, C.; Nordlander, P. Finite-Difference Time-Domain Studies of the Optical Properties of Nanoshell Dimers. *J. Phys. Chem. B* **2005**, *109*, 10042–10051.
3. Mcmahon, J. M.; Henry, A.-I.; Wustholz, K. L.; Natan, M. J.; Freeman, R. G.; Van Duyne, R. P.; Schatz, G. C. Gold Nanoparticle Dimer Plasmonics: Finite Element Method Calculations of the Electromagnetic Enhancement to Surface-Enhanced Raman Spectroscopy. *Anal. Bioanal. Chem.* **2009**, *394*, 1819–1825.

4. Hao, E.; Schatz, G. C. Electromagnetic Fields around Silver Nanoparticles and Dimers. *J. Chem. Phys.* **2004**, *120*, 357–366.
5. Camden, J. P.; Dieringer, J. A.; Wang, Y.; Masiello, D. J.; Marks, L. D.; Schatz, G. C.; Van Duyne, R. P. Probing the Structure of Single-Molecule Surface-Enhanced Raman Scattering Hot Spots. *J. Am. Chem. Soc.* **2008**, *130*, 12616–12617.
6. Michaels, A. M.; Nirmal, M.; Brus, L. E. Enhanced Raman Spectroscopy of Individual Rhodamine 6G Molecules on Large Ag Nanocrystals. *J. Am. Chem. Soc.* **1999**, *121*, 9932–9939.
7. Michaels, A. M.; Jiang, J.; Brus, L. Ag Nanocrystal Junctions as the Site for Surface-Enhanced Raman Scattering of Single Rhodamine 6G Molecules. *J. Phys. Chem. B* **2000**, *104*, 11965–11971.
8. Stranahan, S. M.; Willets, K. A. Super-Resolution Optical Imaging of Single-Molecule SERS Hot Spots. *Nano Lett.* **2010**, *10*, 3777–3784.
9. Weber, M. L.; Willets, K. A. Correlated Super-Resolution Optical and Structural Studies of Surface-Enhanced Raman Scattering Hot Spots in Silver Colloid Aggregates. *J. Phys. Chem. Lett.* **2011**, *2*, 1766–1770.
10. Cang, H.; Labno, A.; Lu, C.; Yin, X.; Liu, M.; Gladden, C.; Liu, Y.; Zhang, X. Probing the Electromagnetic Field of a 15-Nanometre Hotspot by Single Molecule Imaging. *Nature* **2011**, *469*, 385–388.
11. Henglein, A.; Giersig, M. Formation of Colloidal Silver Nanoparticles: Capping Action of Citrate. *J. Phys. Chem. B* **1999**, *103*, 9533–9539.
12. Kerker, M.; Siiman, O.; Bumm, L. A.; Wang, D. S. Surface Enhanced Raman Scattering (SERS) of Citrate Ion Adsorbed on Colloidal Silver. *Appl. Opt.* **1980**, *19*, 3253–3255.
13. Munro, C. H.; Smith, W. E.; Garner, M.; Clarkson, J.; White, P. C. Characterization of the Surface of a Citrate-Reduced Colloid Optimized for Use as a Substrate for Surface-Enhanced Resonance Raman Scattering. *Langmuir* **1995**, *11*, 3712–3720.
14. Sirimuthu, N. M. S.; Bell, S. E. J. Surface-Enhanced Raman Spectroscopy as a Probe of Competitive Binding by Anions to Citrate-Reduced Silver Colloids. *J. Phys. Chem. A* **2005**, *109*, 7405–7410.
15. Ciou, S.-H.; Cao, Y.-W.; Huang, H.-C.; Su, D.-Y.; Huang, C.-L. SERS Enhancement Factors Studies of Silver Nanoprism and Spherical Nanoparticle Colloids in the Presence of Bromide Ions. *J. Phys. Chem. C* **2009**, *113*, 9520–9525.
16. Draine, B. T.; Flatau, P. J. Discrete-Dipole Approximation for Scattering Calculations. *J. Opt. Soc. Am. A* **1994**, *11*, 1491–1499.
17. Cheezum, M. K.; Walker, W. F.; Guilford, W. H. Quantitative Comparison of Algorithms for Tracking Single Fluorescent Particles. *Biophys. J.* **2001**, *81*, 2378–2388.
18. Yildiz, A.; Forkey, J. N.; McKinney, S. A.; Ha, T.; Goldman, Y. E.; Selvin, P. R. Myosin V Walks Hand-over-Hand: Single Fluorophore Imaging with 1.5-nm Localization. *Science* **2003**, *300*, 2061–2065.
19. Yildiz, A.; Selvin, P. R. Fluorescence Imaging with One Nanometer Accuracy: Application to Molecular Motors. *Acc. Chem. Res.* **2005**, *38*, 574–582.
20. Lee, P. C.; Meisel, D. Adsorption and Surface-Enhanced Raman of Dyes on Silver and Gold Sols. *J. Phys. Chem.* **1982**, *86*, 3391–3395.
21. Le Ru, E. C.; Meyer, M.; Etchegoin, P. G. Proof of Single-Molecule Sensitivity in Surface Enhanced Raman Scattering (SERS) by Means of a Two-Analyte Technique. *J. Phys. Chem. B* **2006**, *110*, 1944–1948.
22. Kneipp, K.; Wang, Y.; Dasari, R. R.; Feld, M. S. Single Molecule Detection Using Surface-Enhanced Resonance Raman Scattering (SERRS): A Study Using Rhodamine 6G on Colloidal Silver. *Appl. Spectrosc.* **1995**, *49*, 780–784.
23. Dieringer, J. A.; Lettan, R. B., II; Scheidt, K. A.; Van Duyne, R. P. A Frequency Domain Existence Proof of Single-Molecule Surface-Enhanced Raman Spectroscopy. *J. Am. Chem. Soc.* **2007**, *129*, 16249–16256.
24. Talley, C. E.; Jackson, J. B.; Oubre, C.; Grady, N. K.; Hollars, C. W.; Lane, S. M.; Huser, T. R.; Nordlander, P.; Halas, N. J. Surface-Enhanced Raman Scattering from Individual Au Nanoparticles and Nanoparticle Dimer Substrates. *Nano Lett.* **2005**, *5*, 1569–1574.
25. Ausman, L. K.; Schatz, G. C. On the Importance of Incorporating Dipole Reradiation in the Modeling of Surface-Enhanced Raman Scattering from Spheres. *J. Chem. Phys.* **2009**, *131*, 084708/1–084707/10.
26. Xu, H.; Kall, M. Polarization-Dependent Surface-Enhanced Raman Spectroscopy of Isolated Silver Nanoaggregates. *Chem. Phys. Chem.* **2003**, *4*, 1001–1005.
27. Yoshida, K.-i.; Itoh, T.; Tamaru, H.; Biju, V.; Ishikawa, M.; Ozaki, Y. Quantitative Evaluations of Electromagnetic Enhancement in Surface-Enhanced Resonance Raman Scattering from Plasmonic Properties and Morphologies of Individual Ag Nanostructures. *Phys. Rev. B* **2010**, *81*, 115406/1-9.
28. Yang, W.-H.; Schatz, G. C.; Van Duyne, R. P. Discrete Dipole Approximation for Calculating Extinction and Raman Intensities for Small Particles with Arbitrary Shapes. *J. Chem. Phys.* **1995**, *103*, 869–875.
29. Kelly, K. L.; Coronado, E.; Zhao, L. L.; Schatz, G. C. The Optical Properties of Metal Nanoparticles: The Influence of Size, Shape, and Dielectric Environment. *J. Phys. Chem. B* **2003**, *107*, 668–677.
30. Le Ru, E. C.; Etchegoin, P. G. Rigorous Justification of the $|E|^4$ Enhancement Factor in Surface Enhanced Raman Spectroscopy. *Chem. Phys. Lett.* **2006**, *243*, 63–66.
31. Stranahan, S. M.; Titues, E. J.; Willets, K. A. SERS Orientational Imaging of Silver Nanoparticle Dimers. *J. Phys. Chem. Lett.* **2011**, *2*, 2711–2715.
32. Li, Z.; Shegai, T.; Haran, G.; Xu, H. Multiple-Particle Nanoantennas for Enormous Enhancement and Polarization Control of Light Emission. *ACS Nano* **2009**, *3*, 637–642.
33. Shegai, T.; Li, Z.; Dadosh, T.; Zhang, Z.; Xu, H.; Haran, G. Managing Light Polarization *via* Plasmon–Molecule Interactions within an Asymmetric Metal Nanoparticle Trimer. *Proc. Natl. Acad. Sci. U.S.A.* **2008**, *105*, 16448–16453.
34. Kall, M.; Xu, H.; Johansson, P. Field Enhancement and Molecular Response in Surface-Enhanced Raman Scattering and Fluorescence Spectroscopy. *J. Raman Spectrosc.* **2005**, *36*, 510–514.
35. Litz, J. P.; Camden, J. P.; Masiello, D. J. Spatial, Spectral, and Coherence Mapping of Single-Molecule SERS Active Hot Spots *via* the Discrete-Dipole Approximation. *J. Phys. Chem. Lett.* **2011**, *2*, 1695–1700.
36. Bosnick, K. A.; Jiang, J.; Brus, L. E. Fluctuations and Local Symmetry in Single-Molecule Rhodamine 6G Raman Scattering on Silver Nanocrystal Aggregates. *J. Phys. Chem. B* **2002**, *106*, 8096–8099.
37. Johansson, P.; Xu, H.; Kall, M. Surface-Enhanced Raman Scattering and Fluorescence near Metal Nanoparticles. *Phys. Rev. B* **2005**, *72*, 035427\1–17.
38. Fort, E.; Gresillon, S. Surface Enhanced Fluorescence. *J. Phys. D: Appl. Phys.* **2007**, *41*, 1–31.
39. Lakowicz, J. R. Radiative Decay Engineering 5: Metal-Enhanced Fluorescence and Plasmon Emission. *Anal. Biochem.* **2005**, *337*, 171–194.
40. McLellan, J. M.; Li, Z.-Y.; Siekkinen, A. R.; Xia, Y. The SERS Activity of a Supported Ag Nanocube Strongly Depends on Its Orientation Relative to Laser Polarization. *Nano Lett.* **2007**, *7*, 1013–1017.
41. Mohamed, M. B.; Volkov, V.; Link, S.; El-Sayed, M. A. The "Lightning" Gold Nanorods: Fluorescence Enhancement of over a Million Compared to the Gold Metal. *Chem. Phys. Lett.* **2000**, *317*, 517–523.
42. Geddes, C. D.; Parfenov, A.; Gryczynski, I.; Lakowicz, J. R. Luminescent Blinking from Silver Nanostructures. *J. Phys. Chem. B* **2003**, *107*, 9989–9993.
43. Andersen, P. C.; Jacobson, M. L.; Rowlen, K. L. Flashy Silver Nanoparticles. *J. Phys. Chem. B* **2004**, *108*, 2148–2153.
44. Boyd, G. T.; Yu, Z. H.; Shen, Y. R. Photoinduced Luminescence from the Noble Metals and Its Enhancement on Roughened Surfaces. *Phys. Rev. B* **1986**, *33*, 7923–7936.
45. Yeshchenko, O. A.; Dmitruk, I. M.; Alexeenko, A. A.; Losytskyy, M. Y.; Kotko, A. V.; Pinchuk, A. O. Size-Dependent

Surface-Plasmon-Enhanced Photoluminescence from Silver Nanoparticles Embedded in Silica. *Phys. Rev. B* **2009**, *79*, 235438\1-8.
46. Zhang, A.; Zhang, J.; Fang, Y. Photoluminescence from Colloidal Silver Nanoparticles. *J. Lumin.* **2008**, *128*, 1635–1640.
47. Itoh, T.; Kikkawa, Y.; Biju, V.; Ishikawa, M.; Ikehata, A.; Ozaki, Y. Steady-State and Time-Resolved Background Luminescence from Surface-Enhanced Resonance Raman Scattering-Active Single Ag Nanoaggregates. *J. Phys. Chem. B* **2006**, *110*, 21536–21544.
48. Harb, M.; Rabilloud, F.; Simon, D.; Rydlo, A.; Lecoultre, S.; Conus, F.; Rodrigues, V.; Felix, C. Optical Absorption of Small Silver Clusters: Ag_n, (n=4−22). *J. Chem. Phys.* **2008**, *129*, 194108\1-9.
49. Borys, N. J.; Lupton, J. M. Surface-Enhanced Light Emission from Single Hot Spots in Tollens Reaction Silver Nanoparticle Films: Linear *versus* Nonlinear Optical Excitation. *J. Phys. Chem. C* **2011**, *115*, 13645–13659.
50. Peyser, L. A.; Vinson, A. E.; Bartko, A. P.; Dickson, R. M. Photoactivated Fluorescence from Individual Silver Nanoclusters. *Science* **2001**, *291*, 103–106.
51. Peyser, L. A.; Lee, T.-H.; Dickson, R. M. Mechanism of Ag_n Nanocluster Photoproduction from Silver Oxide Films. *J. Phys. Chem. B* **2002**, *106*, 7725–7728.
52. Lee, T.-H.; Gonzalez, J. I.; Dickson, R. M. Strongly Enhanced Field-Dependent Single-Molecule Electroluminescence. *Proc. Natl. Acad. Sci. U.S.A.* **2002**, *99*, 10272–10275.
53. Jiang, J.; Bosnick, K.; Maillard, M.; Brus, L. Single Molecule Raman Spectroscopy at the Junctions of Large Ag Nanocrystals. *J. Phys. Chem. B* **2003**, *107*, 9964–9972.
54. Itai, K. Theory of Raman Scattering in Coupled Electron-Phonon Systems. *Phys. Rev. B* **1992**, *45*, 707–717.
55. Zawadowski, A.; Cardona, M. Theory of Raman Scattering on Normal Metals with Impurities. *Phys. Rev. B* **1990**, *42*, 10732–10734.
56. Geddes, C. D.; Parfenov, A.; Gryczynski, I.; Lakowicz, J. R. Luminescent Blinking of Gold Nanoparticles. *Chem. Phys. Lett.* **2003**, *380*, 269–272.
57. Norrod, K. L.; Rowlen, K. L. Removal of Carbonaceous Contamination from SERS-Active Silver by Self-Assembly of Decanethiol. *Anal. Chem.* **1998**, *70*, 4218–4221.
58. Cui, Y.; Wang, W.; Liu, R.; Sun, Z.; Wei, Y.; Zhao, Y.; Gao, X. Serial Silver Clusters Biomineralized by One Peptide. *ACS Nano* **2011**, *5*, 8684–8689.
59. Petty, J. T.; Story, S. P.; Juarez, S.; Votto, S. S.; Herbst, A. G.; Degtyareva, N. N.; Sengupta, B. Optical Sensing by Transforming Chromophoric Silver Clusters in DNA Nanoreactors. *Anal. Chem.* **2012**, *84*, 356–364.
60. Diez, I.; Ras, R. H. A. Fluorescent Silver Nanoclusters. *Nanoscale* **2011**, *3*, 1963–1970.
61. Wang, Z.; Palmer, R. E. Mass Spectrometry and Dynamics of Gold Adatoms Observed on the Surface of Size-Selected Au Nanoclusters. *Nano Lett.* **2012**, *12*, 91–95.
62. Gass, A. N.; Kapusta, O. I.; Klimin, S. A.; Mal'shukov, A. G. The Nature of the Inelastic Background in Surface Enhanced Raman Scattering Spectra of Coldy-Deposited Silver Films. The Role of Active Sites. *Solid State Commun.* **1989**, *71*, 749–753.
63. Portales, H.; Duval, E.; Saviot, L.; Fujii, M.; Sumitomo, M.; Hayashi, S. Raman Scattering by Electron−Hole Excitations in Silver Nanocrystals. *Phys. Rev. B* **2001**, *63*, 233402\1-4.
64. Otto, A. Theory of First Layer and Single Molecule Surface Enhanced Raman Scattering (SERS). *Phys. Status Solidi A* **2001**, *188*, 1455–1470.

Supporting Information for "Super-Resolution Imaging Reveals a Difference between SERS and Luminescence Centroids"

Maggie L. Weber, Jonathan P. Litz, David J. Masiello, Katherine A. Willets*

SERS Solution Preparation

Silver nanoparticles are synthesized via the method developed by Lee and Meisel.[1] SERS samples are prepared using 2 mL of the aqueous colloids to which is added 200 μL of 21 nM Rhodamine 6G (R6G) dye in methanol and 2 mL of 20 mM aqueous sodium bromide. The solution is vortexed for 60 seconds and then incubated for one hour.

Substrate Preparation

As previously reported, aluminum metal is deposited through an alphanumeric TEM grid (Ted Pella, Inc.) which acts as a shadow mask on the surface of an indium tin oxide-coated glass coverslip (15-30 nm ITO on 0.17 mm borosilicate glass, SPI Supplies)[2]. After deposition, the coverslips are placed in an Oxford RF plasma cleaner and exposed to atmosphere for 10 minutes, which increases the hydrophilicity of the surface, allowing more uniform sample drying.

SERS Sample Deposition

After the SERS sample has incubated for one hour, 4 μL are dropcast onto the gridded area of the ITO coverslip and dried under a stream of nitrogen. Once dry, the coverslip is then washed with nanopure water to remove any crystals of sodium bromide on the surface and is dried again under nitrogen. Finally, 1 μL of 500x diluted Spherotech Blue Sky fluorescent polystyrene beads (0.5 μm diameter) is dropcast and dried on the coverslip. These beads are used to correct for stage drift in CCD movies prior to super resolution analysis and are also used to match angular position when the sample is transferred between the optical and electron microscopes.

SEM Images of Aggregates in Article and Associated Intensity Time Traces

The following figure contains the original SEM images collected for all aggregates in the Article. These are provided so the junction regions and particle surface can be viewed entirely without the spatial intensity overlays. The associated intensity time traces and selected spectral data are shown so that the on/off behavior of the SERS can be confirmed. Intensity thresholds are determined using a complete series of spectral data, as described in the main text.

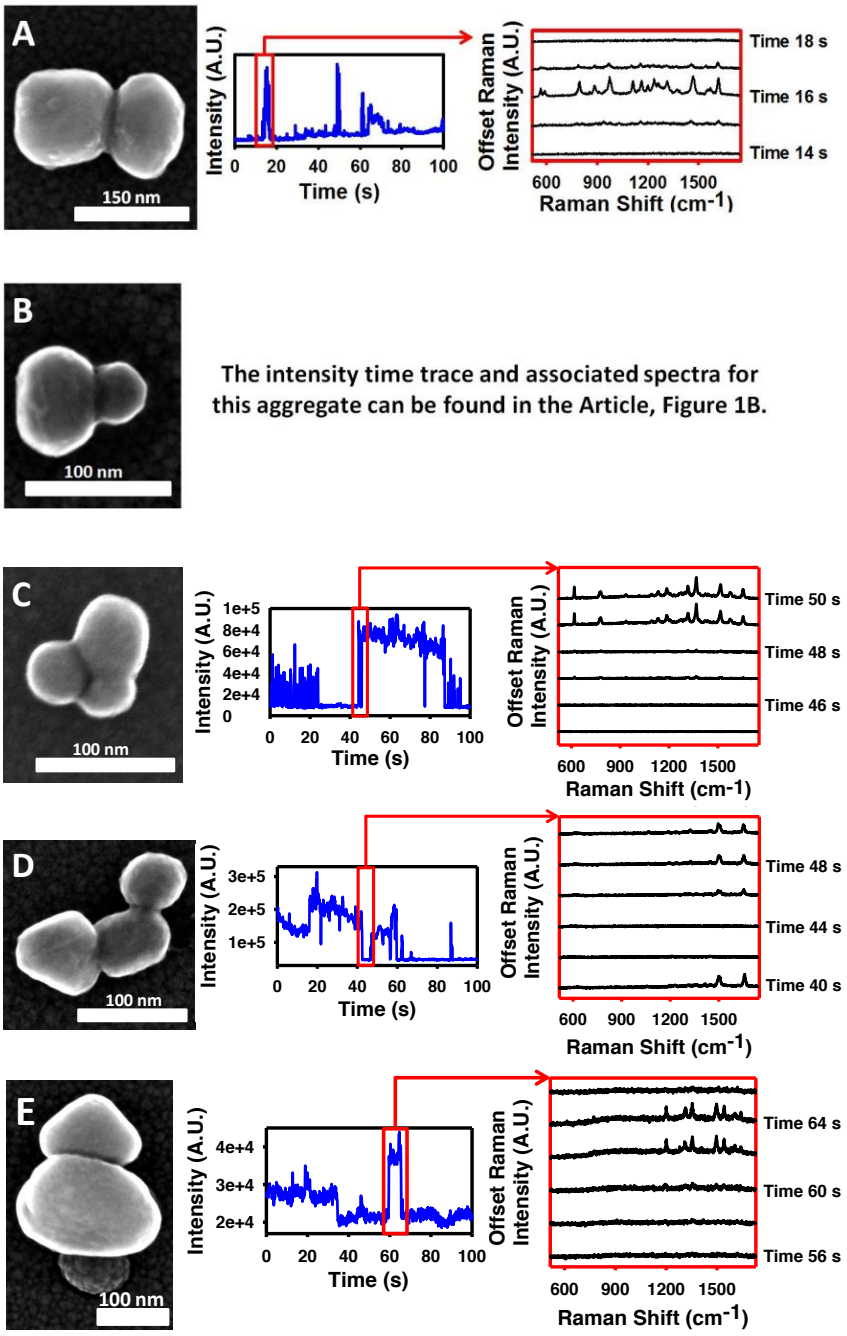

Figure S-1: SEM images and associated intensity time traces and selected spectra data corresponding to the following figures from the main manuscript: A) Figure 2B, B) Figure 3B, C) Figure 5B, D) Figure 6A, E) Figure 6B.

Super Resolution Imaging Through Point Spread Function Fitting

As described previously, point spread function fitting (PSF) is used to isolate and track the position of the SERS and luminescence signals[3]. To clarify, we will walk through the entire process for the dimer shown in Figure 2 in the Article. Spectra are collected using a 1200 groove/mm grating in the PI ACTON SpectraPro 2500i spectrograph. This data is used to confirm which simultaneously collected CCD images will represent R6G SERS and luminescence emission or simply luminescence emission. For a specific region of interest (ROI) in the CCD images, we integrate the total intensity and plot it as a function of time (Figure S-2A). We then set a threshold for the data where every frame whose intensity is below the threshold will be designated as nanoparticle luminescence and everything above will be luminescence and R6G SERS.

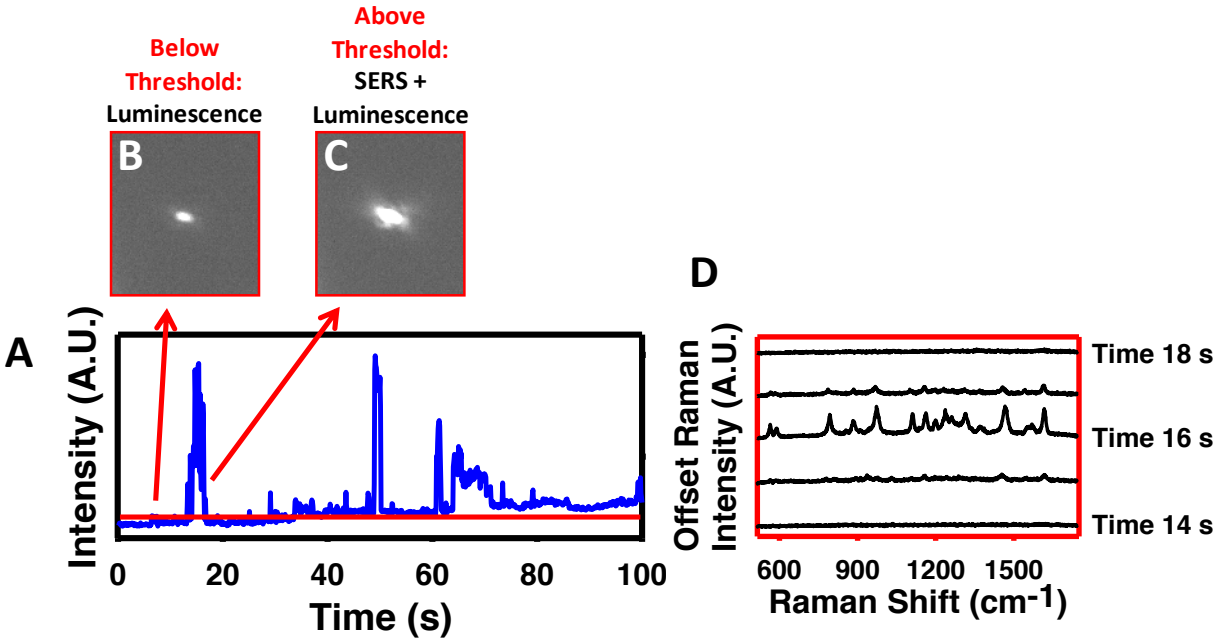

Figure S-2: A) Intensity Time Trace for Square Dimer. B) Diffraction-limited CCD image of luminescent aggregate. C) CCD image of same luminescent aggregate with SERS emission from one or more R6G molecules. D) Correlated spectra for CCD images shown in B and C.

This threshold allows us to independently track the emission from the metal nanoparticles (luminescence) and the emission from R6G molecules probing an aggregate's surface. The threshold is set as close as possible to the background signal to prevent any SERS from biasing the position of the luminescence (fitting process to be described later). This is confirmed by comparing the intensity time trace with the spectral data to confirm that no SERS peaks are evident for frames whose intensity is below the threshold. Figure S-2B was collected at approximately 14 seconds when no R6G peaks were evident in the spectral data and is

designated as luminescence emission. Figure S-2C was collected at approximately 16 seconds when one or more R6G molecules were emitting and is designated as luminescence with SERS emission. Note that the optical images shown have a slight ellipticity; this is due, in part, to the beamsplitter used to split the signal between the spectrometer and the imaging CCD, as well as to the highly polarized emission which originates from a nanoparticle dimer, as described in detail elsewhere.[4]

After the threshold has been drawn, the emission pattern for each frame whose intensity falls below the threshold is fit to a single 2-dimensional Gaussian as defined:

$$I(x,y) = z_0 + I_0 e^{\left[-\frac{1}{2}\left[\left(\frac{x-x_0}{s_x}\right)^2+\left(\frac{y-y_0}{s_y}\right)^2\right]\right]} \qquad \text{(S-1)}$$

where I is the intensity for a given position (x,y) in space, z_0 is the background intensity, I_0 is the intensity at the center of the fit, $s_{x,y}$ are the standard deviations for x and y, respectively, and x_0 and y_0 are the centroid of the fit. We have six adjustable parameters in our fits—z_0, I_0, x_0, y_0, s_x, and s_y—and we fit each diffraction limited spot to equation S-1 using nonlinear least squares by minimizing by the standard error of the fit using homewritten Matlab code. This fitting process will produce a collection of emission centroid positions for all frames designated as "luminescence emission." This data can be plotted to determine the average position for the luminescence centroid throughout the course of an experiment as shown in Figure S-3A.

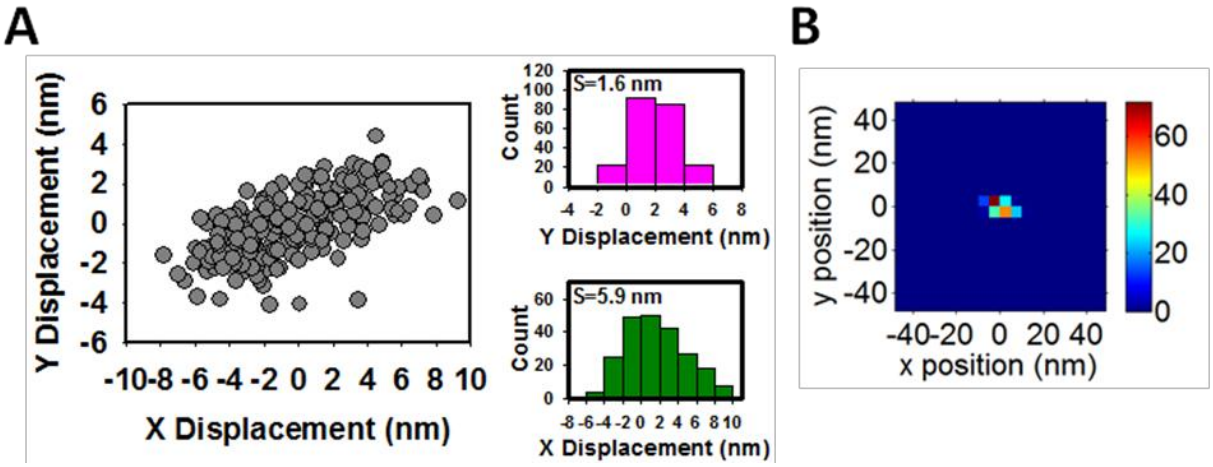

Figure S-3: (A, left) Scatter plot showing the luminescence centroid positions for the square dimer aggregate from Figure 2B. (0,0) represents the mean position of all luminescence centroids. (A, right) Histograms showing the centroid displacement from the mean in both the x (green) and y (pink) directions. (B) Two-dimensional histogram, showing that the frequency with which a particular x_0, y_0 location is fit. (This histogram contains a vertical reflection of the data in the scatter plot) Note that the elliptical shape observed in the scatter plot is due to low probability events and the bulk of the emission originates from a well-defined region.

Histograms for the scatter plot data are shown in Figure S-3A (right) and S-3B, and show that most of the centroid data are clustered around some mean position, arbitrarily defined as (0, 0). The slight ellipticity is most likely due to low single SERS events that bias the centroid towards the origin of the SERS, as we have previously reported.[2] Once the average position of the

luminescence is determined, the point spread function of the luminescence contribution can be subtracted from the raw image data for all frames above our intensity threshold, which is the superposition of the luminescence and SERS emission. The remaining signal will be only due to SERS emission and can also be fit to the same Gaussian equation listed previously (Equation S-1). The centroid data extracted from the fit can be plotted as a scatter plot as shown in Figure S-4.

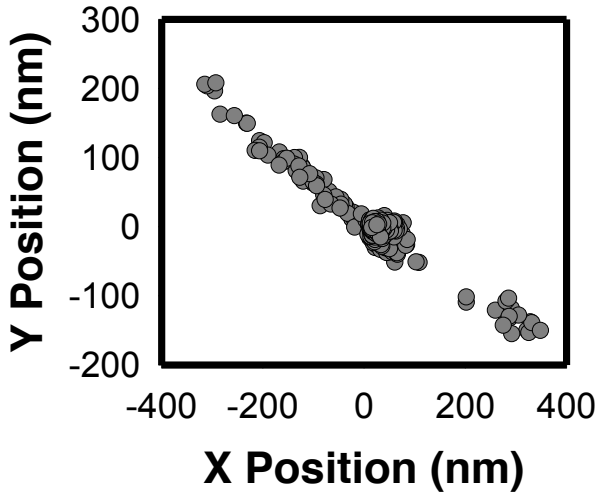

Figure S-4: SERS centroid data distributed about luminescence centroid mean (0,0).

Although this can give us some information, the centroid overlap makes it difficult to know where most of the events are occurring and their relative intensity. To counter this issue, we can bin the data in 4.6 nm bins to calculate the frequency with which a particular centroid position is fit (as in Figure S-3B). From there, we calculate the mean intensity of all points that fall within a given bin to construct the spatial intensity maps shown in the manuscript. (Note: only Gaussian fits that have an R^2 value greater than or equal to 0.8 are included in this binned data.) The spatial intensity map for the data in Figure S-4 can be found in the Article in Figure 2A.

One other important detail to note is that the point spread functions of at least 3 or more fluorescent marker beads are also fit to two-dimensional Gaussians to extract their centroid positions. These centroid positions are calculated for all 1000 frames of a CCD movie and are used to correct for drift in the microscope stage. Both the luminescence and SERS centroid positions are corrected using this fluorescent bead data. This point spread function fitting technique allows us to track various emission signals as a function of time and space to an accuracy of +/- 5 nm, a significant improvement over the optical resolution of ~250 nm.

The following figure contains the luminescence centroid scatter plots and histograms with associated standard deviation for all the aggregates found in the Article.

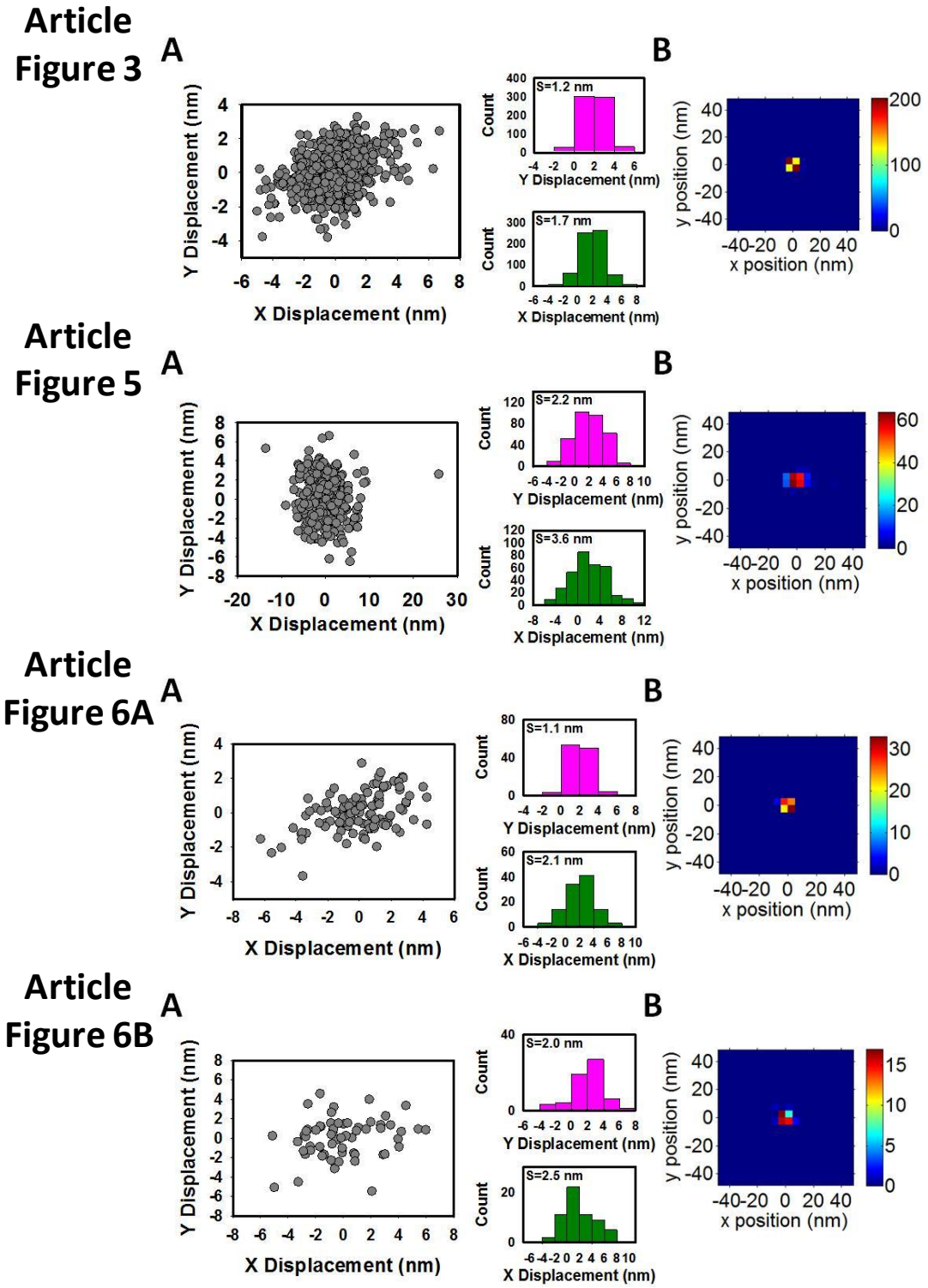

Figure S- 5: (A, left) Scatter plots showing the luminescence centroid positions for the aggregates in the Article. (0,0) represents the mean position of all luminescence centroids. (A, right) Histograms showing the centroid displacement from the mean in both the x (green) and y (pink) directions. (B) Two-dimensional histogram, showing that the frequency with which a particular x_0, y_0 location is fit. (This histogram contains a vertical reflection of the data in the scatter plot).

Calculating the Resolution of the Luminescence and SERS Signals

The accuracy of determining the position of a diffraction-limited emitter through point spread function fitting can be calculated using the following expression[5,6]:

$$\sigma_{u_i} = \sqrt{\left(\frac{s_i^2}{N} + \frac{a^2/12}{N} + \frac{8\pi s_i^4 b^2}{a^2 N^2} \right)} \qquad \text{(S-2)}$$

In this equation, the standard error of the mean of the point spread function, σ_μ, is dependent upon: the standard deviation of the Gaussian fit (s_x and s_y from equation S-1), s_i; the pixel size of the CCD camera in nm, a; the standard deviation of the background in photons, b; and the number of collected photons, N. As an example, we calculate the theoretical accuracy of the fit for the nanoparticle aggregate shown in Figure 2B and Figure S-3. For the luminescence data, we use the average number of emitted photons for N, while in the SERS data, we choose the frame corresponding to the *lowest* SERS signal. For the latter case, this provides an upper limit of the calculated accuracy, since all events with higher signal will have a lower calculated accuracy.

Table S-1: Standard error of the mean for the SERS and luminescence centroids

Parameter	Luminescence	SERS (worst case)
s **(pixels, pixel)**	4.03	4.26
a **(nm per pixel)**	46	46
s **(nm)**	185.38	195.96
b **(photons)**	62.9	62.9
N **(photons)**	3.3×10^5	5.25×10^4
σ_μ **(nm)**	**0.78**	**5.09**

Spatial Intensity Map of Figure 5A in Article

All spatial intensity maps shown in the Article were prepared using the fitting algorithm described above, with the exception of Figure 5A. The intensity time trace for this aggregate showed significant "flicker noise" which makes it difficult to draw a clean threshold using the associated spectral data. For this map, instead of the normal single threshold, two thresholds were defined.

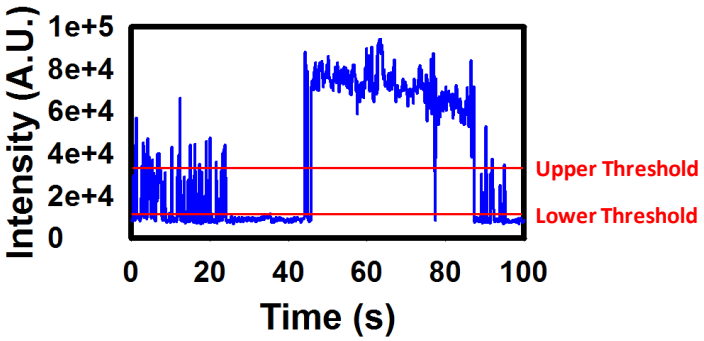

Figure S-6: Intensity time trace threshold levels for Article Figure 5A

The lower threshold was drawn just above the luminescence background and the upper threshold was drawn towards the top of the flicker noise. This parameter and the fact that $R^2 \geq 0.8$ prevents most of those flicker on events from being included in the spatial intensity map. The flicker events leads to poor fitting resolution, which extends the spatial intensity map over a larger area than is possible based on the size of the nanoparticle (although the shape and intensity gradient behavior is preserved). The majority of data appearing in that spatial intensity map will be fit from the strong on event from ~50 to 90 seconds. Other than this change in threshold levels, the Gaussian fitting procedure was the same for the aggregate of Figure 5 in the Article.

DDA Results for Figure 6B

The dielectric function of silver chosen to parametrize our DDA calculations was taken from Palik.[7] All numerical electrodynamics studies involved an interdipole spacing of 1 nm except for the calculations underlying Fig. 4B, which were performed using a 2 nm interdipole spacing.

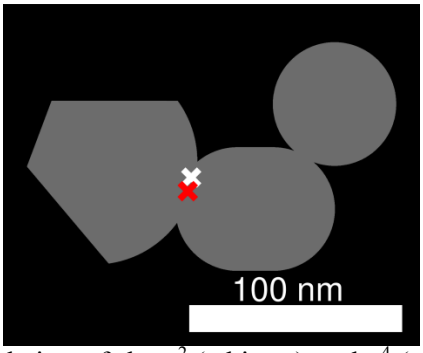

Figure S-7: Rough DDA calculation of the ε^2 (white x) and ε^4 (red x) centroid positions for the modeled trimer

References

(1) Lee, P. C.; Meisel, D.: Adsorption and Surface-Enhanced Raman of Dyes on Silver and Gold Sols. *J. Phys. Chem.* 1982, *86*, 3391-3395.

(2) Weber, M. L.; Willets, K. A.: Correlated Super-Resolution Optical and Structural Studies of Surface-Enhanced Raman Scattering Hot Spots in Silver Colloid Aggregates. *J. Phys. Chem. Lett.* 2011, *2*, 1766-1770.

(3) Stranahan, S. M.; Willets, K. A.: Super-Resolution Optical Imaging of Single-Molecule SERS Hot Spots. *Nano Lett.* 2010, *10*, 3777-3784.

(4) Stranahan, S. M.; Titues, E. J.; Willets, K. A.: SERS Orientational Imaging of Silver Nanoparticle Dimers. *J*. *Phys*. *Chem*. *Lett*. 2011, *2*, 2711-2715.
(5) Yildiz, A.; Selvin, P. R.: Fluorescence Imaging with One Nanometer Accuracy: Application to Molecular Motors. *Acc*. *Chem*. *Res* 2005, *38*, 574-582.
(6) Thompson, R. E.; Larson, D. R.; Webb, W. W.: Precise Nanometer Localization Analysis for Individual Fluorescent Probes. *Biophys*. *J*. 2002, *82*, 2775-2783.
(7) *Handbook of Optical Constants of Solids*; Palik, E. D., Ed.; Academic Press: New York, 1985, pp 275-367.

Chapter 9

MOLECULAR-ELECTRONIC STRUCTURE IN A PLASMONIC ENVIRONMENT: ELUCIDATING THE QUANTUM IMAGE INTERACTION

My contribution to this work: I was intimately involved with all aspects of this project. While working on this project, I mentored summer undergraduate research students Ryan Brewster and Bo Lee, who both became co-authors on the resulting manuscript.

This article has been cited 2 times as of November 16, 2015.[3,181]

THE JOURNAL OF PHYSICAL CHEMISTRY C

Article

pubs.acs.org/JPCC

Molecular−Electronic Structure in a Plasmonic Environment: Elucidating the Quantum Image Interaction

Jonathan P. Litz, Ryan P. Brewster, Alexander B. Lee, and David J. Masiello*

Department of Chemistry, University of Washington, Seattle, Washington 98195-1700, United States

Supporting Information

ABSTRACT: We extend our previous quantum many-body Green's function formalism to characterize the deformations induced in the electronic structure of a quantum emitter when it strongly couples with a plasmon-supporting environment at finite frequency. Through infinite-order perturbation theory, we predict the emergence of subtle yet observable changes in the plasmon-dressed molecule's frontier orbitals, orbital energies, and low-lying electronic excitations when the molecular and plasmonic systems are resonantly coexcited. These distortions, which predominately arise from the finite-frequency image interaction, point to new chemical and optical properties beyond those of the vacuum molecule and bear impact upon resonant plasmon-enhanced molecular spectroscopies and hot-electron-driven chemical catalysis. We propose an experiment capable of testing our predictions.

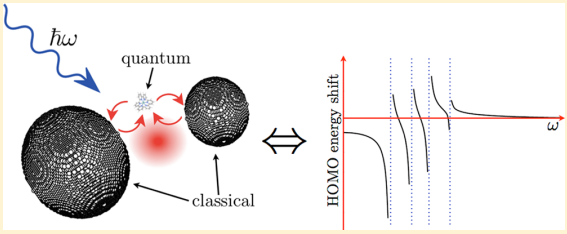

INTRODUCTION

The radiative decay of a quantum emitter such as a molecular chromophore depends not only upon properties intrinsic to the molecule but also upon its environment.[1,2] This is a direct consequence of the boundary conditions inherent to Maxwell's equations, which are so demanding that the radiative emission of a molecule can be radically altered from vacuum due to the presence of a second medium or body.[3−5] In addition, when this medium supports its own unique resonances and those resonances overlap spectrally with those of the molecule, the two systems can be resonantly coexcited. In this regime, the molecule can couple strongly to the second body and its electronic structure may be significantly deformed. The explicit effects of this interaction upon the molecule's electronic structure itself have, until now, been overlooked.

In 1980, Gersten and Nitzan used a classical model to describe the light-driven coupling of a molecular chromophore and a plasmon-supporting nanostructure.[6] They described the two systems as single point dipoles with moments $\boldsymbol{\mu}^{(1)}$ (molecule) and $\mathbf{p}^{(1)}$ (nanostructure) induced by a monochromatic electric field, $\mathbf{E}_0$. Allowing these two dipoles to repeatedly polarize one another leads to the plasmon-dressed molecular polarizability

$$\boldsymbol{\alpha}_{\mathrm{M}}^{\mathrm{D}}(\omega) = [\mathbf{1} - \boldsymbol{\alpha}_{\mathrm{M}}(\omega)\cdot\boldsymbol{\Lambda}\cdot\boldsymbol{\alpha}_{\mathrm{S}}(\omega)\cdot\boldsymbol{\Lambda}]^{-1}\cdot\boldsymbol{\alpha}_{\mathrm{M}}(\omega) \tag{1}$$

where $\boldsymbol{\alpha}_{\mathrm{M}}$ and $\boldsymbol{\alpha}_{\mathrm{S}}$ are the vacuum polarizabilities corresponding to $\boldsymbol{\mu}^{(1)}$ and $\mathbf{p}^{(1)}$, respectively, and $\boldsymbol{\Lambda}$ is the fully retarded dipole-relay tensor.[7] The prefactor in eq 1 is a unitless, frequency-dependent proportionality constant that accounts for the increase in effective molecular polarizability resulting from the infinite-order polarization and back-polarization of the molecule and the nanostructure by one another. Gersten and Nitzan identified this term as the image denominator because it can be interpreted as accounting for the finite-frequency coupling between the molecule and its image in the surface of the nanostructure. Using the dressed polarizability gives the desired relation

$$\boldsymbol{\mu}^{(1)}(\omega) = \boldsymbol{\alpha}_{\mathrm{M}}^{\mathrm{D}}(\omega)[\mathbf{E}_0(\omega) + \boldsymbol{\Lambda}\cdot\mathbf{p}^{(1)}(\omega)] \tag{2}$$

and is necessary to correctly derive the quartic scaling of the electromagnetic enhancement factor in surface-enhanced Raman spectroscopy.[8] If the image recoupling and resulting denominator are not account for, an incorrect quadratic scaling is found, instead.

This model can be extended to determine the energy of interaction between a molecule and the total electric field as

$$W = -\frac{1}{2}\boldsymbol{\alpha}_{\mathrm{M}}^{\mathrm{D}}(\omega)[|\mathbf{E}_0(\omega)|^2 + 2Re\mathbf{E}_0(\omega)^*\mathbf{E}_{\mathrm{S}}(\omega) + |\mathbf{E}_{\mathrm{S}}(\omega)|^2] \tag{3}$$

where $\mathbf{E}_{\mathrm{S}} \equiv \boldsymbol{\Lambda}\cdot\mathbf{p}^{(1)}$ is the electric field scattered by the nanostructure. Equation 3 shows that the energy of interaction is naturally broken into three terms. The first, which depends quadratically on $\mathbf{E}_0$, is the energy associated with the well-known dynamic Stark effect. The second, which is linear in each $\mathbf{E}_0$ and $\mathbf{E}_{\mathrm{S}}$, is the energy of the field-induced van der Waals interaction.[9,10] This term dominates the intermolecular interaction energy between the two systems when the field scattered by both is small in comparison to the source field. However, when a molecule lies in a plasmon-supported

Received: March 27, 2013
Revised: May 13, 2013
Published: May 15, 2013

dx.doi.org/10.1021/jp403047t | J. Phys. Chem. C 2013, 117, 12249−12257

electromagnetic hot spot, the intensity of $\mathbf{E}_S$ can be on the order of 100 times that of $\mathbf{E}_0$, and this term will be minor in comparison to the third, which is quadratic in $\mathbf{E}_S$. This third term is the energy of the image interaction, in which each the molecule and nanostructure repeatedly polarize the other through the electric field. The image denominator of $\boldsymbol{\alpha}_M^D$ accounts for repetitions of this interaction to infinite-order and is essential at frequencies ω where $\mathbf{1} \sim \boldsymbol{\alpha}_M(\omega)\cdot\boldsymbol{\Lambda}\cdot\boldsymbol{\alpha}_S(\omega)\cdot\boldsymbol{\Lambda}$. This condition is met when both a plasmonic and molecular−electronic excitation experience a resonance at a common frequency. In this strong-coupling regime, the molecule becomes anomalously polarized by its image and any finite-order perturbative approach will fail. A theoretical description of such extreme nanoscale light−matter interactions for real systems of experimental interest is important because these conditions are relevant in plasmon-enhanced molecular−optical processes in spectroscopy, sensing, and catalysis, yet their description is challenging, because there are no standard computational approaches available that are capable of exploring this regime from first principles.

Recent first-principles treatments of molecule−plasmon interactions often approach the problem from a quantum-chemical perspective, where the effects of the plasmon are included within a time-dependent DFT (TD-DFT) description of the molecule by the addition of a potential energy to the KS Hamiltonian; this potential might come from approximating the metal nanostructure (with $\gtrsim 10^6$ atoms) by a polarizable continuum model,[11,12] by clusters of ∼100 atoms described fully quantum-mechanically,[13−17] by a capacitance−polarizability interaction model of nanoparticle monomers with a few thousand discrete classical "atoms",[18,19] or by incorporating the nanostructure's local field directly from continuum electrodynamics;[20,21] see refs 22, 23 for a review. In these approaches, attention is placed on chemical interactions between molecule and metal and upon the computation of molecular spectra (e.g., Raman, fluorescence, circular dichroism, etc.), where the damping of electronic excitations due to interactions with the plasmon is phenomenologically parametrized. Explicit consideration of the deformations of the plasmon-dressed molecule's ground- and excited-state electronic structure is not made. Other notable theoretical efforts include the meshing of a two-state random-phase approximation of the molecule with a finite-difference time-domain (FDTD) description of the plasmon's electrodynamics.[24−26] In the static limit, a method has been developed to describe the electronic structure of a molecule in an arbitrary electrostatic environment.[27] Additionally, while not from first principles, a significant theoretical understanding of the molecule−plasmon interaction has been gained from a number of model theories that have elucidated the conditions under which interferences between molecular and plasmonic resonances, like the Fano and induced-transparency effects,[28,29] become pronounced. Likewise, molecule−surface interactions have been studied within the context of on-molecular-resonance field-driven van der Waal's interactions, but these studies neglect the potentially intense electric fields scattered by surface resonances.[9,10]

Previously, we established a many-body Green's function formalism to model molecule−plasmon interactions from first principles, and we numerically implemented it to determine how a molecule's electronic structure is modified by a nearby plasmonic excitation as well as how surface-plasmon resonances are impacted by resonant molecular media.[8,30] However, this approach was limited in three ways: First, it depended upon an analytic form of the nanostructure's polarizability, which limited its application to simple nanoparticle shapes and configurations. Second, the explicit frequency dependence of the image interaction was not completely accounted for; in particular, the image response at the laser driving frequency ω was not included. Third, the proper self-energy accounting for molecule−plasmon interaction was evaluated at frequencies far from molecular resonances. This limited the accuracy of calculations in the regime where molecule and metal are coresonantly excited.

In this paper, we resolve each of these issues and significantly expand the scope of our formalism, enabling us to elucidate the impact of nanoscale light−matter interactions in the strong-coupling regime on molecular electronic structure. In our approach, the molecule is treated with first-principles quantum mechanics, while the plasmonic system is described by fully retarded continuum electrodynamics. Their repeated interaction is rigorously included through Dyson resummation techniques within the language of many-body Green's function theory.[8,31−33] The quantum analog of the image denominator, including its explicit frequency dependence, is recovered and analyzed to reveal a rich pole structure that we interpret as the finite-frequency quantum image interaction. Through our analysis we determine the conditions under which the effect is maximized and predict how a molecule's chemical and optical activity are altered by determining the change in its frontier orbitals, HOMO−LUMO gap, and low-lying electronically excited states. This bears impact upon a variety of plasmon-enhaced molecular optical processes as well as the emerging field of hot-electron initiated chemical catalysis, where being able to control the energetic position of the molecule's HOMO or LUMO relative to the metal's Fermi level is important. We also propose the design of an experiment that combines optical spectroscopy with an electron probe in the form of electron energy-loss spectroscopy (EELS) to measure the deformations of the plasmon-dressed molecule's electronic structure, thereby testing our predictions.

IMAGE INTERACTION AT FINITE FREQUENCY

Within the Born−Oppenheimer approximation, the Hamiltonian of a quantum molecule immersed in a classical electromagnetic field and simultaneously interacting with a quantum plasmonic system is

$$\hat{H}_{mol} + \hat{H}_{int} = U_0 + \hat{F} + \sum_{pq} \langle p|\hat{U}_{im} + U_{src}|q\rangle N\{\hat{c}_p^\dagger \hat{c}_q\} + \frac{1}{2}\sum_{pqrs} \langle pq|V_{e-e}|rs\rangle N\{\hat{c}_p^\dagger \hat{c}_q^\dagger \hat{c}_s \hat{c}_r\} \quad (4)$$

where p, q, r, and s label arbitrary molecular orbitals, and the time-dependence of the operators is suppressed for simplicity of presentation. In addition to the Hartree-Fock (HF) ground-state energy U_0 and Fock operator $\hat{F}$, molecular electrons are coupled to the source field $\mathbf{E}_0$ through $-\Sigma_{pq}\langle p|U_{src}|q\rangle N\{\hat{c}_p^\dagger \hat{c}_q\}$, where we invoke the electric−dipole approximation, $U_{src} \approx -(-e\mathbf{x})\cdot\mathbf{E}_0$. Explicit two-body interactions between mean-field electrons are accounted for through $(1/2)\Sigma_{pqrs}\langle pq|V_{e-e}|rs\rangle N\{\hat{c}_p^\dagger \hat{c}_q^\dagger \hat{c}_s \hat{c}_r\}$. This leaves only the molecule−plasmon polarization (image) coupling, $\hat{U}_{im} \approx -(-e\mathbf{x})\cdot\boldsymbol{\Lambda}\cdot\hat{\mathbf{p}}$. $\boldsymbol{\Lambda} = e^{ikr}\{(1/r^3 - ik/r^2)[3\hat{\mathbf{n}}\hat{\mathbf{n}} - 1] - k^2\hat{\mathbf{n}}\times(\hat{\mathbf{n}}\times)/r\}$ is the standard dipole tensor that relays the electric field generated by a dipole at one point in space to the point $\mathbf{x} = r\hat{\mathbf{n}}$, a distance r away. Møller−Plesset perturbation theory[34] provides one route to including the

interaction effects of other electrons and the source field upon the mean-field molecular−electronic system, and these electron-correlation effects are well-understood.[13−17] However, there are no standard approaches to build in the effects of the image interaction because it requires infinite-order perturbation theory at finite frequency to account for the repeated polarization interaction between molecule and plasmon.

To approach the image effect, we begin with a mean-field description [e.g., Hartree−Fock (HF)[35,36] or Kohn−Sham density functional theory (KS-DFT)[37,38]] of the electronic ground state of an arbitrary vacuum molecule and impose the effects of the molecule−plasmon polarization interaction

$$\begin{aligned}\hat{H}_{\mathrm{im}}(t) &\approx -\hat{\boldsymbol{\mu}}(t)\cdot\boldsymbol{\Lambda}\cdot\hat{\mathbf{p}}(t)\\ &= -\sum_{pq}\boldsymbol{\mu}_{pq}N\{\hat{c}_p^{\dagger}(t)\hat{c}_q(t)\}\cdot\boldsymbol{\Lambda}\\ &\quad\cdot\int_V \hat{\Omega}^{\dagger}(\mathbf{x},t)(-e\mathbf{x})\hat{\Omega}(\mathbf{x},t)\,\mathrm{d}^3x\end{aligned} \tag{5}$$

expressed in terms of the vacuum molecule's dipole-matrix elements $\boldsymbol{\mu}_{pq} = \langle p|-e\mathbf{x}|q\rangle$ and the quantized plasmonic dipole moment $\hat{\mathbf{p}}(t) = \int_V \hat{\Omega}^{\dagger}(\mathbf{x},t)(-e\mathbf{x})\hat{\Omega}(\mathbf{x},t)\,d^3\mathbf{x}$ with corresponding bosonic plasmon field operators $\hat{\Omega},\hat{\Omega}^{\dagger}$. Equation 5 derives from the fact that the plasmon sets up a time-dependent potential, and the energy of interaction is computed by placing the molecule into that potential and integrating over all space.

With $\hat{H}_{\mathrm{im}}$, we employ Dyson's perturbation theory to construct the molecule's image-dressed electronic propagators. The first-order interaction between the two systems time-averages to zero. At second order, the proper self-energy describing how molecular electrons are polarized by their image in the metal is

$$\begin{aligned}\Sigma^{\bigstar(2)}_{pq}(t,t') &= \frac{1}{\hbar^2}\sum_{rs}\boldsymbol{\mu}_{pr}\cdot\boldsymbol{\Lambda}\cdot\langle\Omega_0|T\{\hat{\mathbf{p}}(t)\hat{\mathbf{p}}(t')\}|\Omega_0\rangle\\ &\quad\cdot G_{rs}(t,t')\cdot\boldsymbol{\Lambda}\cdot\boldsymbol{\mu}_{sq}\end{aligned} \tag{6}$$

where $|\Omega_0\rangle$ is the Fock state of the plasmon and $iG_{pq}(t,t') = \langle\Phi_0|T\{\hat{c}_p(t)\hat{c}_q^{\dagger}(t')\}|\Phi_0\rangle$ are the one-body electronic propagators (Green's functions) of the vacuum molecule expressed in terms of the time-ordered product of basic fermionic operators $\hat{c}_p,\hat{c}_p^{\dagger}$ taken with respect to the molecule's ground-state mean-field reference $|\Phi_0\rangle$.

To make a connection with the continuum electrodynamics of nanoscopic metal structures, we could replace the plasmonic dipole−dipole correlation function in eq 6 by its retarded component, i.e., $\theta(t-t')\langle\Omega_0|[\hat{\mathbf{p}}(t),\hat{\mathbf{p}}(t')]|\Omega_0\rangle = -i\hbar\boldsymbol{\alpha}_S(t,t')$[39,40] and interpret the complex-valued metallic polarizability $\boldsymbol{\alpha}_S$ as being parametrized by the dielectric properties of bulk material.[8,30] This effects a dequantization of the plasmon field in a manner consistent with the Bogoliubov decomposition of macroscopically occupied quantum fields.[41] However, analytical expressions connecting the microscopic polarizability and the macroscopic dielectric function for nanostructures of arbitrary morphology and aggregation scheme are often unknown, and further approximations must be made.[42] To make our method applicable to more general nanostructures, we break the correlations inherent in the plasmonic propagator according to

$$\begin{aligned}\langle\Omega_0|T\{\hat{\mathbf{p}}(t)\hat{\mathbf{p}}(t')\}|\Omega_0\rangle &\approx \langle\Omega_0|\hat{\mathbf{p}}(t)|\Omega_0\rangle\langle\Omega_0|\hat{\mathbf{p}}(t')|\Omega_0\rangle\\ &= [\theta(t-t')+\theta(t'-t)]\\ &\quad\cdot\mathbf{p}^{(1)}(t)\mathbf{p}^{(1)}(t')\end{aligned} \tag{7}$$

and re-express the previous self-energy in terms of the continuum electric field generated by the plasmon, $\mathbf{E}_S(\mathbf{x},t) = \boldsymbol{\Lambda}(\mathbf{x})\cdot\mathbf{p}^{(1)}(t)$, evaluated at the position of the molecule (chosen to be at $\mathbf{x} = 0$). This field can be computed from any numerical approach for solving the continuum set of Maxwell's equations. Since the plasmonic field $\mathbf{E}_S(\mathbf{x},t) = \mathbf{E}^{(+)}(\mathbf{x})e^{-i\omega t}+\mathbf{E}^{(-)}(\mathbf{x})e^{i\omega t}$ has both forward and backward propagating components, the presence of the Heaviside function, θ, allows us to identify and eliminate those processes that do not correspond to the image interaction, such as two-photon absorption and emission. This results in the following equation for the proper time-ordered self-energy

$$\begin{aligned}\hbar\Sigma^{\bigstar(2)}_{pq}(z) &\approx \sum_i \frac{\boldsymbol{\mu}_{pi}\cdot\mathbf{E}^{(-)}\mathbf{E}^{(+)}\cdot\boldsymbol{\mu}_{iq}}{\hbar z-\hbar\omega-\varepsilon_i^0-i\eta}\\ &\quad+\sum_a \frac{\boldsymbol{\mu}_{pa}\cdot\mathbf{E}^{(+)}\mathbf{E}^{(-)}\cdot\boldsymbol{\mu}_{aq}}{\hbar z+\hbar\omega-\varepsilon_a^0+i\eta}\end{aligned} \tag{8}$$

expressed in the Fourier frequency z conjugate to the relative time $t-t'$ between interactions. Here i and a denote occupied and virtual molecular orbitals, respectively. The electric field components satisfy $\mathbf{E}^{(+)} = [\mathbf{E}^{(-)}]^*$ at frequency ω, and ε_p^0 and ρ_p^0 are the orbital energies and occupation numbers of the vacuum molecule. To converge the Fourier integral, the positive infinitesimal η is used. Because this approximate self-energy is parametrized by the electric field components $\mathbf{E}^{(+)}$ and $\mathbf{E}^{(-)}$, which are chosen to be real-valued at the position of the molecule, η also serves to regulate the real zero in the denominator of eq 8. This allows us to numerically integrate around specific poles of $\boldsymbol{\Sigma}^{\bigstar}_{(2)}$ without indenting the contour. Physically, the imaginary component of $\boldsymbol{\Sigma}^{\bigstar}_{(2)}$, which is proportional to η, is related to the lifetime of the dressed molecular states. However, in this paper we are only interested in the energetic shift associated with the dressing. Therefore, we use η strictly as a mathematical tool to prevent divergence of $\boldsymbol{\Sigma}^{\bigstar}_{(2)}$ and place no physical significance on it.

With $\boldsymbol{\Sigma}^{\bigstar}_{(2)}$ determined, Dyson's perturbation theory prescribes a method for building in the effects of this interaction upon the noninteracting molecular system to infinite order in perturbation theory, yielding a nonperturbative result. This is accomplished by resumming the geometric series

$$\begin{aligned}\mathcal{G}(z) &= \mathbf{G}(z)+\mathbf{G}(z)\boldsymbol{\Sigma}^{\bigstar}_{(2)}(z)\mathbf{G}(z)+\ldots\\ &= [\mathbf{G}^{-1}(z)-\boldsymbol{\Sigma}^{\bigstar}_{(2)}(z)]^{-1}\end{aligned} \tag{9}$$

yielding the $K\times K$ matrix-representation of the electronic propagators of the image-dressed molecule $\mathcal{G}$ driven at the frequency ω, in terms of the noninteracting propagators

$$G_{pq}(z) = \delta_{pq}\left[\frac{\rho_p^0}{z-\varepsilon_p^0/\hbar-i\eta}+\frac{1-\rho_p^0}{z-\varepsilon_p^0/\hbar+i\eta}\right] \tag{10}$$

of the vacuum molecule. The diagrammatic representation of $\mathcal{G}$ is presented in Figure 1. With the self-energy defined in eq 8, this resummation represents the quantum-mechanical analog of

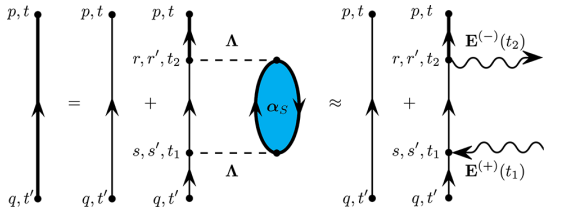

Figure 1. Diagrammatic representation of the Dyson expansion of the interacting Green's function $\mathcal{G}$ corresponding to the image interaction. Thick (thin) black lines represent interacting (noninteracting) molecular−electronic propagators, and dashed black lines indicate interactions between molecular and plasmonic dipole moments mediated by the dipole-relay tensor $\mathbf{\Lambda}$. Upon breaking the correlations in the plasmon's polarization bubble (blue), we obtain the approximation shown on the right, which involves the electric field components $\mathbf{E}^{(\pm)}$ of the plasmon, as indicated by the wavy lines. The other time ordering of these components ($t_2 < t_1$) is not depicted but is included in eq 8.

the repeated polarization interaction between molecule and metal that is accounted for in the Gersten−Nitzan model through the image denominator. While previously discussed at the (many-body) excitation level,[6] here we show that the effect is relevant even at the level of the electronic ground state and its underlying one-body wave functions. As in the classical case, incorporation of the infinite order image interaction is essential for the correct description of the physics, with $1 - \mathbf{G}(z)\mathbf{\Sigma}^{\star}_{(2)}(z)$ carrying the role of the image denominator $\mathbf{1} - \boldsymbol{\alpha}_{\mathrm{M}}(\omega)\cdot\mathbf{\Lambda}\cdot\boldsymbol{\alpha}_{\mathrm{S}}(\omega)\cdot\mathbf{\Lambda}$ at the level of $\mathcal{G}$. Details of the complete connection between the one- and many-body levels of the description of the image interaction are documented in our previous work.[8,30]

INTEGRATION OF THE ENERGY SHELL

While $\mathbf{G}$ exhibits responses (so-called *principle* poles) at the ionization potentials and electron affinities of the vacuum molecule, $\mathbf{\Sigma}^{\star}_{(2)}$ may *induce* additional responses in $\mathcal{G}$ that modify the physics of the interacting molecule. However, the frequency z (or energy $\hbar z$) appearing in these expressions is not physical and must be removed to extract meaningful physics. One approach to eliminate z is to Taylor expand the self-energy around the vacuum molecule's orbital energies and retain only the zeroth-order term.[30] However, as z is tuned into resonance with the denominator in eq 8, the molecule and plasmon become strongly coupled and any finite-order Taylor approximation breaks down.

To overcome this challenge, we identify a z-independent potential energy

$$\hbar\mathbf{\Sigma}_0 = \oint_{\mathrm{IP}} [\mathbf{\Sigma}^{\star}_{(2)}(z)\mathcal{G}(z) + \mathcal{G}(z)\mathbf{\Sigma}^{\star}_{(2)}(z)]\,\frac{\mathrm{d}(\hbar z)}{2\pi i} \tag{11}$$

that accounts entirely for the influence of the plasmon's polarization upon the molecule's ground-state energy. This term is determined from the following expression for the ground state energy of the interacting system:

$$\begin{aligned}\mathcal{U}_0 &= Tr \oint_{\mathrm{IP}} [\mathbf{h} + \hbar z\mathbf{1}]\mathcal{G}(z)\,\frac{\mathrm{d}z}{4\pi i} \\ &= \frac{1}{2}Tr[\mathbf{h} + \mathbf{F}]\boldsymbol{\rho} + \frac{1}{2}\mathrm{Tr}\oint_{\mathrm{IP}} [\mathbf{\Sigma}^{\star}_{(2)}(z)\mathcal{G}(z) \\ &\quad + \mathcal{G}(z)\mathbf{\Sigma}^{\star}_{(2)}(z)]\,\frac{\mathrm{d}(\hbar z)}{4\pi i}\end{aligned} \tag{12}$$

where $\mathbf{h}$ is the noninteracting one-body part of H_{mol} and where we have used $G(z) = [z\mathbf{1} - \mathbf{F}/\hbar]^{-1}$ to complete the equality. After decomposing the proper self-energy $\mathbf{\Sigma}^{\star}_{(2)}(z) = (1/2)\mathbf{\Sigma}_0\boldsymbol{\rho}^{-1} + \mathbf{\Sigma}_R(z)$ into z-independent and z-dependent components and demanding that the former term inherits all of the image interaction physics,[43,44] the interacting ground state energy becomes

$$\begin{aligned}\mathcal{U}_0 &= \frac{1}{2}Tr\left\{[\mathbf{h} + \mathbf{F}]\boldsymbol{\rho} + \frac{1}{2}\hbar\mathbf{\Sigma}_0\right\} \\ &= \frac{1}{2}Tr\{[\mathbf{h} + \mathbf{F} + \hbar\mathbf{\Sigma}_0]\boldsymbol{\rho}\}\end{aligned} \tag{13}$$

with the replacement $Tr\mathbf{\Sigma}_0 = 2Tr\mathbf{\Sigma}_0\boldsymbol{\rho}$ connecting the traces of the full self-energy and its occupied components; see the Supporting Information. A similar approach was developed to compute the electron−electron correlation energy in molecular systems.[43,44] In $\hbar\mathbf{\Sigma}_0$, the contour is routed around only those poles that correspond to ionization-potential (IP)-like processes. These poles can be traced back adiabatically to the principle IPs of the vacuum molecule. Integrating around only these poles is challenging, as the induced poles can cross principle poles and even other induced poles as a function of the excitation frequency ω. Because of this, standard Coulson integration techniques are ineffective. Instead we use η to move poles away from the real axis and integrate around the upper-half plane, which contains only IP-like poles. In our calculations, $\eta = 0$ provides an upper bound for the magnitude of the calculated shift in orbital energies. Therefore, the shifts that we report are conservative lower bounds for the actual deformation.

Once the necessary integrals are evaluated, an application of the variational principle upon the interacting ground-state energy of the molecule yields the following one-body equation

$$[\mathbf{F} + \hbar\mathbf{\Sigma}_0]\boldsymbol{\chi} = \boldsymbol{\chi}\boldsymbol{\varepsilon} \tag{14}$$

where $\boldsymbol{\chi}$ and $\boldsymbol{\varepsilon}$ are the matrix representations of the image-dressed orbitals and corresponding orbital energies. Solutions of this equation depend parametrically upon the local field $\mathbf{E}_{\mathrm{S}}$ of the plasmon as well as upon ω. The matrix $\mathbf{F}$ is either the standard Fock or KS Hamiltonian, depending upon the level of theory used in the fiducial molecular system.

NUMERICAL SIMULATIONS

We numerically implement our formalism within the Q-Chem software package[45] and the discrete-dipole approximation (DDA).[46] Through the former, a vacuum molecule's ground- and excited-state structure may be computed at varying levels of theory from semiempirical to ab initio. The latter solves the fully retarded three-dimensional electromagnetic scattering problem at finite frequency for nanoscale metal targets of arbitrary morphology and aggregation scheme based upon the material's bulk dielectric properties. Combining these bottom-up and top-down approaches provides an advantage, because it rigorously describes the essential physics yet provides a

computationally tractable route to simulating real experiment. For the purposes of the presented calculations, we choose the B3LYP/6-31G* level of theory for the molecular electronic structure. In addition, we choose the subsequent plasmon-dressing to only modify the electronic degrees of freedom with the underlying atomic nuclei, which are significantly less polarizable, held fixed at their vacuum equilibrium geometry. All DDA calculations presented involve silver nanoclusters represented with 1 nm dipole spacing and with bulk dielectric properties taken from Palik.[47] We do not bring $\mathcal{G}$ into self-consistency with $\boldsymbol{\Sigma}^{\star}_{(2)}$ in the present study, however, this conserving approximation[33] will be explored in the future. η is set to 0.27 eV, which provides a sufficient shift to allow us to perform calculations on resonance.

Analytical analysis of the pole structure appearing in the first term of the Dyson expansion of $\mathcal{G}$ in eq 11 reveals principle poles at $\hbar z = \varepsilon_p^0 \pm i\eta$ and induced poles at $\hbar z = \varepsilon_i^0 + \hbar\omega + i\eta$ and $\hbar z = \varepsilon_a^0 - \hbar\omega - i\eta$. The residues at these poles make explicit the basic mechanism of the quantum image interaction: An electron in the ith occupied molecular orbital "sees" its image, as mediated by the plasmon oscillating at frequency ω, as a sum of interactions with all virtual orbitals a of the form $\boldsymbol{\mu}_{ia}\cdot\mathbf{E}^{(+)}\mathbf{E}^{(-)}\cdot\boldsymbol{\mu}_{ai}/(\varepsilon_i + \hbar\omega - \varepsilon_a + 2i\eta)$; each virtual orbital sees the occupied orbitals in a complementary manner. Occupied−virtual orbital pairs with energies differing by approximately the energy of incident light (i.e., $\varepsilon_a - \varepsilon_i \approx \hbar\omega$) and that have a large overlap between $\boldsymbol{\mu}_{ia}$ and $\mathbf{E}^{(\pm)}$ will couple strongly. At second order in the Dyson expansion, each electron may additionally interact twice with its image in the plasmon such that a pair of induced occupied−virtual responses resonate (i.e., $\varepsilon_i + \hbar\omega \approx \varepsilon_a - \hbar\omega$). In this case, occupied−virtual pairs with energies that differ by 2ω can participate resonantly in the interaction. Because the proper self-energy $\boldsymbol{\Sigma}^{\star}_{(2)}$ is of second-order in perturbation theory, no additional features arise at higher orders in the Dyson expansion beyond repetitions of those already mentioned. A pictorial representation of the first-order mechanism can be found in Figure 2. However, we emphasize that all numerical results presented involve the infinite-order resummation of $\mathcal{G}$ in eq 11.

PLASMON-DRESSED MOLECULAR ORBITALS AND APPROXIMATE EXCITATIONS

The presence of these responses manifests itself in the deformations of the metal-dressed molecule's ground-state one-body electronic structure, such as in its ionization potentials, its electron affinities, and their energetic separations. Using the planar molecule pyrazine as a first example of our formalism, Figure 3 displays the spectral dependence of its metal-dressed frontier orbitals (upper panels), compared to the corresponding orbital in the vacuum molecule. The molecule is immersed within a fictitious broadband plasmonic environment driven with a source field of magnitude $|\mathbf{E}_0| = 5.14 \times 10^5$ V/cm for the in-plane and 1.54×10^6 V/cm for the out-of-plane polarizations; the field is assumed to be amplified by a factor of 100 at the position of the molecule for all frequencies of incident light. A constant enhancement factor is chosen to enable exploration of the frequency-dependence of the image interaction based on vacuum molecular properties and field orientation without other confounding effects. The orientation of the molecule with respect to the field is shown in the figure inset. Pyrazine's HOMO−LUMO transition aligns strongly with the out-of-plane polarization, while other low-lying transitions overlap with the in-plane polarization. Our

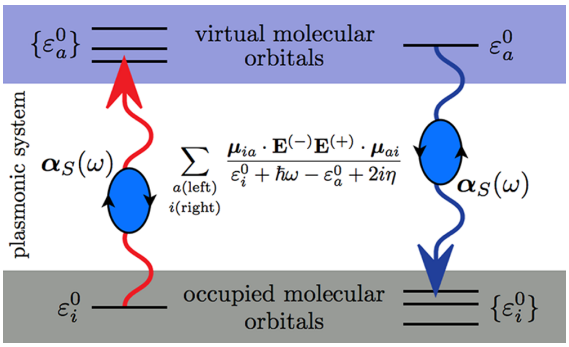

Figure 2. Pictorial depiction of the mechanism of the quantum image interaction upon the electronic ground-state orbitals of a molecule. An electron in the ith occupied molecular orbital of energy ε_i^0 "sees" its image in the manifold of image virtual orbitals of energy $\{\varepsilon_a^0\}$ that are resonantly coupled to it through the plasmon oscillating at frequency ω (left). The opposite is true for the image-dressing of the molecule's virtual orbitals (right). The diagonal component of the first-order perturbative approximation to the image interaction $\hbar\boldsymbol{\Sigma}_0$ is displayed in the figure; the denominator shows this resonance condition, while the numerator makes explicit how the image interaction depends upon the relative orientations of the molecular−electronic dipole moment and plasmonic field.

calculations reveal the presence of both positive and negative orbital energy shifts on the order of 0.1 eV in magnitude when the plasmonic field is polarized along the directions of these low-lying electronic transitions. For example, in the upper left panel, we see that when the plasmon is brought into resonance with and is polarized along pyrazine's HOMO−LUMO transition ($N \rightarrow N + 1$), the energies of the HOMO and LUMO shift together in a frequency-dependent manner. A similar effect is found when the field is polarized in the direction of other low-lying transitions (upper right). This is to be expected from our analytical analysis, where the largest deformations are predicted at those excitation frequencies where the plasmon energy $\hbar\omega = \varepsilon_a^0 - \varepsilon_i^0$ and $2\hbar\omega = \varepsilon_a^0 - \varepsilon_i^0$. These shifts follow a dispersive line shape because $\hbar\boldsymbol{\Sigma}_0$ is directly proportional to the molecule's linear polarizability, the real part of which has a dispersive line shape that is negative (positive) when $\hbar\omega$ is red (blue) of each transition $\varepsilon_a^0 - \varepsilon_i^0$ and is maximal in magnitude when both systems are resonantly coexcited. In this example, every electronic transition resonantly interacts with its image in the plasmon, since a fictitious broadband plasmonic field is used.

Signatures of these deformations of pyrazine's one-body electronic structure may be found at the many-body level in both ground and excited states. Due to resonant coupling with a nearby plasmon, the molecular excitation energies may be modified appreciably, affecting plasmon-enhanced spectroscopies and catalysis by deforming molecular potential energy landscapes. In KS-DFT, the HOMO−LUMO gap may provide an approximate description of a molecule's lowest-lying electronically excited state. By approximating the energies of the low-lying electronically excited states of pyrazine by $\varepsilon_a - \varepsilon_i$, we predict significant distortions of its transition energies from vacuum for both out-of-plane and in-plane polarizations of the plasmonic field (Figure 3, lower panels). The spectral-dependence of each excited state tracks the spectral dependence of the deformations of the underlying (one-body) orbital energies comprising it. The magnitude of this image-induced

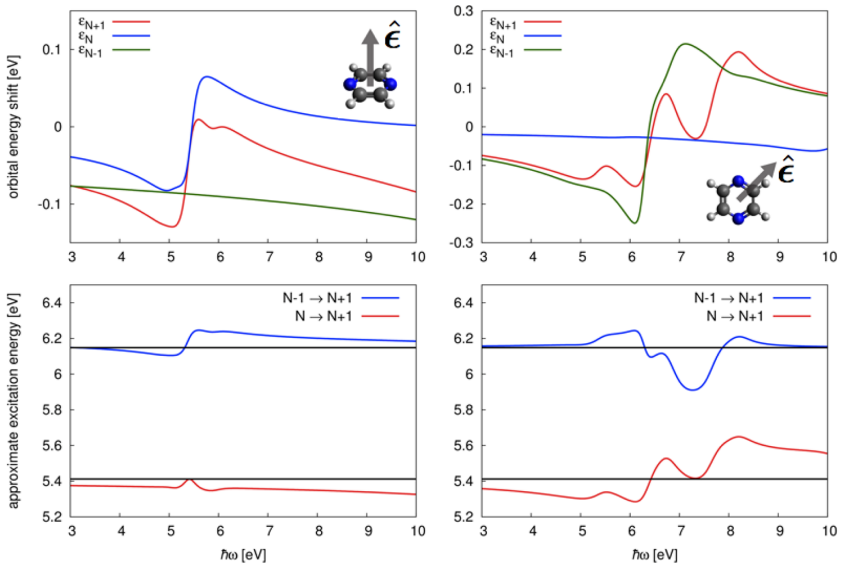

Figure 3. Energetic deformations of the ground-state frontier orbitals (upper panels) and low-lying electronically excited states (lower panels) of the metal-dressed pyrazine molecule with respect to the vacuum molecule as a function of the excitation energy $\hbar\omega$. Incident source fields of $|\mathbf{E}_0| = 1.54 \times 10^6$ and $|\mathbf{E}_0| = 5.14 \times 10^5$ V/cm enhanced at all frequencies by a factor of 100 by a broadband plasmon are chosen to investigate the behavior of the image interaction in the out-of-plane (left panels) and in-plane (right panels) polarization directions shown in the insets. As each orbital resonantly interacts with its image in the plasmon as a function of ω, strong positive or negative shifts in the plasmon-dressed orbital energies are observed. The frequency-dependence of pyrazine's frontier orbital energies (upper panels) is determined by the spectral behavior of the potential energy $\hbar\Sigma_0$, which is directly proportional to the molecule's linear polarizability. These distortions are manifested at the many-body level in the frequency-dependence of pyrazine's excitation spectrum upon plasmon-dressing (lower panels). By approximating the low-lying electronically excited state energies of pyrazine by their most dominant one-body transition $\varepsilon_a - \varepsilon_i$, we predict a surprising and potentially observable spectral dependence that can be traced back to the effect of the resonant image interaction upon pyrazine's one-body wave functions.

deformation is a few tenths of an electronvolt. Because of this, it can in principle play a role in a variety of plasmon-enhanced optical processes in spectroscopy, sensing, and catalysis, where small electronic deformations can have profound effects. Further, more polarizable molecules are expected to experience greater energetic shifts at similar field strengths.

With the dependence of the image interaction upon molecular properties and field orientation now understood, we next investigate the image-dressed electronic structure of an optically active dye molecule, indigo, when it is placed within the junction of the plasmon-supporting silver nanotrimer aggregate displayed in Figure 4. The two systems are driven by far-field linearly polarized radiation of strength $|\mathbf{E}_0| = 1.08 \times 10^5$ V/cm, and at certain frequencies they are resonantly coexcited, which means that the energy of the plasmonic excitation is approximately equal to the energy of a many-electron transition. In this case, the molecule is exposed to the highly polarizable electromagnetic environment set up by the plasmon and becomes dressed as a result of the repeated interaction between its electrons and their image in the plasmon. The upper left panel of Figure 4 displays a two-dimensional representation of the three-dimensional nanotrimer along with the location of the indigo molecule relative to the structure (indicated by the red "×") and its orientation relative to the polarization $\hat{\boldsymbol{\epsilon}}$ of the exciting electric field (upper right); the transition moment vectors of its two lowest-lying optically active excitations are denoted by S_1 and S_2.

The frequency-dependence of the magnitude of the electric near-field localized in the junction of interest (i.e., the hot-spot spectrum) is displayed as the red curve in the lower left panel of Figure 4. Superimposed are the energies of the three frontier orbitals that dominantly compose indigo's S_1 and S_2 transitions. This figure shows that the energies of the HOMO (ε_N) and LUMO (ε_{N+1}) are significantly modified from their vacuum values at those frequencies ω where they resonantly interact with their image in the plasmon. At other frequencies, the plasmon is not excited and the image interaction on these orbitals is suppressed. For the HOMO, the trimer supports a plasmon that is excited at frequencies near $\varepsilon_{N+1} - \varepsilon_N/\hbar$. The same is true for the LUMO. However, the energy of the HOMO−3 (ε_{N-3}) shifts little because there are no appreciable plasmon oscillations at those frequencies connecting it resonantly to any image orbital. Manifestations of these orbital energy distortions can be seen in the excitation spectra in the lower right panel, computed by approximating S_1 and S_2 by the orbitals that dominantly contribute to the transition. The magnitudes of these distortions are large enough to be observed, in principle.

We now suggest an experiment to directly measure the effect of the image interaction: Cutting-edge experiments in nanoplasmonics and nanophotonics are now interrogating nanoscale matter with both swift electron and optical probes.[48−52] EELS performed in a scanning transmission electron microscope (STEM) offers the possibility to map the flow of energy with subnanometer spatial resolution,[53] with an energy resolution approaching 0.1 eV. By correlating this technique with optical spectroscopy, it is possible to excite metal nanostructures embedded within resonant molecular media with optical radiation of well-defined frequency and then probe the molecular media's frontier orbitals via STEM/EELS. A similar

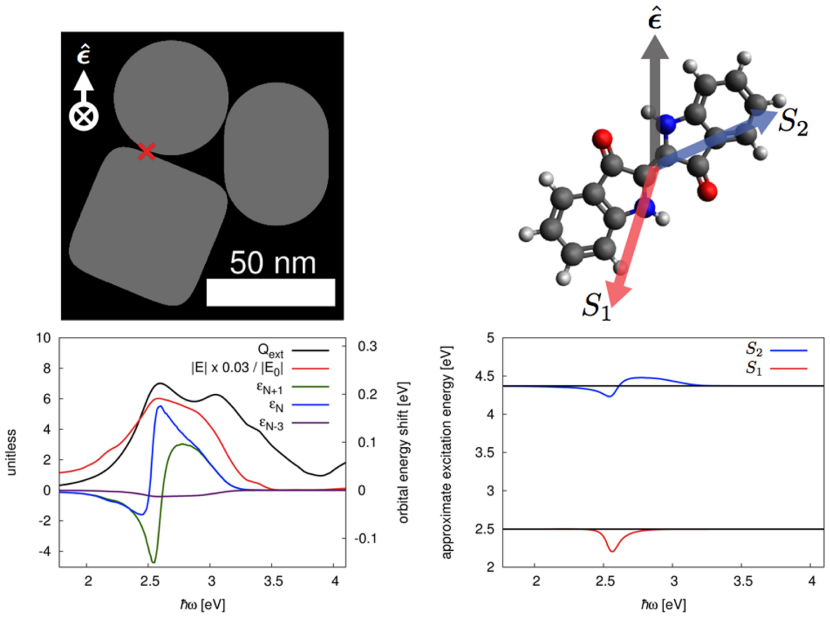

Figure 4. Frequency-dependent energetic deformations of the ground- and excited-state electronic structure of indigo (upper right) as it is subjected to the highly polarizable nanoplasmonic environment of a silver nanotrimer aggregate (upper left). The molecule is located at the red "×", and the system is driven by an electric field of magnitude $|\mathbf{E}_0| = 1.08 \times 10^5$ V/cm. As the two systems are resonantly coexcited, both the one-body and many-body structure of indigo is affected in a frequency-dependent manner. The lower left panel displays the trimer's extinction (black) and near-field intensity or hot-spot (red) spectra, as well as the distortions of the frontier orbitals that contribute dominantly to the S_1 ($N \rightarrow N + 1$) and S_2 ($N - 3 \rightarrow N + 1$) excited states of indigo. The spectral dependence of the image-dressed S_1 (red) and S_2 (blue) transition energies with respect to those of the vacuum molecule (black) are shown in the lower right panel. At excitation energies away from where the plasmon is excited, there is no appreciable image interaction upon the molecular electronic transitions.

technique has been used to measure the band gaps in boron nitride nanotubes[54] and in thin layers of HfO_2.[55] The optical excitation frequency can be either on or off a plasmon resonance, and the subsequent EEL spectrum will read out the varying probabilities for the electron beam to deposit energy into a molecular orbital that may be energetically shifted from its native value. As the STEM is rastered across the nanostructure, molecules located within a hot spot will be dressed by their image in the plasmon, while those located elsewhere will not. The high spatial resolving power of the STEM will expose that information. Since our predictions for these one- and many-body energy deformations are on the order of 0.1 eV, they should be observable with an experiment like this.

CONCLUSION

We have presented a first-principles quantum many-body description of the quantum-mechanical image interaction between a molecular emitter and a nearby plasmon-supporting metal nanostructure at finite frequency. In particular, we elucidate the conditions under which the extreme electromagnetic environment generated by a plasmon may deform the one- and many-body electronic structure of a molecule when both systems are resonantly coexcited. Numerical simulations based upon our formalism demonstrate the importance of these effects both within a model calculation of pyrazine immersed in a broadband plasmonic environment as well as within a first-principles treatment of the indigo molecule located in the computed electromagnetic hot spot of a silver nanotrimer aggregate. An experiment capable of measuring the predicted distortions of a molecule's electronic structure is proposed, based upon the correlation of optical and electron spectroscopies. The results of this work bear impact upon a variety of plasmon-enhanced molecular spectroscopies as well as upon the emerging field of plasmon-mediated hot-electron-driven chemistry, where controlling the molecule's energetics relative to the metal is of crucial importance.

ASSOCIATED CONTENT

Supporting Information

Details of the derivation of $Tr\boldsymbol{\Sigma}_0 = 2Tr\boldsymbol{\Sigma}_0\boldsymbol{\rho}$ used in eq 13. This material is available free of charge via the Internet at http://pubs.acs.org.

AUTHOR INFORMATION

Corresponding Author

*E-mail: masiello@chem.washington.edu.

Notes

The authors declare no competing financial interest.

ACKNOWLEDGMENTS

This work was supported by the National Science Foundation's CAREER program under award number CHE-1253775 (D.J.M.), by a National Science Foundation Graduate Research Fellowship under grant no. DGE-0718124 (J.P.L.), and by the National Science Foundation's NNIN REU program (A.B.L.).

REFERENCES

(1) Purcell, E. M. Spontaneous emission probabilities at radio frequencies. *Phys. Rev.* **1946**, *69*, 681.

(2) Chance, R. R.; Prock, A.; Silbey, R. Molecular fluorescence and energy transfer near interfaces. *Adv. Chem. Phys.* **1978**, *37*, 1.
(3) Anger, P.; Bharadwaj, P.; Novotny, L. Enhancement and quenching of single-molecule fluorescence. *Phys. Rev. Lett.* **2006**, *96*, 113002.
(4) Chen, Y.; Munechika, K.; Ginger, D. S. Dependence of fluorescence intensity on the spectral overlap between fluorophores and plasmon resonant single silver nanoparticles. *Nano Lett.* **2007**, *7*, 690.
(5) Munechika, K.; Chen, Y.; Tillack, A. F.; Kulkarni, A. P.; Plante, I. J.-L.; Munro, A. M.; Ginger, D. S. Spectral control of plasmonic emission enhancement from quantum dots near single silver nanoprisms. *Nano Lett.* **2010**, *10*, 2598−2603.
(6) Gersten, J.; Nitzan, A. Electromagnetic theory of Raman scattering by molecules adsorbed on rough surfaces. *J. Chem. Phys.* **1980**, *73*, 3023.
(7) Jackson, J. D. *Classical Electrodynamics*, 3rd ed.; J. Wiley & Sons: New York, 1999.
(8) Masiello, D. J.; Schatz, G. C. Many-body theory of surface-enhanced Raman scattering. *Phys. Rev. A* **2008**, *78*, 042505.
(9) Milonni, P. W.; Smith, A. van der Waals dispersion forces in electromagnetic fields. *Phys. Rev. A* **1996**, *53*, 3484−3489.
(10) Perreault, J. D.; Bhattacharya, M.; Lonij, V. P. A.; Cronin, A. D. Modifying atom−surface interactions with optical fields. *Phys. Rev. A* **2008**, *77*, 043406.
(11) Corni, S.; Tomasi, J. Enhanced response properties of a chromophore physisorbed on a metal particle. *J. Chem. Phys.* **2001**, *114*, 3739.
(12) Sánchez-González, Á.; Corni, S.; Mennucci, B. Surface-enhanced fluorescence within a metal nanoparticle array: The role of solvent and plasmon couplings. *J. Phys. Chem. C* **2011**, *115*, 5450−5460.
(13) Jensen, L.; Autschbach, J.; Schatz, G. C. Finite lifetime effects on the polarizability within time-dependent density-functional theory. *J. Chem. Phys.* **2005**, *122*, 224115.
(14) Jensen, L.; Zhao, L.; Autschbach, J.; Schatz, G. C. Theory and method for calculating resonance Raman scattering from resonance polarizability derivatives. *J. Chem. Phys.* **2005**, *123*, 174110.
(15) Zhao, L. L.; Jensen, L.; Schatz, G. C. Pyridine−Ag_2O cluster: A model system for studying surface-enhanced Raman scattering. *J. Am. Chem. Soc.* **2006**, *128*, 2911.
(16) Aikens, C. M.; Schatz, G. C. TDDFT studies of absorption and SERS spectra of pyridine interacting with Au_{20}. *J. Phys. Chem. A* **2006**, *110*, 13317.
(17) Jensen, L.; Zhao, L. L.; Schatz, G. C. Size-dependence of the enhanced Raman scattering of pyridine adsorbed on Ag_n (n = 2−8, 20) clusters. *J. Phys. Chem. C* **2007**, *111*, 4756.
(18) Morton, S. M.; Jensen, L. A discrete interaction model/quantum mechanical method for describing response properties of molecules adsorbed on metal nanoparticles. *J. Chem. Phys.* **2010**, *133*, 074103.
(19) Morton, S. M.; Jensen, L. A discrete interaction model/quantum mechanical method to describe the interaction of metal nanoparticles and molecular absorption. *J. Chem. Phys.* **2011**, *135*, 134103.
(20) Chen, H.; McMahon, J. M.; Ratner, M. A.; Schatz, G. C. Classical electrodynamics coupled to quantum mechanics for calculation of molecular optical properties: A RT-TDDFT/FDTD approach. *J. Phys. Chem. C* **2010**, *114*, 14384−14392.
(21) Mullin, J.; Schatz, G. C. Combined linear response quantum mechanics and classical electrodynamics (QM/ED) method for the calculation of surface-enhanced Raman spectra. *J. Phys. Chem. A* **2012**, *116*, 1931−1938.
(22) Giannini, V.; Fernández-Domínguez, A. I.; Heck, S. C.; Maier, S. A. Plasmonic nanoantennas: Fundamentals and their use in controlling the radiative properties of nanoemitters. *Chem. Rev.* **2011**, *111*, 3888−3912.
(23) Morton, S. M.; Silverstein, D. W.; Jensen, L. Theoretical studies of plasmonics using electronic structure methods. *Chem. Rev.* **2011**, *111*, 3962−3994.
(24) Neuhauser, D.; Lopata, K. Molecular nanopolaritonics: Cross manipulation of near-field plasmons and molecules. I. Theory and application to junction control. *J. Chem. Phys.* **2007**, *127*, 154715.
(25) Lopata, K.; Neuhauser, D. Nonlinear nanopolaritonics: Finite-difference time-domain Maxwell−Schrödinger simulation of molecule-assisted plasmon transfer. *J. Chem. Phys.* **2009**, *131*, 014701.
(26) Coomar, A.; Arntsen, C.; Lopata, K. A.; Pistinner, S.; Neuhauser, D. Near-field: A finite-difference time-dependent method for simulation of electrodynamics on small scales. *J. Chem. Phys.* **2011**, *135*, 084121.
(27) Watson, M. A.; Rappoport, D.; Lee, E. M. Y.; Olivares-Amaya, R.; Aspuru-Guzik, A. Electronic structure calculations in arbitrary electrostatic environments. *J. Chem. Phys.* **2012**, *136*, 024101.
(28) Manjavacas, A.; García de Abajo, F. J.; Nordlander, P. Quantum plexcitonics: Strongly interacting plasmons and excitons. *Nano Lett.* **2011**, *11*, 2318.
(29) Wu, X.; Gray, S. K.; Pelton, M. Quantum-dot-induced transparency in a nanoscale plasmonic resonator. *Opt. Express* **2010**, *18*, 23633−23645.
(30) Masiello, D. J.; Schatz, G. C. On the linear response and scattering of an interacting molecule−metal system. *J. Chem. Phys.* **2010**, *132*, 064102.
(31) Fetter, A. L.; Walecka, J. D. *Quantum Theory of Many-Particle Systems*; McGraw-Hill: New York, 1971.
(32) Linderberg, J.; Öhrn, Y. *Propagators in Quantum Chemistry*; John Wiley and Sons: Hoboken, NJ, 1973.
(33) Kadanoff, L. P., Baym, G. (Eds.) *Quantum Statistical Mechanics*; Westview Press: Boulder, CO, 1994.
(34) Møller, C.; Plesset, M. S. Note on an approximation treatment for many-electron systems. *Phys. Rev.* **1934**, *46*, 618.
(35) Hartree, D. R. The wave mechanics of an atom with a non-Coulomb central field. Parts I−III. *Proc. Cambridge Philos. Soc.* **1928**, *24* (89−111), 426−437.
(36) Faddeev, L. D.; Khalfin, L. A.; Komarov, I. V. *V. A. Fock—Selected Works: Quantum Mechanics and Quantum Field Theory*; Chapman & Hall/CRC: Boca Raton, FL, 2004.
(37) Hohenberg, P.; Kohn, W. Inhomogeneous electron gas. *Phys. Rev.* **1964**, *136*, B864−B871.
(38) Kohn, W.; Sham, L. J. Self-consistent equations including exchange and correlation effects. *Phys. Rev.* **1965**, *140*, A1133−A1138.
(39) Mukamel, S. Causal versus noncausal description of nonlinear wave mixing: Resolving the damping-sign controversy. *Phys. Rev. A* **2007**, *76*, 021803(R).
(40) Bialynicki-Birula, I.; Sowiński, T. Quantum electrodynamics of qubits. *Phys. Rev. A* **2007**, *76*, 062106.
(41) Bogoliubov, N. N. On the theory of superfluidity. *J. Phys. (Moscow)* **1947**, *11*, 23.
(42) Gray, S. K.; Kupka, T. Propagation of light in metallic nanowire arrays: Finite-difference time-domain studies of silver cylinders. *Phys. Rev. B* **2003**, *68*, 45415.
(43) Holleboom, L. J.; Snijders, J. G.; Baerends, E. J. Natural energy orbitals and the one-particle Green's function. *Int. J. Quantum Chem.* **1988**, *34*, 289.
(44) Holleboom, L. J.; Snijders, J. G. Green-function calculations using non-Hartree Fock orbitals. *Int. J. Quantum Chem.* **1992**, *43*, 259−272.
(45) Shao, Y.; et al. Advances in quantum chemical methods and algorithms in the Q-Chem 3.0 program package. *Phys. Chem. Chem. Phys.* **2006**, *8*, 3172.
(46) Draine, B. T.; Flatau, P. J. Discrete-dipole approximation for scattering calculations. *J. Opt. Soc. Am. A* **1994**, *11*, 1491.
(47) Lynch, D. W.; Hunter, W. R. In *Handbook of Optical Constants of Solids*; Palik, E. D., Ed.; Academic Press: New York, 1985.
(48) Yurtsever, A.; Zewail, A. H. Direct visualization of near-fields in nanoplasmonics and nanophotonics. *Nano Lett.* **2012**, *12*, 3334−3338.
(49) Yurtsever, A.; van der Veen, R. M.; Zewail, A. H. Subparticle ultrafast spectrum imaging in 4D electron microscopy. *Science* **2012**, *335*, 59−64.

(50) Mirsaleh-Kohan, N.; Iberi, V.; Simmons, P. D.; Bigelow, N. W.; Vaschillo, A.; Rowland, M. M.; Best, M. D.; Pennycook, S. J.; Masiello, D. J.; Guiton, B. S.; Camden, J. P. Single-molecule surface-enhanced Raman scattering: Can STEM/EELS image electromagnetic hot spots? *J. Phys. Chem. Lett.* **2012**, *3*, 2303−2309.
(51) Bigelow, N. W.; Vaschillo, A.; Iberi, V.; Camden, J. P.; Masiello, D. J. Characterization of the electron- and photon-driven plasmonic excitations of metal nanorods. *ACS Nano* **2012**, *6*, 7497−7504.
(52) Guiton, B. S.; Iberi, V.; Li, S.; Leonard, D. N.; Parish, C. M.; Kotula, P. G.; Varela, M.; Schatz, G. C.; Pennycook, S. J.; Camden, J. P. Correlated optical measurements and plasmon mapping of silver nanorods. *Nano Lett.* **2011**, *11*, 3482−3488.
(53) Nellist, P. D.; Pennycook, S. J. Subangstrom resolution by underfocused incoherent transmission electron microscopy. *Phys. Rev. Lett.* **1998**, *81*, 4156.
(54) Arenal, R.; Stéphan, O.; Kociak, M.; Taverna, D.; Loiseau, A.; Colliex, C. Electron energy loss spectroscopy measurement of the optical gaps on individual boron nitride single-walled and multiwalled nanotubes. *Phys. Rev. Lett.* **2005**, *95*, 127601.
(55) Couillard, M.; Kociak, M.; Stéphan, O.; Botton, G. A.; Colliex, C. Multiple-interface coupling effects in local electron-energy-loss measurements of band gap energies. *Phys. Rev. B* **2007**, *76*, 165131.

Molecular Electronic Structure in a Plasmonic Environment: Elucidating the Quantum Image Interaction

Jonathan P. Litz, Ryan P. Brewster, Alexander B. Lee, and David J. Masiello*

Department of Chemistry, University of Washington, Seattle, Washington 98195-1700, USA

E-mail: masiello@chem.washington.edu

Supporting Information

In Eq. 13 of the main text, we substitute $\mathrm{Tr}\hbar\boldsymbol{\Sigma}_0 = 2\mathrm{Tr}\hbar\boldsymbol{\Sigma}_0\boldsymbol{\rho}$. We do this for consistency between the noninteracting part of the ground-state electronic energy and the self energy. This relation is analytically exact at first order in the Dyson expansion and, through numerical solution of the infinite-order expression, is found to be correct to at least 10^{-5} au (10^{-4} au) away from (close to) molecular resonances. In addition this relation is physically intuitive.

Here we will show analytically that $\mathrm{Tr}\hbar\boldsymbol{\Sigma}_0 = 2\mathrm{Tr}\hbar\boldsymbol{\Sigma}_0\boldsymbol{\rho}$ at first order in the Dyson expansion, where $\tilde{\mathscr{G}}(z) = \tilde{\mathbf{G}}(z)$ and $\boldsymbol{\rho} = \boldsymbol{\rho}^0$. Let us begin by solving for $\mathrm{Tr}\hbar\boldsymbol{\Sigma}_0^{(1)}$:

$$\begin{aligned}\mathrm{Tr}\hbar\boldsymbol{\Sigma}_0^{(1)} &= \oint_{\mathrm{IP}} \sum_p \tilde{G}_{pp}(z)\tilde{\Sigma}^{\bigstar(2)}_{pp}(z)\frac{d(\hbar z)}{\pi i} \\ &= \oint_{\mathrm{IP}} \sum_p \left[\frac{\rho_p^0}{z-\varepsilon_p^0/\hbar - i\eta} + \frac{1-\rho_p^0}{z-\varepsilon_p^0/\hbar + i\eta}\right] \times \\ &\qquad \left[\sum_i \frac{\boldsymbol{\mu}_{pi}\cdot\mathbf{E}^{(-)}\mathbf{E}^{(+)}\cdot\boldsymbol{\mu}_{ip}}{\hbar z - \hbar\omega - \varepsilon_i^0 - i\eta} + \sum_a \frac{\boldsymbol{\mu}_{pa}\cdot\mathbf{E}^{(+)}\mathbf{E}^{(-)}\cdot\boldsymbol{\mu}_{ap}}{\hbar z + \hbar\omega - \varepsilon_a^0 + i\eta}\right]\frac{dz}{\pi i}.\end{aligned} \tag{1}$$

*To whom correspondence should be addressed

By Cauchy's residue theorem, Eq. (1) becomes

$$\mathrm{Tr}\hbar\boldsymbol{\Sigma}_0^{(1)} = 4\sum_{ia}\frac{\boldsymbol{\mu}_{ia}\cdot\mathbf{E}^{(-)}\mathbf{E}^{(+)}\cdot\boldsymbol{\mu}_{ai}}{\varepsilon_i^0+\hbar\omega-\varepsilon_a^0+2i\eta}. \tag{2}$$

Let us now look at $2\mathrm{Tr}\hbar\boldsymbol{\Sigma}_0^{(1)}\boldsymbol{\rho}^0$:

$$\begin{aligned}2\mathrm{Tr}\hbar\boldsymbol{\Sigma}_0^{(1)}\boldsymbol{\rho}^0 &= 2\oint_{\mathrm{IP}}\sum_j \tilde{G}_{jj}(z)\tilde{\Sigma}^{\bigstar(2)}_{jj}(z)\frac{d(\hbar z)}{\pi i}\\ &= 2\oint_{\mathrm{IP}}\sum_j\left[\frac{\rho_j^0}{z-\varepsilon_j^0/\hbar-i\eta}+\frac{1-\rho_j^0}{z-\varepsilon_j^0/\hbar+i\eta}\right]\times\\ &\qquad\left[\sum_i\frac{\boldsymbol{\mu}_{ji}\cdot\mathbf{E}^{(-)}\mathbf{E}^{(+)}\cdot\boldsymbol{\mu}_{ij}}{\hbar z-\hbar\omega-\varepsilon_i^0-i\eta}+\sum_a\frac{\boldsymbol{\mu}_{ja}\cdot\mathbf{E}^{(+)}\mathbf{E}^{(-)}\cdot\boldsymbol{\mu}_{aj}}{\hbar z+\hbar\omega-\varepsilon_a^0+i\eta}\right]\frac{dz}{\pi i}.\end{aligned} \tag{3}$$

Through Cauchy's residue theorem, Eq. (3) becomes

$$2\mathrm{Tr}\hbar\boldsymbol{\Sigma}_0^{(1)}\boldsymbol{\rho}^0 = 4\sum_{ia}\frac{\boldsymbol{\mu}_{ia}\cdot\mathbf{E}^{(-)}\mathbf{E}^{(+)}\cdot\boldsymbol{\mu}_{ai}}{\varepsilon_i^0+\hbar\omega-\varepsilon_a^0+2i\eta}. \tag{4}$$

Therefore at first order, $\mathrm{Tr}\hbar\boldsymbol{\Sigma}_0 = 2\mathrm{Tr}\hbar\boldsymbol{\Sigma}_0\boldsymbol{\rho}$.

This substitution is physically intuitive because it states that the net shift in occupied orbital energies is equal to the net shift in virtual orbital energies upon image-dressing the molecule. For each pairwise interaction of an occupied and virtual orbital, both orbitals will have the same energetic shift. Ultimately, the total change in each occupied (unoccupied) orbital energy will be equal to the superposition of the orbital's pairwise image interaction energy with each unoccupied (occupied) orbital as shown in Eqs. (2) and (4) in the SI.

Appendix A

TWO POPULATION DEPLETION MODEL CODE

2pop_depletion

November 17, 2015

In [1]:
```
#Jonathan P. Litz
#November 17, 2015
#This is the code used to generate the MCMC traces for the 2-population model
#in Litz, Thakar, Portet, and Keller 2015 (Biophysical Journal)

%matplotlib inline
import matplotlib.pyplot as plt
import pandas as pd
import numpy as np
import pymc

#list of lipids we have area data for
lipidList = ['SOPC', 'DMPC', 'DOPC']

#dict mapping lipids to max time of experiment
maxTimeDict = {'SOPC': 102, 'DMPC': 302, 'DOPC': 302}

#area per molecule is approximated as exponentially
#decreasing with increasing \chi_C
areaParamsDict = {'SOPC': (38.5, 26.8, 2.9),
            'DMPC': (38.1, 21.0, 5.1),
            'DOPC': (36.5, 31.1, 2.2)}

class Lipid:
    def __init__(self, name):
        #String representing the name of the lipid. e.g., 'DOPC'
        self.name = name

        self.maxTime = maxTimeDict[ name ]
        self.areaParams = areaParamsDict[ name ]

    def area_per_molecule(self, mol_frac_chol):
        p1, p2, p3 = self.areaParams
        return p1 + p2 * np.exp( -p3 * mol_frac_chol )

#This prompts you for the name of the lipid being studied
lipidChosen = raw_input('Which lipid? Your choices are
                            DOPC, SOPC, DMPC (case matters): ')

while lipidChosen not in lipidList:
    lipidChosen = raw_input('No data for this lipid. Which lipid?
                        Your choices are DOPC, SOPC, DMPC (case matters):')
```

```
        lipid = Lipid(lipidChosen)
```

```
Which lipid? Your choices are DOPC, SOPC, DMPC (case matters): DMPC
```

```
In [2]: def get_dataframe(lipid):
            data = pd.read_table('depletionData/' + lipid.name + '.csv'
                                 , sep=',', header=None)

            #times is a list from 5 to maxTime counting by 2s
            times = np.arange(5., lipid.maxTime, 2.)
            times = np.insert(times, 0, 0.)

            #this is the initial mole fraction of cholesterol.
            #It can be varied (but this might break some assumptions in the code)
            mol_frac_chol_0 = 0.66

            flattenData = []
            flattenTimes = []
            flattenRuns = []
            flattenMolFrac = []

            for i in range(len(data.columns)):
                for j in range(len(times)):
                    flattenRuns.append( i )
                    flattenData.append( data[i][j] )
                    flattenTimes.append( times[j] )
                    flattenMolFrac.append( mol_frac_chol_0 )

            dataDict = {'area_remaining': flattenData, 'time': flattenTimes,
                        'mol_frac_chol_0': flattenMolFrac}

            frame = pd.DataFrame(dataDict, index = flattenRuns)

            return frame, data.mean(1), data.std(1), times

        def calculate_mol_frac_chol( lipid, t, chi_0, chi_s, k_s, k_f):
            """Calculate \chi_C at time t given a lipid, fitting parameters,
                    and the initial \chi_C"""
            n_lipid_over_n_chol = (1 - chi_0) / (chi_s * np.exp(-k_s * t) +
                                                 (chi_0 - chi_s) * np.exp(-k_f * t))
            chi_C = 1. / (n_lipid_over_n_chol + 1.)

            return chi_C

        def calculate_area_remaining( lipid, t, chi_0, chi_s, k_s, k_f ):
            """Calculate the area remaining at time t given a lipid,
                fitting parameters, and the initial \chi_C"""
            chi_C = calculate_mol_frac_chol(lipid, t, chi_0, chi_s, k_s, k_f)
            avg_area_ratio = lipid.area_per_molecule( chi_C ) /
                                     lipid.area_per_molecule( chi_0 )

            return ( 1 - chi_0 + chi_s * np.exp(-k_s * t) +
                        (chi_0 - chi_s) * np.exp(-k_f * t) ) * avg_area_ratio

        def calculate_depletion_coefficient( lipid, t, chi_0, chi_s, k_s, k_f):
```

```
        """Calculate the depletion coefficient at time t given a lipid,
            fitting parameters, and the initial \chi_C"""
        numerator = k_s * chi_s * np.exp(-k_s * t) +
                        k_f * (chi_0 - chi_s) * np.exp(-k_f * t)
        denominator = chi_s * np.exp(-k_s * t) + (chi_0 - chi_s) * np.exp(-k_f * t)
        return numerator / denominator

    def save_results( lipid, results ):
        resultsFrame = pd.DataFrame(results).transpose()
        resultsFrame.columns = ['chi_s', 'k_s', 'k_f']
        resultsFrame.to_pickle( lipid.name + '.bi_fit' )
```

In [85]:
```
frame, means, stdevs, times = get_dataframe(lipid)

mol_frac_chol_0 = frame['mol_frac_chol_0'].values[0]
tdata           = frame['time'].values
area_data       = frame['area_remaining'].values

# Define the variables needed for the routine, with uniform prior distributions
chi_s  = pymc.Uniform('chi_s', 0, mol_frac_chol_0)
k_f = pymc.Uniform('k_f', 0., 1.)
k_s = pymc.Uniform('k_s', 0., k_f)

@pymc.stochastic(observed=False)
def sigma(value=1):
    return -np.log(abs(value))
#A uniform prior for sigma works as well

# Define the form of the model and likelihood
@pymc.deterministic
def bi_area_model(lipid=lipid, time=tdata, mol_frac_chol_0=mol_frac_chol_0,
                      chi_s=chi_s, k_s=k_s, k_f=k_f):
    return calculate_area_remaining( lipid, time, mol_frac_chol_0,
                                         chi_s, k_s, k_f )

#This tells pymc to do least squares
#(expect a normal distribution of errors around the model)
bi_fit = pymc.Normal('bi_fit', mu = bi_area_model,
                           tau = 1. / sigma ** 2, observed=True, value=area_data)

#package the full model in a dictionary (this dict is then handed to pymc)
bi_model = dict(chi_s=chi_s, k_s=k_s, k_f=k_f, sigma=sigma,
                    bi_area_model=bi_area_model, bi_fit=bi_fit)
bi_mcmc = pymc.MCMC(bi_model)

#draw 100000 sets of parameters from the MCMC
bi_mcmc.sample(iter=100000, burn=20000)
#bi_mcmc.sample(iter=10000, burn=5000) #just for debugging, it runs faster

# extract the traces and plot the results
bi_pymc_trace = [bi_mcmc.trace('chi_s')[:],
                 bi_mcmc.trace('k_s')[:],
                 bi_mcmc.trace('k_f')[:]]
                # bi_mcmc.trace('sigma')[:]]
```

```
        save_results_on = False #turn this on the write the calculated results to file
        if save_results_on == True:
            save_results(lipid, bi_pymc_trace)
```

```
[-----------------100%-----------------] 100000 of 100000 complete in 363.5 sec
```

BIBLIOGRAPHY

[1] Litz, J. P.; Camden, J. P.; Masiello, D. J. *J. Phys. Chem. Lett.* **2011**, *2*, 1695–1700.

[2] Weber, M. L.; Litz, J. P.; Masiello, D. J.; Willets, K. A. *ACS Nano* **2012**, *6*, 1839–1848.

[3] Litz, J. P.; Brewster, R. P.; Lee, A. B.; Masiello, D. J. *J. Phys. Chem. C* **2013**, *117*, 12249–12257.

[4] Litz, J. P.; Thakkar, N.; Portet, T.; Keller, S. L. *Biophys. J.* **2015**, In Press.

[5] Bleecker, J. V.; Cox, P. A.; Foster, R. N.; Litz, J. P.; Blosser, M. C.; Keller, S. L. *J. Phys. Chem. B* **2015**, Under Review.

[6] Morrison, K. C.; Litz, J. P.; Scherpelz, K. P.; Dossa, P. D.; Vosburg, D. A. *Org. Lett.* **2009**, *11*, 2217–2218.

[7] Karukstis, K. K.; Litz, J. P.; Garber, M. B.; Angell, L. M.; Korir, G. K. *Spectrochim. Acta. A. Mol. Biomol. Spectrosc.* **2010**, *75*, 1354–61.

[8] Wan, K. K.; Litz, J. P.; Vosburg, D. A. *Tetrahedron: Asymmetry* **2010**, *21*, 2425–2428.

[9] Nacsa, E. D.; Fielder, B. C.; Wetzler, S. P.; Srisuknimit, V.; Litz, J. P.; Van Vleet, M. J.; Quach, K.; Vosburg, D. A. *Synthesis (Stuttg).* **2015**, *47*, 2599–2602.

[10] Quehenberger, O. et al. *J. Lipid Res.* **2010**, *51*, 3299–3305.

[11] Fahy, E. et al. *J. Lipid Res.* **2005**, *46*, 839–862.

[12] van Meer, G.; Voelker, D. R.; Feigenson, G. W. *Nat. Rev. Mol. Cell Biol.* **2008**, *9*, 112–124.

[13] Ejsing, C. S.; Sampaio, J. L.; Surendranath, V.; Duchoslav, E.; Ekroos, K.; Klemm, R. W.; Simons, K.; Shevchenko, A. *Proc. Natl. Acad. Sci.* **2009**, *106*, 2136–2141.

[14] van Meer, G.; de Kroon, A. I. P. M. *J. Cell Sci.* **2011**, *124*, 5–8.

[15] Ekroos, K.; Ejsing, C. S.; Bahr, U.; Karas, M.; Simons, K.; Shevchenko, A. *J. Lipid Res.* **2003**, *44*, 2181–2192.

[16] Huang, J.; Buboltz, J. T.; Feigenson, G. W. *BBA-Biomembranes* **1999**, *1417*, 89–100.

[17] Stevens, M. M.; Honerkamp-Smith, A. R.; Keller, S. L. *Soft Matter* **2010**, *6*, 5882–5890.

[18] Veatch, S. L.; Keller, S. L. *Biochim. Biophys. Acta - Mol. Cell Res.* **2005**, *1746*, 172–185.

[19] Veatch, S. L.; Keller, S. L. *Biophys. J.* **2003**, *85*, 3074–3083.

[20] Seelig, A.; Seelig, J. *Biochemistry* **1974**, *13*, 4839–4845.

[21] Mills, T. T.; Toombes, G. E. S.; Tristram-Nagle, S.; Smilgies, D.-M.; Feigenson, G. W.; Nagle, J. F. *Biophys. J.* **2008**, *95*, 669–681.

[22] Tsamaloukas, A.; Szadkowska, H.; Slotte, P. J.; Heerklotz, H. *Biophys. J.* **2005**, *89*, 1109–1119.

[23] Huang, Z.; London, E. *Langmuir* **2013**, *29*, 14631–14638.

[24] Steck, T. L.; Ye, J.; Lange, Y. *Biophys. J.* **2002**, *83*, 2118–2125.

[25] Hamilton, J. A. *Curr. Opin. Lipidol.* **2003**, *14*, 263–271.

[26] Bruckner, R. J.; Mansy, S. S.; Ricardo, A.; Mahadevan, L.; Szostak, J. W. *Biophys. J.* **2009**, *97*, 3113–3122.

[27] Jo, S.; Rui, H.; Lim, J. B.; Klauda, J. B.; Im, W. *J. Phys. Chem. B* **2010**, *114*, 13342–13348.

[28] Zhang, L.; Granick, S. *J. Chem. Phys.* **2005**, *123*, 3–6.

[29] Pan, J.; Tristram-Nagle, S.; Nagle, J. F. *Phys Rev E* **2009**, *80*, 021931.

[30] Kučerka, N.; Nieh, M. P.; Katsaras, J. *BBA-Biomembranes* **2011**, *1808*, 2761–2771.

[31] McIntosh, T. J.; Simon, S. A. *Biochemistry* **1986**, *25*, 4058–4066.

[32] Radhakrishnan, A.; McConnell, H. M. *Biochemistry* **2000**, *39*, 8119–8124.

[33] Olsen, B. N.; Bielska, A. A.; Lee, T.; Daily, M. D.; Covey, D. F.; Schlesinger, P. H.; Baker, N. A.; Ory, D. S. *Biophys. J.* **2013**, *105*, 1838–1847.

[34] Lange, Y.; Ye, J.; Steck, T. L. *J. Biol. Chem.* **2005**, *280*, 36126–36131.

[35] Lange, Y.; Steck, T. L. *Prog. Lipid Res.* **2008**, *47*, 319–332.

[36] Haynes, M. P.; Phillips, M. C.; Rothblat, G. H. *Biochemistry* **2000**, *39*, 4508–4517.

[37] Ramshaw, J. D. *J. Chem. Educ.* **1995**, *72*, 601–603.

[38] Radhakrishnan, A.; Anderson, T. G.; McConnell, H. M. *P. Natl. Acad. Sci. USA* **2000**, *97*, 12422–12427.

[39] McConnell, H. M.; Radhakrishnan, A. *BBA-Biomembranes* **2003**, *1610*, 159–173.

[40] Lange, Y.; Ye, J.; Steck, T. L. *P. Natl. Acad. Sci. USA* **2004**, *101*, 11664–11667.

[41] Lange, Y.; Ory, D. S.; Ye, J.; Lanier, M. H.; Hsu, F.-F.; Steck, T. L. *J. Biol. Chem.* **2008**, *283*, 1445–1455.

[42] Lange, Y.; Ye, J.; Duban, M.-E.; Steck, T. L. *Biochemistry* **2009**, *48*, 8505–8515.

[43] Lange, Y.; Steck, T. L.; Ye, J.; Lanier, M. H.; Molugu, V.; Ory, D. *J. Lipid Res.* **2009**, *50*, 1881–1888.

[44] Steck, T. L.; Lange, Y. *Trends Cell Biol.* **2010**, *20*, 680–687.

[45] Das, A.; Brown, M. S.; Anderson, D. D.; Goldstein, J. L.; Radhakrishnan, A. *eLife* **2014**, *3*, e02882.

[46] Sokolov, A.; Radhakrishnan, A. *J. Biol. Chem.* **2010**, *285*, 29480–29490.

[47] Lange, Y.; Tabei, S. M. A.; Ye, J.; Steck, T. L. *Biochemistry* **2013**, *52*, 6950–6959.

[48] Gay, A.; Rye, D.; Radhakrishnan, A. *Biophys. J.* **2015**, *108*, 1459–1469.

[49] Das, A.; Goldstein, J. L.; Anderson, D. D.; Brown, M. S.; Radhakrishnan, A. *P. Natl. Acad. Sci. USA* **2013**, *110*, 10580–10585.

[50] Lange, Y.; Steck, T. *Trends Cell Biol.* **1996**, *8924*, 205–208.

[51] Lange, Y.; Ye, J.; Steck, T. L. *PLoS One* **2014**, *9*, e98482.

[52] Kris-Etherton, P. *Am. J. Clin. Nutr.* **1997**, *65S*, 1628S – 1644S.

[53] Silvius, J. R. *BBA-Biomembranes* **2003**, *1610*, 174–183.

[54] Nelson, L. D.; Johnson, A. E.; London, E. *J. Biol. Chem.* **2008**, *283*, 4632–4642.

[55] Flanagan, J. J.; Tweten, R. K.; Johnson, A. E.; Heuck, A. P. *Biochemistry* **2009**, *48*, 3977–3987.

[56] Moe, P. C.; Heuck, A. P. *Biochemistry* **2010**, *49*, 9498–9507.

[57] Wang, M. M.; Olsher, M.; Sugár, I. P.; Chong, P. L. G. *Biochemistry* **2004**, *43*, 2159–2166.

[58] Ali, M. R.; Cheng, K. H.; Huang, J. *P. Natl. Acad. Sci. USA* **2007**, *104*, 5372–5377.

[59] Johnson, B. B.; Moe, P. C.; Wang, D.; Rossi, K.; Trigatti, B. L.; Heuck, A. P. *Biochemistry* **2012**, *51*, 3373–3382.

[60] Beattie, M. E.; Veatch, S. L.; Stottrup, B. L.; Keller, S. L. *Biophys. J.* **2005**, *89*, 1760–1768.

[61] Yancey, P. G.; Rodrigueza, W. V.; Kilsdonk, E. P. C.; Stoudt, G. W.; Johnson, W. J.; Phillips, M. C.; Rothblat, G. H. *J. Biol. Chem.* **1996**, *271*, 16026–16034.

[62] Melzak, K.; Melzak, S.; Gizeli, E.; Toca-Herrera, J. *Materials (Basel).* **2012**, *5*, 2306–2325.

[63] Mohwald, H. In *Structure and Dynamics of Membranes*; Lipowsky, R., Sackmann, E., Eds.; Elsevier: Amsterdam, 1995; pp 161–212.

[64] Kucerka, N.; Nagle, J. F.; Sachs, J. N.; Feller, S. E.; Pencer, J.; Jackson, A.; Katsaras, J. *Biophys. J.* **2008**, *95*, 2356–2367.

[65] Stottrup, B. L.; Stevens, D. S.; Keller, S. L. *Biophys. J.* **2005**, *88*, 269–276.

[66] Kilsdonk, E. P. C.; Yancey, P. G.; Stoudt, G. W.; Bangerter, F. W.; Johnson, W. J.; Phillips, M. C.; Rothblat, G. H. *J. Biol. Chem.* **1995**, *270*, 17250–17256.

[67] Beseničar, M. P.; Bavdek, A.; Kladnik, A.; Maček, P.; Anderluh, G. *BBA-Biomembranes* **2008**, *1778*, 175–184.

[68] Huang, J.; Feigenson, G. W. *Biophys. J.* **1999**, *76*, 2142–2157.

[69] Brzustowicz, M. R.; Cherezov, V.; Zerouga, M.; Caffrey, M.; Stillwell, W.; Wassall, S. R. *Biochemistry* **2002**, *41*, 12509–12519.

[70] Brzustowicz, M. R.; Cherezov, V.; Caffrey, M.; Stillwell, W.; Wassall, S. R. *Biophys. J.* **2002**, *82*, 285–298.

[71] Baykal-Caglar, E.; Hassan-Zadeh, E.; Saremi, B.; Huang, J. *BBA-Biomembranes* **2012**, *1818*, 2598–2604.

[72] Chong, P. L. *P. Natl. Acad. Sci. USA* **1994**, *91*, 10069–10073.

[73] Mason, R. P.; Tulenko, T. N.; Jacob, R. F. *BBA-Biomembranes* **2003**, *1610*, 198–207.

[74] Ziblat, R.; Kjaer, K.; Leiserowitz, L.; Addadi, L. *Angew. Chem. Int. Edit.* **2009**, *48*, 8958–8961.

[75] Raguz, M.; Mainali, L.; Widomska, J.; Subczynski, W. K. *BBA-Biomembranes* **2011**, *1808*, 1072–1080.

[76] Varsano, N.; Fargion, I.; Wolf, S. G.; Leiserowitz, L.; Addadi, L. *J. Am. Chem. Soc.* **2015**, *137*, 1601–1607.

[77] Mainali, L.; Raguz, M.; Subczynski, W. K. *J. Phys. Chem. B* **2013**, *117*, 8994–9003.

[78] Raguz, M.; Mainali, L.; Widomska, J.; Subczynski, W. K. *Chem. Phys. Lipids* **2011**, *164*, 819–829.

[79] Toppozini, L.; Meinhardt, S.; Armstrong, C. L.; Yamani, Z.; Kučerka, N.; Schmid, F.; Rheinstädter, M. C. *Phys. Rev. Lett.* **2014**, *113*, 228101.

[80] Ziblat, R.; Leiserowitz, L.; Addadi, L. *J. Am. Chem. Soc.* **2010**, *132*, 9920–9927.

[81] Barrett, M. A.; Zheng, S.; Toppozini, L. A.; Alsop, R. J.; Dies, H.; Wang, A.; Jago, N.; Moore, M.; Rheinstädter, M. C. *Soft Matter* **2013**, *9*, 9342–9351.

[82] Hung, W.-C.; Lee, M.-T.; Chen, F.-Y.; Huang, H. W. *Biophys. J.* **2007**, *92*, 3960–3967.

[83] Sugár, I. P.; Chong, P. L. G. *J. Am. Chem. Soc.* **2012**, *134*, 1164–1171.

[84] Ohvo-Rekilä, H.; Ramstedt, B.; Leppimäki, P.; Slotte, J. P. *Prog. Lipid Res.* **2002**, *41*, 66–97.

[85] Silvius, J. R. *Lipid-Protein Interactions*; Wiley: New York, 1982.

[86] Marsh, D. *BBA-Biomembranes* **2010**, *1798*, 688–699.

[87] Hamai, C.; Cremer, P. S.; Musser, S. M. *Biophys. J.* **2007**, *92*, 1988–1999.

[88] Niu, S.-L.; Litman, B. J. *Biophys. J.* **2002**, *83*, 3408–3415.

[89] Anderson, T. G.; Tan, A.; Ganz, P.; Seelig, J. *Biochemistry* **2004**, *43*, 2251–2261.

[90] Schneider, C. A.; Rasband, W. S.; Eliceiri, K. W. *Nat. Methods* **2012**, *9*, 671–675.

[91] Patil, A.; Huard, D.; Fonnesbeck, C. J. *J. Stat. Softw.* **2010**, *35*, 1–81.

[92] Heftberger, P.; Kollmitzer, B.; Heberle, F. A.; Pan, J.; Rappolt, M.; Amenitsch, H.; Kučerka, N.; Katsaras, J.; Pabst, G. *J. Appl. Crystallogr.* **2014**, *47*, 173–180.

[93] Gallová, J.; Uhríková, D.; Kučerka, N.; Teixeira, J.; Balgavý, P. *Chem. Phys. Lipids* **2010**, *163*, 765–770.

[94] Kučerka, N.; Pencer, J.; Nieh, M.-P.; Katsaras, J. *Eur. Phys. J. E* **2007**, *23*, 247–254.

[95] Kučerka, N.; Gallová, J.; Uhríková, D.; Balgavý, P.; Bulacu, M.; Marrink, S.-J.; Katsaras, J. *Biophys. J.* **2009**, *97*, 1926–1932.

[96] Koenig, B. W.; Gawrisch, K. *BBA-Biomembranes* **2005**, *1715*, 65–70.

[97] Greenwood, A. I.; Tristram-Nagle, S.; Nagle, J. F. *Chem. Phys. Lipids* **2006**, *143*, 1–10.

[98] Tristram-Nagle, S.; Liu, Y.; Legleiter, J.; Nagle, J. F. *Biophys. J.* **2002**, *83*, 3324–3335.

[99] Uhríková, D.; Rybár, P.; Hianik, T.; Balgavý, P. *Chem. Phys. Lipids* **2007**, *145*, 97–105.

[100] Fernandez, M. L.; West, K. L. *J. Nutr.* **2005**, *135*, 2075–2078.

[101] Baum, S. J.; Kris-Etherton, P. M.; Willett, W. C.; Lichtenstein, A. H.; Rudel, L. L.; Maki, K. C.; Whelan, J.; Ramsden, C. E.; Block, R. C. *J. Clin. Lipidol.* **2012**, *6*, 216–234.

[102] Dougherty, R. M.; Galli, C.; Ferro-Luzzi, A.; Iacono, J. M. *Am. J. Clin. Nutr.* **1987**, *45*, 443–455.

[103] Brown, M. S.; Goldstein, J. L. *Cell* **1997**, *89*, 331–340.

[104] Horton, J. D.; Goldstein, J. L.; Brown, M. S. *J. Clin. Invest.* **2002**, *109*, 1125–1131.

[105] Brown, M. S.; Goldstein, J. L. *J. Lipid Res.* **2008**, *50S*, S15–S27.

[106] Radhakrishnan, A.; Goldstein, J. L.; McDonald, J. G.; Brown, M. S. *Cell Metab.* **2008**, *8*, 512–521.

[107] Lange, Y.; Ye, J.; Rigney, M.; Steck, T. L. *J. Lipid Res.* **1999**, *40*, 2264–2270.

[108] Grosjean, K.; Mongrand, S.; Beney, L.; Simon-Plas, F.; Gerbeau-Pissot, P. *J. Biol. Chem.* **2015**, *290*, 5810–5825.

[109] Toulmay, A.; Prinz, W. A. *J. Cell Biol.* **2013**, *202*, 35–44.

[110] Wang, C.-W.; Miao, Y.-H.; Chang, Y.-S. *J. Cell Biol.* **2014**, *206*, 357–366.

[111] Veatch, S. L.; Polozov, I. V.; Gawrisch, K.; Keller, S. L. *Biophys. J.* **2004**, *86*, 2910–2922.

[112] Putzel, G. G.; Schick, M. *J. Phys. Condens. Matter* **2011**, *23*, 284101.

[113] Solomonov, I.; Weygand, M. J.; Kjaer, K.; Rapaport, H.; Leiserowitz, L. *Biophys. J.* **2005**, *88*, 1809–1817.

[114] Andersen, O. S.; Koeppe II, R. E. *Annu. Rev. Biophys. Biomol. Struct.* **2007**, *36*, 107–130.

[115] Phillips, R.; Ursell, T.; Wiggins, P.; Sens, P. *Nature* **2009**, *459*, 379–385.

[116] Heimburg, T. *Thermal Biophysics of Membranes*; Wiley-VCH: Weinheim, 2007.

[117] Simons, K.; Ikonen, E. *Nature* **1997**, *387*, 569–572.

[118] Simons, K.; Gerl, M. J. *Nat. Rev. Mol. Cell Biol.* **2010**, *11*, 688–699.

[119] Lewis, B. A.; Engelman, D. M. *J. Mol. Biol.* **1983**, *166*, 211–217.

[120] Petrache, H. I.; Dodd, S. W.; Brown, M. F. *Biophys. J.* **2000**, *79*, 3172–3192.

[121] Sperotto, M. M.; Mouritsen, O. G. *Eur. Biophys. J.* **1988**, *16*, 1–10.

[122] Ipsen, J. H.; Karlström, G.; Mourtisen, O.; Wennerström, H.; Zuckermann, M. *BBA-Biomembranes* **1987**, *905*, 162–172.

[123] Baumgart, T.; Hunt, G.; Farkas, E. R.; Webb, W. W.; Feigenson, G. W. *BBA-Biomembranes* **2007**, *1768*, 2182–2194.

[124] Sengupta, P.; Hammond, A.; Holowka, D.; Baird, B. *BBA-Biomembranes* **2008**, *1778*, 20–32.

[125] Stillwell, W. *An Introduction to Biological Membranes: From Bilayers to Rafts*; Academic Press: Amsterdam, 2013.

[126] Rinia, H. A.; Snel, M. M. E.; van der Eerden, J. P. J. M.; de Kruijff, B. *FEBS Lett.* **2001**, *501*, 92–96.

[127] Berquand, A.; Mingeot-Leclercq, M.-P.; Dufrêne, Y. F. *BBA-Biomembranes* **2004**, *1664*, 198–205.

[128] Giocondi, M. C.; Le Grimellec, C. *Biophys. J.* **2004**, *86*, 2218–2230.

[129] Jensen, M. H.; Morris, E. J.; Simonsen, A. C. *Langmuir* **2007**, *23*, 8135–8141.

[130] Chen, L.; Yu, Z.; Quinn, P. J. *BBA-Biomembranes* **2007**, *1768*, 2873–2881.

[131] García-Sáez, A. J.; Chiantia, S.; Schwille, P. *J. Biol. Chem.* **2007**, *282*, 33537–33544.

[132] Weise, K.; Triola, G.; Brunsveld, L.; Waldmann, H.; Winter, R. *J. Am. Chem. Soc.* **2009**, *131*, 1557–1564.

[133] Goksu, E. I.; Longo, M. L. *Langmuir* **2010**, *26*, 8614–8624.

[134] Marquês, J. T.; de Almeida, R. F. M.; Viana, A. S. *Soft Matter* **2012**, *8*, 2007–2016.

[135] Connell, S. D.; Heath, G.; Olmsted, P. D.; Kisil, A. *Faraday Discuss.* **2013**, *161*, 91–111.

[136] Nielsen, M. M. B.; Simonsen, A. C. *Langmuir* **2013**, *29*, 1525–1532.

[137] Heberle, F. A.; Petruzielo, R. S.; Pan, J.; Drazba, P.; Kučerka, N.; Standaert, R. F.; Feigenson, G. W.; Katsaras, J. *J. Am. Chem. Soc.* **2013**, *135*, 6853–6859.

[138] Kuzmin, P. I.; Akimov, S. A.; Chizmadzhev, Y. A.; Zimmerberg, J.; Cohen, F. S. *Biophys. J.* **2005**, *88*, 1120–1133.

[139] Wallace, E. J.; Hooper, N. M.; Olmsted, P. D. *Biophys. J.* **2006**, *90*, 4104–4118.

[140] Williamson, J.; Olmsted, P. *Biophys. J.* **2015**, *108*, 1963–1976.

[141] Lin, Q.; London, E. *J. Biol. Chem.* **2013**, *288*, 1340–1352.

[142] Ayuyan, A. G.; Cohen, F. S. *Biophys. J.* **2006**, *91*, 2172–2183.

[143] Honerkamp-Smith, A. R.; Cicuta, P.; Collins, M. D.; Veatch, S. L.; den Nijs, M.; Schick, M.; Keller, S. L. *Biophys. J.* **2008**, *95*, 236–246.

[144] Roux, A.; Cuvelier, D.; Nassoy, P.; Prost, J.; Bassereau, P.; Goud, B. *EMBO J.* **2005**, *24*, 1537–1545.

[145] Veatch, S. L.; Gawrisch, K.; Keller, S. L. *Biophys. J.* **2006**, *90*, 4428–4436.

[146] Veatch, S. L.; Soubias, O.; Keller, S. L.; Gawrisch, K. *P. Natl. Acad. Sci. USA* **2007**, *104*, 17650–17655.

[147] Davis, J. H.; Clair, J. J.; Juhasz, J. *Biophys. J.* **2009**, *96*, 521–539.

[148] Heberle, F. A.; Wu, J.; Goh, S. L.; Petruzielo, R. S.; Feigenson, G. W. *Biophys. J.* **2010**, *99*, 3309–3318.

[149] Ionova, I. V.; Livshits, V. A.; Marsh, D. *Biophys. J.* **2012**, *102*, 1856–1865.

[150] Bezlyepkina, N.; Gracià, R. S.; Shchelokovskyy, P.; Lipowsky, R.; Dimova, R. *Biophys. J.* **2013**, *104*, 1456–1464.

[151] Pan, J.; Cheng, X.; Heberle, F. A.; Mostofian, B.; Kučerka, N.; Drazba, P.; Katsaras, J. *J. Phys. Chem. B* **2012**, *116*, 14829–14838.

[152] Marquês, J. T.; Viana, A. S.; De Almeida, R. F. *BBA-Biomembranes* **2011**, *1808*, 405–414.

[153] Das, C.; Sheikh, K. H.; Olmsted, P. D.; Connell, S. D. *Phys. Rev. E* **2010**, *82*, 041920.

[154] Dufrêne, Y. F.; Barger, W. R.; Green, J.-B. D.; Lee, G. U. *Langmuir* **1997**, *13*, 4779–4784.

[155] Picas, L.; Rico, F.; Scheuring, S. *Biophys. J.* **2012**, *102*, L01–L03.

[156] Eaton, P.; West, P. *Atomic Force Microscopy*; Oxford University Press, 2010.

[157] Kucerka, N.; Perlmutter, J. D.; Pan, J.; Tristram-Nagle, S.; Katsaras, J.; Sachs, J. N. *Biophys. J.* **2008**, *95*, 2792–2805.

[158] Tahara, Y.; Fujiyoshi, Y. *Micron* **1994**, *25*, 141–149.

[159] Kaizuka, Y.; Groves, J. T. *Biophys. J.* **2004**, *86*, 905–912.

[160] Gordon, V. D.; Deserno, M.; Andrew, C. M. J.; Egelhaaf, S. U.; Poon, W. C. K. *EPL* **2008**, *84*, 48003.

[161] Zhao, J.; Wu, J.; Veatch, S. *Biophys. J.* **2013**, *104*, 825–834.

[162] Blosser, M. C.; Honerkamp-Smith, A. R.; Han, T.; Haataja, M.; Keller, S. L. *Biophys. J.* **2015**, In Press.

[163] Honerkamp-Smith, A. R.; Veatch, S. L.; Keller, S. L. *BBA-Biomembranes* **2009**, *1788*, 53–63.

[164] Stone, H. A.; Ajdari, A. *J. Fluid Mech.* **1998**, *369*, 151–173.

[165] Stottrup, B. L.; Veatch, S. L.; Keller, S. L. *Biophys. J.* **2004**, *86*, 2942–2950.

[166] Stanich, C. A.; Honerkamp-Smith, A. R.; Putzel, G. G.; Warth, C. S.; Lamprecht, A. K.; Mandal, P.; Mann, E.; Hua, T. A. D.; Keller, S. L. *Biophys. J.* **2013**, *105*, 444–454.

[167] Bhatia, T.; Husen, P.; Ipsen, J. H.; Bagatolli, L. A.; Simonsen, A. C. *BBA-Biomembranes* **2014**, *1838*, 2503–2510.

[168] Mihailescu, M.; Vaswani, R.; Jardón-Valadez, E.; Castro-Román, F.; Freites, J.; Worcester, D.; Chamberlin, A.; Tobias, D.; White, S. *Biophys. J.* **2011**, *100*, 1455–1462.

[169] Simons, K.; Sampaio, J. L. *Cold Spring Harb. Perspect. Biol.* **2011**, *3*, a004697.

[170] Pike, L. J. *J. Lipid Res.* **2009**, *50S*, S323–S328.

[171] Lehninger, A. L.; Nelson, D. L.; Cox, M. M. *Principles of Biochemistry, Fourth Edition*; W. H. Freeman: New York, 2005.

[172] Alberts, B.; Johnson, A.; Lewis, J.; Raff, M.; Roberts, K. *Molecular Biology of the Cell, 4th Edition*; Garland Science: New York, 2002.

[173] Lindsey, H.; Petersen, N.; Chan, S. I. *BBA-Biomembranes* **1979**, *555*, 147–167.

[174] Marsh, D. *CRC Handbook of Lipid Bilayers*; CRC Press: Boca Raton, FL, 1990.

[175] Angelova, M. I.; Soléau, S.; Méléard, P.; Faucon, J. F.; Bothorel, P. *Prog. Colloid Polym. Sci.* **1992**, *89*, 127–131.

[176] Blosser, M. C.; Starr, J. B.; Turtle, C. W.; Ashcraft, J.; Keller, S. L. *Biophys. J.* **2013**, *104*, 2629–2638.

[177] Johnson, S.; Stinson, B.; Go, M.; Carmona, L.; Reminick, J.; Fang, X.; Baumgart, T. *BBA-Biomembranes* **2010**, *1798*, 1427–1435.

[178] Cox, P. A.; Waldow, D. A.; Dupper, T. J.; Jesse, S.; Ginger, D. S. *ACS Nano* **2013**, *7*, 10405–10413.

[179] Nečas, D.; Klapetek, P. *Cent. Eur. J. Phys.* **2012**, *10*, 181–188.

[180] O'Haver, T. terpconnect.umd.edu/˜toh/spectrum/InteractivePeakFitter.htm. ipf.m Peak Fitter.

[181] Google Scholar. https://scholar.google.com/.

[182] In-Nano, *ACS Nano* **2012**, *6*, 990–992.